RAA 2014 Vol. **14** No. **9**, 1061–1120 doi: 10.1088/1674–4527/14/9/002
http://www.raa-journal.org *http://www.iop.org/journals/raa*

Research in Astronomy and Astrophysics

INVITED REVIEWS

Probing the dark side of the Universe with weak gravitational lensing effects *

Li-Ping Fu[1] and Zu-Hui Fan[2]

[1] Shanghai Key Lab for Astrophysics, Shanghai Normal University, Shanghai 200234, China; *fuliping@shnu.edu.cn*
[2] Department of Astronomy, School of Physics, Peking University, Beijing 100871, China; *fanzuhui@pku.edu.cn*

Received 2014 March 20; accepted 2014 May 7

Abstract Arising from gravitational deflections of light rays by large-scale structures in the Universe, weak-lensing effects have been recognized as one of the most important probes in cosmological studies. In this paper, we review the main progress in weak-lensing analyses, and discuss the challenges in future investigations aiming to understand the dark side of the Universe with unprecedented precisions.

Key words: cosmology: dark matter and dark energy — large-scale structure of universe — gravitational lensing

1 INTRODUCTION

The tremendous advance in astronomical observations has led to the emergence of a concordance cosmological model, in which dark matter and dark energy account for about 23% and 72%, respectively, of the total energy budget of the Universe (e.g. Spergel et al. 2003; Komatsu et al. 2011; Planck Collaboration et al. 2013a). Understanding the dark side of the Universe has thus been one of the most fundamental challenges in scientific research. The properties of dark matter and dark energy affect the global expansion behavior of the Universe and the formation and evolution of large-scale structures (LSSs). Therefore constraints on the two dark components can be derived by accurately measuring both (e.g., Weinberg et al. 2013b; Bauer et al. 2013). Gravitational in origin, weak-lensing effects result from the light deflection by LSSs in the Universe. In addition, similar to ordinary optical lens systems, their observational effects also sensitively depend on the geometrical distances between observer, lens and source (e.g., Bartelmann & Schneider 2001). Thus weak-lensing effects are closely related to both LSSs and the expansion history of the Universe, and have been recognized as one of the highly promising probes in cosmological studies (e.g., LSST Science Collaboration et al. 2009; Laureijs et al. 2011; Spergel et al. 2013; Weinberg et al. 2013a). Particularly, they are gravity induced and can reveal the underlying large-scale dark matter distribution much more directly than other analyses, such as galaxy clustering (e.g., Anderson et al. 2012), X-ray (e.g., Rosati et al. 2002; Peterson & Fabian 2006) or Sunyaev-Zeldovich effects (Sunyaev & Zeldovich 1970; Birkinshaw 1999), which are strongly affected by complicated gas physics.

* Supported by the National Natural Science Foundation of China.

On the other hand, however, because they are very weak, it is extremely challenging to extract weak-lensing signals from observations (e.g., Miller et al. 2013). Having been speculated to exist even before the establishment of the general theory of relativity, not until the 1990s were the expected coherent shape distortions of background galaxies caused by weak lensing first seen around massive foreground clusters of galaxies (Tyson et al. 1990). The cosmic shear signals from LSSs were detected around the year 2000 (Bacon et al. 2000; Kaiser et al. 2000; Van Waerbeke et al. 2000; Wittman et al. 2000). Since then, weak-lensing studies have rapidly developed, and become an important area of research in cosmology (e.g., Fu et al. 2008; Heymans et al. 2012; Erben et al. 2013; Hoekstra et al. 2013).

In this paper, we present an overview of the current status of weak-lensing studies and discuss their future prospects in the era of precision cosmology. The rest of the paper is organized as follows. We outline the theoretical basics for weak-lensing effects in Section 2. In Section 3, we describe the observational procedures for measuring weak-lensing shear signals. Cosmological applications of weak-lensing effects are presented in Section 4, including studies on the mass distribution of individual clusters of galaxies, cosmic shear correlation analyses, weak-lensing peak statistics and galaxy-galaxy lensing analyses. Discussions are contained in Section 5. We use the the speed of light $c = 1$ throughout the paper.

2 BASICS OF THE WEAK GRAVITATIONAL LENSING EFFECT

In the theoretical framework of general relativity, the inhomogeneous matter distribution in the Universe induces perturbations in the spacetime metric, and therefore affects the moving path of particles therein including those of photons (e.g., Schneider et al. 1992). Such light deflections by intervening LSSs can change the appearance of background sources. When light rays pass through central regions of foreground galaxies or cluster of galaxies, strong-lensing effects can occur, generating multiple/highly distorted images of a background source. For most of the Universe, however, the lensing effect is weak, and only leads to a tiny shape distortion and magnitude change for a background source. This is referred to as the weak-lensing effect, which can only be studied statistically by observing a large number of background sources (e.g., Bartelmann & Schneider 2001). Here we summarize the basic theory of the gravitational lensing effect, particularly for the weak-lensing effect. Before that, we first introduce the standard model for the evolution of the background and the perturbed Universe on the basis of the theory of general relativity.

2.1 Background Universe

For the background Universe without perturbations, its spacetime can be described by the following Friedmann-Lemaitre-Robertson-Walker (FLRW) metric

$$ds^2 = dt^2 - a^2(t)\left[d\chi^2 + f_{\rm K}^2(\chi)d\boldsymbol{\theta}'^2\right], \tag{1}$$

where $a(t)$ is the cosmic scale factor that is related to the redshift by $a_0/a = 1+z$, χ is the comoving radial distance, and $d\boldsymbol{\theta}'^2$ represents the solid angle element. The function $f_{\rm K}$ is given by

$$f_{\rm K}(\chi) = \begin{cases} K^{-1/2}\sin(K^{1/2}\chi) & \text{if } K > 0\,, \\ \chi & \text{if } K = 0\,, \\ (-K)^{-1/2}\sinh[(-K)^{1/2}\chi] & \text{if } K < 0\,, \end{cases} \tag{2}$$

where $K = \text{constant}$ is related to the spatial curvature of the Universe.

In the theory of general relativity, a and K are determined by the matter composition of the Universe through the following Friedmann equations

$$\left(\frac{\dot{a}}{a}\right)^2 + \frac{K}{a^2} = \frac{8\pi G}{3}\sum_i \rho_i\,, \tag{3}$$

$$\frac{\ddot{a}}{a} = -\frac{4\pi G}{3}\sum_i (\rho_i + 3p_i)\,, \tag{4}$$

where the dot symbol is for the derivative with respect to t, and ρ_i and p_i denote the energy density and the pressure of the ith component, respectively. Without considering the coupling between different components, we have from Equations (3) and (4)

$$d(a^3\rho_i) = -p_i da^3. \tag{5}$$

In the fluid approach, the physical properties of different components in the Universe are often described by the corresponding equation of state in the form $p = w\rho$, where w is the equation-of-state parameter. For the matter component including the cold dark matter and the baryonic matter after photon-baryon decoupling, we take $w = 0$. For the radiation component, $w = 1/3$. For the dark energy component that drives the accelerating expansion of the Universe, $w < -1/3$ is required where w can change with time (redshift). For the cosmological constant, the equivalent $w = -1$. From Equation (5), we have in general

$$\rho_i = \rho_0 \exp\left\{-3\int_{a_0}^{a} da \frac{1 + w_i(a)}{a}\right\}, \tag{6}$$

where the subscript '0' denotes the present value at redshift $z = 0$. Therefore $\rho_\mathrm{m} \propto a^{-3}$ for the matter component, $\rho_\gamma \propto a^{-4}$ for the radiation component, and $\rho_\Lambda = \mathrm{constant}$ for the cosmological constant term.

With the Hubble parameter defined as $H(a) = \dot{a}/a$, the critical density of the Universe $\rho_\mathrm{crit}(a)= 3H(a)^2/(8\pi G)$, and the dimensionless energy density parameter $\Omega_i(a) = \rho_i(a)/\rho_\mathrm{crit}(a)$, Equation (3) can be written as

$$H(a)^2 = H_0^2\left[\sum_i \Omega_i\left(\frac{\rho_i(a)}{\rho_{i0}}\right) + \Omega_\mathrm{K}\left(\frac{a_0^2}{a^2}\right)\right], \tag{7}$$

where $\Omega_\mathrm{K} = 1 - \Omega_\mathrm{tot} = 1 - \sum_i \Omega_i$. To be consistent with the convention in literature, here we use Ω_i without the subscript '0' for the present dimensionless density of component i, and $\Omega_i(a)$ for the corresponding quantity at time a. It is seen that a different energy composition leads to different evolutionary behavior of $a(t)$. Therefore by accurately measuring the expansion history of the Universe, we can possibly tell what our Universe is made of, and further probe the nature of dark matter and dark energy.

Figure 1 shows $a(t)/a_0$ for different cosmological models with H_0 fixed, where a_0 is the scale factor at present. The horizontal x-axis is for t/t_0 with t_0 being the age of the flat ΛCDM model with $\Omega_\mathrm{m} = 0.3$ and $\Omega_\Lambda = 0.7$. We choose $t = 0$ at present. Thus the corresponding age of a model can be read out by $-x_i \times t_0$ where x_i is the x-value at $a = 0$. For dynamical dark energy models, here we consider two cases, one with a constant equation-of-state parameter $w = -0.7$, and the other with $w(a) = w_0 + w_a(1 - a)$ and $(w_0, w_a) = (-0.9, -1.1)$, respectively. We can see that the past expansion history of the model with $(w_0, w_a) = (-0.9, -1.1)$ (black) is very similar to that of the ΛCDM model (blue). Indeed, both of the models can fit the current cosmological observations well (Planck Collaboration et al. 2013a). On the other hand, the future evolutionary paths of the two models are very different. For $(w_0, w_a) = (-0.9, -1.1)$, because $(1 - a) < 0$ for the future, $w(a)$

will eventually become positive and thus lead to a deceleration of the Universe. It should be noted, however, that the behaviors at $t > 0$ (future) are shown purely for illustrative purposes, and the form of $w(a)$ used here may not be physically valid to describe the equation of state of dark energy in future times. Nonetheless, we see that the properties of dark energy strongly affect the evolution of the Universe.

Now we turn to the definition of distances. In a cosmological context, different measurements give rise to different distances. By comparing the energy of light rays we receive with the energy emitted from a source, we get the luminosity distance $D_{\rm L}$ specifically defined as

$$D_{\rm L}^2 = \frac{L}{4\pi F}\,, \tag{8}$$

where L is the luminosity emitted by the source and F is the flux received by the observer. The measurements of $D_{\rm L}$ involve standardizable candles, such as Cepheid variable stars from the period-luminosity relation, spiral galaxies using the Tully-Fisher relation and Type Ia supernovae (SNeIa). On the other hand, the measurement of angular extension $\delta_{\rm A}$ of a physical scale $X_{\rm A}$ leads to the angular diameter distance $D_{\rm A}$ defined as

$$D_{\rm A} = \frac{X_{\rm A}}{\delta_{\rm A}}\,. \tag{9}$$

In a time-evolving Universe, these two distances are not the same but related to each other by the distance duality relation $D_{\rm L} = (1+z)^2 D_{\rm A}$. Both $D_{\rm L}$ and $D_{\rm A}$ are related to the comoving radial distance χ that light rays propagate. Considering a source at redshift z_1 and an observer at redshift z_0, the light rays travel following the null geodesics with $ds^2 = 0$, i.e., $dt = -a(t)d\chi$ with the minus sign chosen corresponding to $\chi = 0$ at the observer's location. We then have

$$d\chi = -\frac{dt}{a} = -\frac{da}{a\dot{a}} = -\frac{da}{a^2 H(a)} = \frac{1}{a_0 H_0}\frac{dz}{E(z)}\,, \tag{10}$$

where we have used the relation $1 + z = a_0/a$ and $E(z) = H(z)/H_0$. Thus

$$\chi(z_0, z_1) = \frac{1}{a_0 H_0}\int_{z_0}^{z_1}\frac{dz}{E(z)}\,. \tag{11}$$

For a cosmological model consisting of matter, radiation and dark energy, from Equation (7), we have

$$E(z) = \sqrt{\Omega_{\rm m}(1+z)^3 + \Omega_{\gamma 0}(1+z)^4 + \Omega_{\rm DE}\exp\big[3\int_0^z dz'\frac{1+w_{\rm DE}(z')}{1+z'}\big] + \Omega_{\rm K}(1+z)^2}\,. \tag{12}$$

The angular diameter distance $D_{\rm A}$ is then given by

$$D_{\rm A} = a(z_1) f_{\rm K}[\chi(z_1, z_0)] = \frac{a_0 f_{\rm K}[\chi(z_1, z_0)]}{1+z_1}\,, \tag{13}$$

where $f_{\rm K}$ is called the comoving angular diameter distance and is given in Equation (2).

In Figure 2, we show $D_{\rm A}$ for the same set of cosmological models as that shown in Figure 1. We will see later that the lensing effect depends on the angular diameter distances from the observer to the lens, to the source and between the lens and the source, and therefore sensitively depends on the expansion history of the Universe.

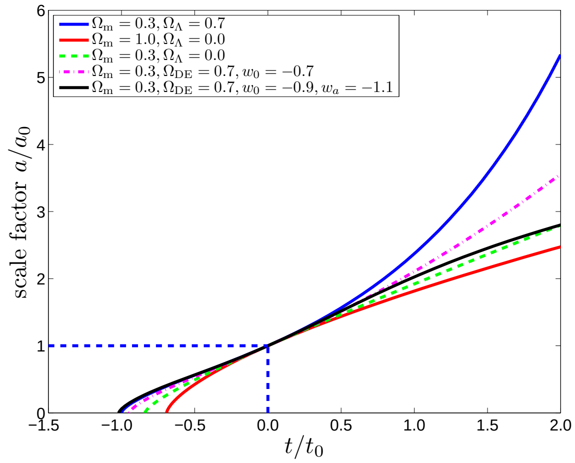

Fig. 1 The scale factor a/a_0 for different cosmological models. The horizontal x-axis is t/t_0 where t_0 is the present age of the flat ΛCDM model with $\Omega_m = 0.3$ and $\Omega_\Lambda = 0.7$. We choose $t = 0$ for the present time.

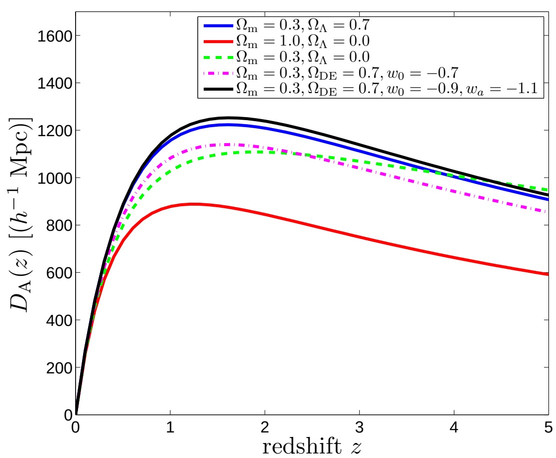

Fig. 2 The angular diameter distance for different cosmological models in units of h^{-1} Mpc.

2.2 Perturbed Universe

While it is homogeneous and isotropic on very large scales, the Universe is full of structures on scales less than a few hundred Mpc. These LSSs arise from primordial perturbations generated in the inflationary epoch, which have been amplified with the evolution of the Universe (e.g., Dodelson 2003). In the concordance cosmological model, the dark matter component plays the dominant role to gravitationally lay the skeleton of LSSs. The baryonic matter component then falls into the potential wells and goes through complex processes, such as heating and cooling, to eventually form luminous objects observable to us (e.g., Mo et al. 2010). The inhomogeneous matter distribution related to LSSs perturbs the light propagation and leads to the gravitational lensing effects (e.g., Schneider et al. 1992).

To describe the perturbed Universe, we adopt the conformal Newtonian gauge in which the spacetime metric can be written as (e.g., Dodelson 2003)

$$ds^2 = \Big[1 + 2\Phi(\boldsymbol{x})\Big]dt^2 - a^2\Big[1 + 2\Psi(\boldsymbol{x})\Big]\Big[d\chi^2 + f_{\mathrm{K}}^2(\chi)d\boldsymbol{\theta}'^2\Big]\,, \tag{14}$$

where Φ and Ψ reflect the perturbations on the metric from the inhomogeneous matter distribution. The quantity Φ has a similar meaning as a gravitational potential in Newtonian theory, and Ψ represents perturbations to the spatial curvature of the Universe. In weak-lensing studies, we are mainly interested in the late evolutionary stage of the Universe where the matter component significantly dominates over the radiation component. Thus in the theory of general relativity neglecting the anisotropic stress, we have $\Psi = -\Phi$. For subhorizon matter perturbations, the potential satisfies

$$\nabla^2\Phi(\boldsymbol{x}) = 4\pi G a^2 \bar{\rho}_{\mathrm{m}}\delta(\boldsymbol{x})\,, \tag{15}$$

where $\delta(\boldsymbol{x}) = [\rho_{\mathrm{m}}(\boldsymbol{x}) - \bar{\rho}_{\mathrm{m}}]/\bar{\rho}_{\mathrm{m}}$ with $\bar{\rho}_{\mathrm{m}}$ being the background matter density of the Universe. It is noted that Equation (14) and Equation (15) hold even in the nonlinear regime of matter perturbations with $\delta \gg 1$ as long as $|\Phi| \ll 1$ and $|\Psi| \ll 1$ (e.g., Ishibashi & Wald 2006).

For the perturbation field $\delta(\boldsymbol{x})$, it can be expressed in terms of its Fourier modes $\delta(\boldsymbol{k})$ with

$$\delta(\boldsymbol{x}) = \int \frac{d^3\boldsymbol{k}}{(2\pi)^3}\exp(i\boldsymbol{k}\cdot\boldsymbol{x})\delta(\boldsymbol{k})\,. \tag{16}$$

The power spectrum is defined as $P(\boldsymbol{k}) = |\delta(\boldsymbol{k})|^2$, representing the spatial characteristics of the perturbation field at different scales. For a statistically homogeneous and isotropic perturbation field, $P(\boldsymbol{k}) = P(|\boldsymbol{k}|)$, it is related to the two-point correlation function $\xi(\boldsymbol{r}_1, \boldsymbol{r}_2) = \xi(|\boldsymbol{r}_1 - \boldsymbol{r}_2|)$ of the field by

$$\xi(|\boldsymbol{r}_1 - \boldsymbol{r}_2|) = \int \frac{d^3\boldsymbol{k}}{(2\pi)^3}\exp[i\boldsymbol{k}\cdot(\boldsymbol{r}_1 - \boldsymbol{r}_2)]P(|\boldsymbol{k}|)\,. \tag{17}$$

It is known that the statistical properties of a Gaussian random field can be fully described by its two-point correlation function (power spectrum) (e.g., Bardeen et al. 1986). For the standard paradigm of structure formation in the Universe, the matter inhomogeneity is seeded in the inflationary epoch and the primordial perturbation field can be well described by a Gaussian random field. The evolution of the perturbation field δ depends on cosmological models. In the early stage of the Universe, δ is small and its evolution follows the linearized dynamical equations and the Gaussianity of δ is preserved. Therefore the power spectrum of linear density perturbations plays an important role in cosmological studies. It is generally written as

$$P(k, a) = P_i(k, a_i)T^2(k, a)G^2(a)/G^2(a_i)\,, \tag{18}$$

where $P_i(k, a_i)$ is the primordial power spectrum at very early time a_i, and $T(k, a)$ is the transfer function that describes the scale-dependent evolution of perturbations since the epoch of horizon crossing to the stage when the perturbations of different scales start to evolve similarly afterwards. The overall increase of the perturbations is then represented by the linear growth factor $G(a)$. For P_i, it can be written as a power law with $P_i(k) \propto k^{n_{\mathrm{s}}}$. For $T(k, a)$, it depends on the matter content of the Universe and can be accurately calculated given a cosmological model (e.g., Eisenstein & Hu 1999; Lewis et al. 2000). For the linear growth factor in the late stage, we have, from the linear dynamical equations (e.g., Dodelson 2003),

$$\frac{d^2G}{da^2} + \left(\frac{d\ln H}{da} + \frac{3}{a}\right)\frac{dG}{da} - \frac{3\Omega_{\mathrm{m}}H_0^2}{2a^5H^2}G = 0\,. \tag{19}$$

It is seen that the behavior of $G(a)$ depends on the expansion history of the Universe, which is in turn governed by the matter composition of the Universe.

Figure 3 shows $G(a)$ for different cosmological models by solving Equation (19) under the initial conditions with $G(a_i) = a_i$ and $dG/da|_{a_i} = 1$ with $a_i = 0.01$. Its model dependence is clearly seen. We should note that the values of G shown in Figure 3 are arbitrarily normalized to a_i for different models.

For the amplitude of the power spectrum, it is often represented by the quantity σ_8, the rms of the extrapolated linear perturbations smoothed over the top-hat smoothing scale of $8\ h^{-1}$ Mpc, which is given by

$$\sigma_8^2 = \int \frac{d^3\boldsymbol{k}}{(2\pi)^3} P(|\boldsymbol{k}|, a_0) W^2(kR_{\rm TH}), \tag{20}$$

where $W(kR_{\rm TH})$ is the Fourier transform of the top-hat smoothing function and the smoothing scale $R_{\rm TH} = 8\ h^{-1}$ Mpc. It is seen that to fully specify the linear power spectrum of perturbations, we need to know $n_{\rm s}$ and σ_8 in addition to $\Omega_{\rm m}$, $\Omega_{\rm DE}$ and $w_{\rm DE}$. Furthermore, different properties of different types of matters, baryonic or cold/warm/hot dark matter, affect the transfer function differently. Therefore we also need the information about, e.g., the baryonic content $\Omega_{\rm B}$, neutrino mass and so on.

Put another way, cosmological observations on LSSs and the expansion history of the Universe can thus set constraints on these important cosmological parameters and further reveal the nature of dark matter and dark energy as well as the physics driving inflation in the early Universe. Current observations show that for a flat ΛCDM model with $\Omega_{\rm m}+\Omega_\Lambda = 1$ and $w_{\rm DE} = -1$, we have $\Omega_{\rm m}h^2 = 0.1426 \pm 0.0025$, $\Omega_{\rm B}h^2 = 0.02205 \pm 0.00028$, $n_{\rm s} = 0.9603 \pm 0.0073$ and $\sigma_8 = 0.829 \pm 0.012$ (Planck Collaboration et al. 2013a). Without the prior on the flatness, the curvature of the Universe is constrained to be $\Omega_{\rm K} = 0.0005^{+0.0065}_{-0.0066}$, i.e., our Universe is nearly flat to a very high precision (Planck Collaboration et al. 2013a). Meaningful constraints on the properties of neutrinos, including their total mass and the effective number of species, have also been derived, demonstrating the great power of cosmological observations that are highly complementary to particle physics experiments (e.g., Li et al. 2009a; Komatsu et al. 2011; Planck Collaboration et al. 2013a). For the nature of dark energy, the cosmological constant can fit well with current observations. However, the allowed range for dynamical dark energy models is still large (e.g., Zhao & Zhang 2010; Weinberg et al. 2013b). Future cosmological observations will target constraints with much improved precision in order to better understand our Universe (e.g., LSST Science Collaboration et al. 2009; Laureijs et al. 2011; Spergel et al. 2013). For that, weak-lensing effects are expected to play crucial roles as one of the most promising probes (e.g., Fu et al. 2008; Li et al. 2009a; Kilbinger et al. 2013; Simpson et al. 2013; Fu et al. 2014) .

In the above, we discuss linear density perturbations. For structure formation to occur, however, nonlinear gravitational interactions are strong on scales of a few Mpc or less (e.g., Mo et al. 2010). For weak-lensing effects on arcmin scales, the signals are dominantly contributed by nonlinear structures. Therefore we have to go beyond linear perturbations (e.g., Kilbinger et al. 2013). Fortunately, fast developments in numerical simulations allow us to trace the nonlinear gravitational evolution of structure formation rather accurately (e.g., Springel et al. 2005; Sato et al. 2009; Hilbert et al. 2009; Harnois-Déraps et al. 2012). With these nonlinear interactions, couplings occur between different Fourier modes. The statistics of density perturbations show significant non-Gaussianity, and the power spectrum/two-point correlation function alone cannot reveal all their properties. Nonetheless, the power spectrum is still a very important quantity directly related to the lowest order correlation analyses. Extensive studies have been done to understand the nonlinear evolution of density perturbations. Different methods calibrated with numerical simulations have been proposed to calculate the nonlinear power spectrum (e.g., Peacock & Dodds 1996; Smith et al. 2003; Lewis et al. 2000).

Figure 4 presents the extrapolated linear power spectrum and the nonlinear power spectrum of density perturbations at $z = 0$ calculated by CLASS (Blas et al. 2011) for different cosmological

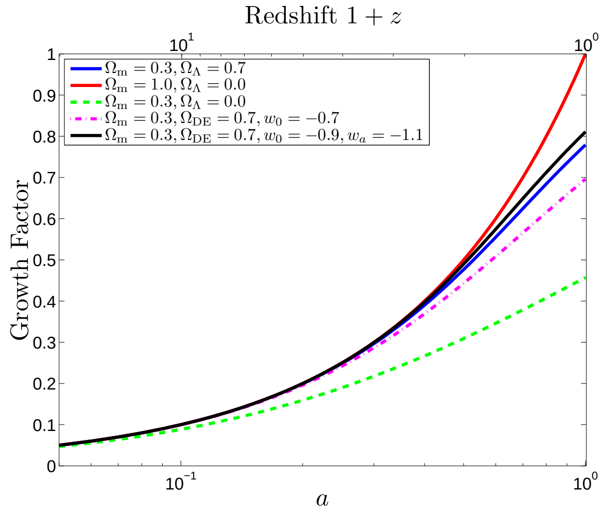

Fig. 3 The linear growth factor for different cosmological models.

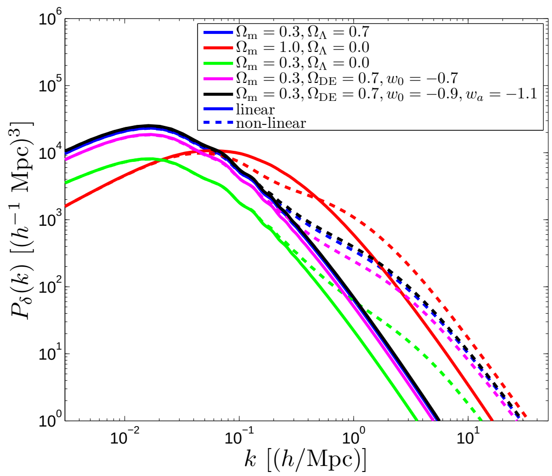

Fig. 4 The linear (*solid lines*) and nonlinear (*dashed lines*) power spectrum for different cosmological models calculated from the CLASS package (Blas et al. 2011) (see also *http://class-code.net*). For all the models, the power amplitude of the primordial curvature perturbations at $k_0 = 0.002\ \mathrm{Mpc}^{-1}$ is set to be $A_s = 2.1 \times 10^{-9}$ and the power index is $n_s = 0.96$.

models. It is seen that the nonlinearity considerably enhances the small-scale power, leading to significant effects on weak-lensing signals as we will see later.

2.3 Weak Lensing Effects

We now turn to weak-lensing effects. We start from a Schwarzschild lens (i.e., a point-mass lens) of mass M (e.g., Schneider et al. 1992; Bartelmann & Schneider 2001). A light ray from a distant source reaches the observer along the direction $\boldsymbol{\beta}$ with respect to a chosen optical axis in the case

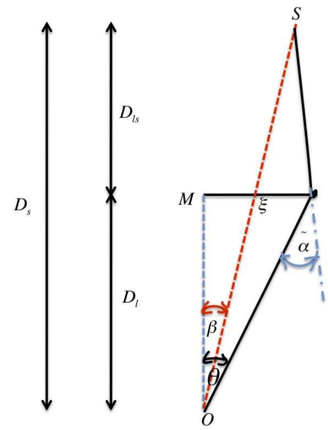

Fig. 5 A schematic configuration of a Schwarzschild lens system. Adapted from Schneider et al. (1992).

of no gravitational lens in the path. With a lens, the ray is deflected when it passes by the lens, and the deflection angle is known to be $\tilde{\boldsymbol{\alpha}} = (4GM)\boldsymbol{\xi}/|\boldsymbol{\xi}|^2$ (note $c = 1$ is used), twice that obtained by the Newtonian theory of gravity. Here $|\boldsymbol{\xi}|$ is the impact parameter satisfying $|\boldsymbol{\xi}| \gg R_{\rm s} = 2GM$ with $R_{\rm s}$ being the Schwarzschild radius. The observer then sees the light ray from the direction $\boldsymbol{\theta}$. The configuration of the system is schematically shown in Figure 5, where $D_{\rm s}, D_{\rm l}$ and $D_{\rm ls}$ denote the angular diameter distances from the observer O to the source S, to the lens, and between the lens and the source, respectively. The mapping between $\boldsymbol{\theta}$ and $\boldsymbol{\beta}$ satisfies the following relation

$$D_{\rm s}\boldsymbol{\beta} = \frac{D_{\rm s}}{D_{\rm l}}\boldsymbol{\xi} - D_{\rm ls}\tilde{\boldsymbol{\alpha}}(\boldsymbol{\xi})\,, \tag{21}$$

and with $\boldsymbol{\xi} = D_{\rm l}\boldsymbol{\theta}$, we have

$$\boldsymbol{\beta} = \boldsymbol{\theta} - \frac{D_{\rm ls}}{D_{\rm s}}\tilde{\boldsymbol{\alpha}}(D_{\rm l}\boldsymbol{\theta}) = \boldsymbol{\theta} - \boldsymbol{\alpha}(\boldsymbol{\theta})\,, \tag{22}$$

where the scaled deflection angle $\boldsymbol{\alpha}$ is defined as $\boldsymbol{\alpha} = (D_{\rm ls}/D_{\rm s})\tilde{\boldsymbol{\alpha}}$. The above equation is often referred to as the lens equation.

For a lens with a mass distribution of $\rho(\boldsymbol{r})$, if the light deflection is much smaller than the characteristic scale on which the mass density changes appreciably, the thin-lens description is an excellent approximation. In such a case, the total deflection angle can be written as the linear summation of the deflections from different mass elements along a straight line within the lens, and is given by (e.g., Bartelmann & Schneider 2001)

$$\tilde{\boldsymbol{\alpha}}(\boldsymbol{\xi}) = 4G\int d^2\boldsymbol{\xi}'\Sigma(\boldsymbol{\xi}')\frac{\boldsymbol{\xi}-\boldsymbol{\xi}'}{|\boldsymbol{\xi}-\boldsymbol{\xi}'|^2}\,, \tag{23}$$

where $\Sigma(\boldsymbol{\xi})$ is the surface mass density of the lens projected along the line of sight and

$$\Sigma(\boldsymbol{\xi}) = \int dx_3\rho(\boldsymbol{\xi}, x_3)\,. \tag{24}$$

The corresponding scaled deflection angle $\boldsymbol{\alpha}$ is

$$\boldsymbol{\alpha}(\boldsymbol{\theta}) = \frac{1}{\pi}\int d^2\boldsymbol{\theta}'\kappa(\boldsymbol{\theta}')\frac{\boldsymbol{\theta}-\boldsymbol{\theta}'}{|\boldsymbol{\theta}-\boldsymbol{\theta}'|^2}\,, \tag{25}$$

where $\kappa(\boldsymbol{\theta}) = \Sigma(D_{\rm l}\boldsymbol{\theta})/\Sigma_{\rm cr}$ is the dimensionless surface mass density of the lens called the lensing convergence, and

$$\Sigma_{\rm cr} = \frac{1}{4\pi G}\frac{D_{\rm s}}{D_{\rm l}D_{\rm ls}}\,. \tag{26}$$

By inspecting Equation (25), we can see that $\boldsymbol{\alpha}$ can be written as the derivative of a deflection potential with $\boldsymbol{\alpha} = \nabla\psi$, and the potential is given by

$$\psi(\boldsymbol{\theta}) = \frac{1}{\pi}\int d^2\boldsymbol{\theta}'\kappa(\boldsymbol{\theta}')\ln|\boldsymbol{\theta}-\boldsymbol{\theta}'|\,. \tag{27}$$

The convergence κ then satisfies $\nabla^2\psi(\boldsymbol{\theta}) = 2\kappa(\boldsymbol{\theta})$.

With the lens equation and deflection angle, we can then analyze the lensing-induced image change for a background source (e.g., Bartelmann & Schneider 2001). Let $I^S(\boldsymbol{\beta})$ and $I^O(\boldsymbol{\theta})$ be the original and the observed surface brightness of the source, respectively. Because the gravitational light deflection does not change the surface brightness but only the propagation direction of a light ray, we have $I^O(\boldsymbol{\theta}) = I^S[\boldsymbol{\beta}(\boldsymbol{\theta})]$. For a source with a size much smaller than the characteristic scale over which the lens properties significantly change, the lensing mapping can be approximately written as $\boldsymbol{\beta}(\boldsymbol{\theta}) = \boldsymbol{\beta}_0 + A(\boldsymbol{\theta}_0)(\boldsymbol{\theta}-\boldsymbol{\theta}_0)$ with the Jacobian matrix

$$A = \frac{\partial\boldsymbol{\beta}}{\partial\boldsymbol{\theta}} = \left(\delta_{ij} - \frac{\partial^2\psi(\boldsymbol{\theta})}{\partial\theta_i\partial\theta_j}\right) = \begin{pmatrix} 1-\kappa-\gamma_1 & -\gamma_2 \\ -\gamma_2 & 1-\kappa+\gamma_1 \end{pmatrix}, \tag{28}$$

where γ_1 and γ_2 are the two shear components with

$$\gamma_1 = \frac{1}{2}\left(\frac{\partial^2\psi}{\partial^2\theta_1} - \frac{\partial^2\psi}{\partial^2\theta_2}\right), \qquad \gamma_2 = \frac{\partial^2\psi}{\partial\theta_1\partial\theta_2}\,. \tag{29}$$

We then see that lensing effects can change the appearance of a source. A circular isophote of a source is distorted into an ellipse with the axial ratio determined by the two eigenvalues of the Jacobian matrix A of Equation (28). Specifically, the axial ratio is given by

$$r = \frac{1-\kappa-|\gamma|}{1-\kappa+|\gamma|} = \frac{1-|g|}{1+|g|}\,, \tag{30}$$

where $|\gamma| = \sqrt{\gamma_1^2+\gamma_2^2}$, and $g_i = \gamma_i/(1-\kappa)$ is called the reduced shear. If the shear $\gamma = 0$, no shape distortions occur. On the other hand, it is noted that it is the reduced shear g that is directly related to the lensing induced shape distortions. The lensing effects from a spherically overdense/underdense region tend to shear the background sources tangentially/radially with respect to the center of the region.

Besides the shape distortion, lensing effects also change the cross section of a light bundle resulting in a flux change of the observed image compared to the case of no lensing effects. This is represented by the magnification factor μ given by

$$\mu = \frac{1}{\det A} = \frac{1}{(1-\kappa)^2-|\gamma|^2}\,. \tag{31}$$

The value $|\mu| > 1$ (< 1) indicates a brightening (dimming) effect from lensing, and μ can be either positive (positive parity) or negative (negative parity) (e.g., Schneider et al. 1992).

In central parts of galaxies or clusters of galaxies, lensing effects are strong and apparent. Multiple images or heavily distorted giant arc-like images of background sources can occur (e.g., Walsh et al. 1979; Soucail et al. 1987; Lynds & Petrosian 1989; More et al. 2012; Inada et al. 2012; Kneib & Natarajan 2011, and the references therein). By accurately measuring the position, luminosity and shape of the images, one can effectively derive constraints on the mass distribution for the central part of the lens (e.g., Courteau et al. 2014; Hoekstra et al. 2013). For most of the Universe, however, the lensing effects are weak with $\kappa \ll 1$ and $|\gamma| \ll 1$. Thus the weak-lensing effect, the main topic of this paper, is directly associated with LSSs in the Universe and is potentially very powerful in cosmological studies.

The drawback of weak-lensing studies is that it is impossible to detect the weak-lensing effect from a single background source given that the intrinsic ellipticities of galaxies are much larger than the lensing-induced shape distortions and their intrinsic luminosities are not known. Statistical analyses that come from observing a large number of background sources are thus necessary (e.g., Heymans et al. 2012). For weak-lensing studies with shape measurements of background galaxies, the noise from random intrinsic ellipticities can be suppressed by averaging over a number of galaxies. The residual noise is on the level of $\sigma_{\epsilon_{\rm s}}/\sqrt{n_{\rm g}\theta_0^2}$ where $\sigma_{\epsilon_{\rm s}}$ is the dispersion of the intrinsic ellipticity of background galaxies, $n_{\rm g}$ is their surface number density used in the weak-lensing analyses, and θ_0 is the typical scale we are interested in. The term $n_{\rm g}\theta_0^2$ corresponds to the number of galaxies over which the average is calculate. For $\sigma_{\epsilon_{\rm s}} \sim 0.3$ and $n_{\rm g} \sim 10$ arcmin^{-2}, typical for the current generation of observations, such as CFHTLenS (e.g., Erben et al. 2013), the residual noise is $\sim 0.1/\theta_0$. To obtain a signal with signal-to-noise ratio (S/N) of ~ 3, we need the signal smoothed over the angular scale θ_0 to be on the order of $\gamma \sim 0.3/\theta_0$. Taking $\theta_0 \sim 10'$, for a typical angular scale of a massive cluster at $z \sim 0.2$, the required signal is $\gamma \sim 0.03$. Therefore for massive clusters of galaxies with $M \sim 10^{15}M_\odot$, we are able to individually study their mass distribution through weak-lensing analyses. Increasing $n_{\rm g}$ by acquiring deeper observations can increase the S/N. However even with $n_{\rm g} \sim 50$ arcmin^{-2}, it would be very difficult to study the mass distribution individually for objects with $M < 10^{13}M_\odot$. On the other hand, stacking signals over a large number of foreground lenses can effectively increase the number of background sources used in weak-lensing analyses, and the noise level for the stacked signal is $\sim \sigma_{\epsilon_{\rm s}}/\sqrt{N_{\rm lens}n_{\rm g}\theta_0^2}$ where $N_{\rm lens}$ is the number of lenses in the stacking. This idea is underlying the so-called galaxy-galaxy lensing technique, in which the stacked lensing signals around a large number of lens galaxies are detected to study the average mass distribution for a sample of lens galaxies (e.g., Mandelbaum et al. 2006, 2013). This allows us to probe group-sized and even galaxy-sized dark matter halos statistically, though not individually (e.g., Li et al. 2013; Gillis et al. 2013).

The above discussions focus on the single lens case, in which a single object, such as a cluster of galaxies, dominates the lensing signal along the considered line of sight. In general, however, all the LSSs between a source and an observer contribute to the lensing effect. In order to accurately calculate the lensing signal, in principle, we need to trace the light deflections cumulatively along an actual light path. This can be calculated from the geodesics of a light ray in the perturbed Universe (e.g., Schneider et al. 1992; Bartelmann & Schneider 2001).

The lensing equation is then given by (e.g., Bartelmann & Schneider 2001)

$$\boldsymbol{\beta}(\boldsymbol{\theta},\chi) = \boldsymbol{\theta} - 2\int_0^{\chi} d\chi' \frac{f_{\rm K}(\chi-\chi')}{f_{\rm K}(\chi)f_{\rm K}(\chi')} \nabla_{\boldsymbol{\beta}}\Phi\Big[\boldsymbol{\beta}(\boldsymbol{\theta},\chi'),\chi'\Big]\,, \tag{32}$$

where χ is the comoving radial distance given in Equation (1), $f_{\rm K}$ is the corresponding comoving angular diameter distance given in Equation (2), and Φ is the 3D Newtonian potential given in Equation (14). The multiple lens-plane method has been numerically developed in which the continuous matter distribution between the source and the observer is discretized into multiple thin lens-planes, and a light ray is only deflected when it reaches a lens-plane (e.g., Blandford & Narayan 1986; Jain et al. 2000; Hilbert et al. 2009). The total deflection is obtained by the summation of the deflection at each lens-plane along the deflected light path. In the cosmic shear regime where the lensing deflection is very weak, the Born approximation is an excellent first-order approximation in which the total deflection angle can be calculated along the unperturbed light path. Then the lensing equation can be simplified to (e.g., Bartelmann & Schneider 2001)

$$\boldsymbol{\beta}(\boldsymbol{\theta},\chi)=\boldsymbol{\theta}-2\int_0^{\chi}d\chi'\,\frac{f_{\rm K}(\chi-\chi')}{f_{\rm K}(\chi)f_{\rm K}(\chi')}\nabla_{\boldsymbol{\theta}}\Phi\left[f_{\rm K}(\chi')\boldsymbol{\theta},\chi'\right]. \tag{33}$$

The corresponding Jacobian matrix is given by

$$A_{ij}=\frac{\partial\beta_i}{\partial\theta_j}=\delta_{ij}-2\int_0^{\chi}d\chi'\,\frac{f_{\rm K}(\chi-\chi')}{f_{\rm K}(\chi)f_{\rm K}(\chi')}\frac{\partial^2\Phi[f_{\rm K}(\chi')\boldsymbol{\theta},\chi']}{\partial\theta_i\partial\theta_j}. \tag{34}$$

Then the effective convergence κ is

$$\kappa=\int_0^{\chi}d\chi'\,\frac{f_{\rm K}(\chi-\chi')}{f_{\rm K}(\chi)f_{\rm K}(\chi')}\nabla^2_{\boldsymbol{\theta}}\Phi\left[f_{\rm K}(\chi')\boldsymbol{\theta},\chi'\right], \tag{35}$$

and the shear γ_1 and γ_2 are, respectively,

$$\gamma_1=\int_0^{\chi}d\chi'\,\frac{f_{\rm K}(\chi-\chi')}{f_{\rm K}(\chi)f_{\rm K}(\chi')}\left\{\frac{\partial^2\Phi[f_{\rm K}(\chi')\boldsymbol{\theta},\chi']}{\partial\theta_1^2}-\frac{\partial^2\Phi[f_{\rm K}(\chi')\boldsymbol{\theta},\chi']}{\partial\theta_2^2}\right\}, \tag{36}$$

$$\gamma_2=2\int_0^{\chi}d\chi'\,\frac{f_{\rm K}(\chi-\chi')}{f_{\rm K}(\chi)f_{\rm K}(\chi')}\left\{\frac{\partial^2\Phi[f_{\rm K}(\chi')\boldsymbol{\theta},\chi']}{\partial\theta_1\partial\theta_2}\right\}. \tag{37}$$

From the 3D potential Φ, we have

$$\nabla^2_{\boldsymbol{x}}\Phi=\frac{3H_0^2\Omega_{\rm m}}{2a}\delta(\boldsymbol{x}), \tag{38}$$

where the subscript $\boldsymbol{x}$ indicates the derivatives with respect to the linear coordinates rather than the angular coordinates. Thus

$$\kappa=\frac{3H_0^2\Omega_{\rm m}}{2}\int_0^{\chi}d\chi'\,\frac{f_{\rm K}(\chi-\chi')f_{\rm K}(\chi')}{f_{\rm K}(\chi)}\frac{\delta[f_{\rm K}(\chi')\boldsymbol{\theta},\chi']}{a(\chi')}. \tag{39}$$

It is seen that κ is the weighted projection of the density perturbation δ along the line of sight. For a sample of source galaxies with a redshift distribution $p_{\rm s}(z)dz=p_{\rm s}(\chi)d\chi$, the effective lensing convergence can be obtained by

$$\kappa=\frac{3H_0^2\Omega_{\rm m}}{2}\int_0^{\chi_{\rm H}}d\chi\,p_{\rm s}(\chi)\int_0^{\chi}d\chi'\,\frac{f_{\rm K}(\chi-\chi')f_{\rm K}(\chi')}{f_{\rm K}(\chi)}\frac{\delta[f_{\rm K}(\chi')\boldsymbol{\theta},\chi']}{a(\chi')}, \tag{40}$$

where $\chi_{\rm H}$ indicates the χ value corresponding to $z=\infty$. By changing the order of the integrations, the above equation can be written as

$$\kappa=\frac{3H_0^2\Omega_{\rm m}}{2}\int_0^{\chi_{\rm H}}d\chi'\bar{G}(\chi')f_{\rm K}(\chi')\frac{\delta[f_{\rm K}(\chi')\boldsymbol{\theta},\chi']}{a(\chi')}, \tag{41}$$

where the function $\bar{G}(\chi')$ is

$$\bar{G}(\chi')=\int_{\chi'}^{\chi_{\rm H}}d\chi\,p_{\rm s}(\chi)\frac{f_{\rm K}(\chi-\chi')}{f_{\rm K}(\chi)}. \tag{42}$$

Under the Limber approximation (Limber 1954), the power spectrum of κ is then given by (e.g. Bartelmann & Schneider 2001)

$$P_\kappa(l)=\frac{9H_0^4\Omega_{\rm m}^2}{4}\int_0^{\chi_{\rm H}}d\chi'\,\frac{\bar{G}^2(\chi')}{a^2(\chi')}P_\delta\left[\frac{l}{f_{\rm K}(\chi')};\chi'\right], \tag{43}$$

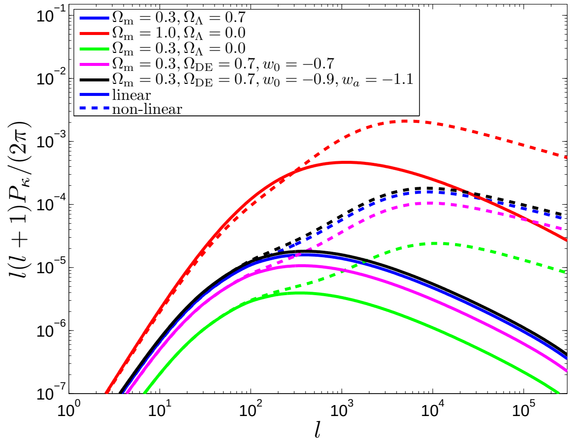

Fig. 6 The lensing convergence power spectrum calculated from the 3D linear (*solid lines*) and nonlinear (*dashed lines*) power spectrum under the Limber approximation for different cosmological models. The model parameters are the same as those in Fig. 4.

where $P_\delta[l/f_{\rm K}(\chi'); \chi']$ is the power spectrum of density perturbation δ at $k = l/f_{\rm K}(\chi')$ and at time corresponding to the radial comoving distance χ'. From Equation (36) and Equation (37), it is easy to see that the power spectrum of $\gamma = \gamma_1 + i\gamma_2$ is the same as P_κ. Therefore P_κ is the crucial quantity in cosmic shear two-point correlation analyses.

In Figure 6, we show $l(l+1)P_\kappa/(2\pi)$ for different cosmological models, where the solid and dashed lines are calculated using the linear and nonlinear P_δ, respectively. The source redshift is set to be $z_{\rm s} = 1$. It is seen clearly that on arcmin scales, the nonlinear effects are dominant and greatly boost weak-lensing signals.

3 OBSERVATIONAL WEAK-LENSING ANALYSES

Weak-lensing shear analyses depend crucially on accurate photometry for a large number of faint galaxies. The development of large mosaics of CCD astronomical cameras opened a new era in imaging surveys. The Sloan Digital Sky Survey[1] (SDSS) is the most successful example that has had a significant impact in astronomical studies. Its great success paved the way for new generations of deep optical and infrared surveys with ambitious scientific goals that were not achievable for surveys with past Schmidt photographic plates. The Canada-France-Hawaii Telescope Legacy Survey[2] (CFHTLS) done with the MegaPrime/MegaCam instrument is the first second-generation wide field survey project. It is also the first set of wide field observations that are optimized for very deep photometry with sub arc-second seeing imaging and a long baseline for monitoring time series. The instruments and the surveys have been designed to out-perform all similar projects and to produce outstanding data sets for studies of SNeIa, weak gravitational lensing and small moving bodies in the Solar System. With further technological improvements, the third-generation of large-scale surveys has been in operation. Some of them are specifically designed or are ideal for weak-lensing

[1] *http://www.sdss.org/*
[2] *http://www.cfht.hawaii.edu/Science/CFHLS/*

observations, such as the VST Kilo-Degree Survey[3] (KIDS) and Dark Energy Survey[4] (DES). The huge amount of data expected from these large surveys require highly efficient and automatic data reduction and analysis softwares.

In this section, we will briefly introduce the basics of data reduction for weak-lensing studies. Three of the most popular softwares to achieve weak-lensing shear measurements from observational images will be presented. We will also describe weak-lensing simulations and discuss relevant systematic uncertainties.

3.1 Data Reduction and Mask Creation

A CCD camera mounted on a telescope is a particle detector, with the associated readout electronics and amplifiers. The sensitivity varies from pixel to pixel because the CCD is not illuminated homogeneously. The raw data observed from a telescope cannot be used directly for scientific studies, and necessary data reduction processes have to be applied. For most of the publicly released data, pre-precessing steps have already been performed. Pre-processing procedures consist of subtracting master biases and darks, and normalizing images with master flats. BIAS exposure is an image exposure in the shortest possible time with the shutter closed. It shows the electronic noise and systematics of the camera, and has to be subtracted from the science exposures. DARK current is caused by the high energy electrons related to the temperature of the camera itself. Therefore one of the ways to reduce the effects of DARK current is to reduce the temperature of the camera. DARK current is very noisy but usually very stable. It can be corrected by subtracting the expected DARK current from pixels, which is estimated by the combination of a series of dark exposures. The other important step in pre-processing is to normalize images with a master FLAT field, an exposure with an area that is homogeneously illuminated. This is for correcting the inhomogeneous effects caused by dust on the optical surfaces or/and the different quantum efficiencies of different pixels on the CCD itself. The common way to get a FLAT field is to take an image of the sky at zenith a few minutes after sunset and to choose an area that is free of gradients. It is necessary to take several flats to reduce the calibration noise.

Further data processing includes astrometric calibration, field-to-field photometric rescaling, image recentering, image resampling and warping, and finally image stacking and a specific masking process. For a general survey, the SCIENCE images with preliminary astrometric position and photometry information are usually provided with the raw images by the data processing center. Here, we briefly introduce the main issues related to data reduction: the image calibration and the stacking process.

For an astrometric calibration of the image, the physical coordinate of each exposure has to first be converted to the World Coordinate System (WCS). Then, the WCS coordinates of detected objects are matched to an external catalog of reference objects. The astrometric calibration for the whole image can thus be done using two-dimensional fitted distortion polynomials obtained by minimizing the differences between the detected objects' WCS coordinates and those of the reference catalog. The internal astrometric accuracy can achieve a level of 10% of a pixel. However, the external accuracy is limited by the accuracy of the reference catalog. A reference catalog usually covers the full sky containing objects with high S/N, such as bright stars with high positional accuracies. Once the astrometric calibration is done, the next step is to perform the photometric calibration. The instrumental fluxes are converted to "magnitude" in order to allow comparisons of photometric measurements between different exposures under various observing conditions or even between different instruments. The zero-point corrections are done similarly to the astrometric calibration, by minimizing the weighted quadratic sum of magnitude differences from overlapping detections of the images. In principle, the accuracy and homogeneity should be improved if all available data are

[3] *http://www.astro-wise.org/projects/KIDS/*
[4] *http://www.darkenergysurvey.org/*

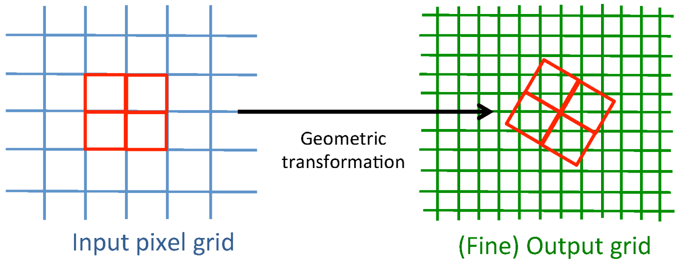

Fig. 7 The explanation of image resampling: mapping of an input image onto a (fine) output image.

taken at the same time to do the astrometric and photometric calibrations. SCAMP[5] is astrometric and photometric calibration software specifically designed for large imaging surveys. It uses the input catalogs and an external reference catalog (e.g., 2MASS, SDSS-R7, USNO) to compute accurate astrometric and photometric calibrations. The astrometric solution is stored in an output WCS image header.

Once the calibration for each exposure is done, the image coadding is the final step of data reduction to get the SCIENCE image. For a telescope, the exposure time of a signal image (called exposure) is limited by the telescope itself, usually a few minutes depending on the observational band. To obtain a deeper image, a few to hundreds of exposures of the same field are needed. They are stacked together to produce one SCIENCE image. In order to have observations in the gap regions between CCDs, different exposures are taken by shifting the center of the camera by a few arcminutes (called dithering). Thus, an important step is to resample images, which is to map pixels of individual exposures to a projected pixel grid. This projection is done by first oversampling each image by a factor of two as shown in Figure 7. Images are then re-centered and resampled using an interpolation kernel, e.g., the Lanczos interpolation kernel, to preserve the noise structure, and to minimize artifacts on the interpolated image.

Before moving to the image coadding process, one can apply further image quality selection criteria, e.g. discarding exposures with obviously bad qualities, such as poor seeing, bad telescope tracking, and telescope defocusing, or with galaxy and star counts strongly out of expectations. It is also important to ensure homogeneity in the pointing level to avoid discarding too many exposures in certain fields. The last step is to coadd all the resampled images that are weighted properly to produce the final SCIENCE image. The coadding can be done by taking weighted mean or median values of pixels from different exposures to ensure the best rejection of satellite trails and cosmic rays. During the coadding process, an additional WEIGHT-MAP image is produced, containing the information about how often individual pixels are observed in the resampled images. This WEIGHT-MAP is often used in object detections providing information about the S/N of different areas of the image. The image resampling and coadding can be done using the public astrometric software SWARP[6].

An additional step in data reduction is to mask the regions that affect the accuracy of object measurement, e.g., saturated stars and their bright halos, cosmic rays, bad pixels, regions with low S/N in image boundaries and CCD gaps, etc. Masks can be generated by public automatic masking softwares, e.g., automask[7]. However, it is essential to further check automatic masks and refine them

5 *http://www.astromatic.net/software/scamp*
6 *http://www.astromatic.net/software/swarp*
7 *http://marvinweb.astro.uni-bonn.de/data_products/THELIWWW/automask.html*

manually, especially for regions with bright halos and low S/N in CCD gaps and the edges of the image.

3.2 Shear Measurement Pipeline

As described in Section 2.4, the weak-lensing effect generates ellipse-like distortions for an observed galaxy image. The ellipticity parameters of a galaxy can be written in the form of the complex ellipticity $\boldsymbol{e} = e_1 + ie_2$. In the weak-lensing regime, the estimate of the lensing shear signal $\boldsymbol{\gamma}$ can ideally be obtained by averaging over the observed image ellipticities of a number of galaxies, $\boldsymbol{\gamma} \approx \langle \boldsymbol{e} \rangle$. In reality however, it is not easy to get an unbiased estimate of shear signals. The observed shapes of objects can be severely contaminated by the point spread function (PSF) caused by the complicated telescope optics, the limited size of the mirror, etc. For ground-based observations, there are additional contaminations resulting from the turbulence of Earth's atmosphere (seeing). Furthermore, the images suffer from pixelization and inefficiency of charge transfer in the CCD itself. The contaminations to the measured shapes of objects consist of isotropic and anisotropic parts. The effects of a seeing disk and the intrinsic size of the PSF circularize the observed images leading to a reduction in the amplitude of the inferred lensing signal. On the other hand, an anisotropic PSF introduces distortions to the shapes of objects, which can mimic lensing signals and therefore introduce systematic uncertainties in lensing shear analyses.

A shear measurement pipeline generally includes the following steps: object detection and separation from SCIENCE images, determination of the observed galaxy shapes, PSF estimation and deconvolution (correction), and calculation of the inferred shear signals.

Galaxies used for weak-lensing analyses are distant background galaxies. The detection and accurate shape determination of these faint objects are not a trivial task. One of the most widely used software packages called SEXTRACTOR[8] has been demonstrated to be able to achieve high accuracies in object detections. It can be done either on individual exposures that have passed all the data reduction processes and calibrations, or on a coadded image. The masks and WEIGHT-MAPS are used to discard saturated stars and bad detections. Galaxies and stars need to be distinguished from all other detections, and galaxy-star separation is often performed on the basis of the size *vs.* magnitude of objects. Stars are point-like objects with more or less uniform observed sizes mainly due to the seeing disk. All detected objects with size larger than the observed size of stars are marked as galaxies, whereas the smaller ones are treated as noise.

The next step is to quantify the shape parameters for stars and galaxies in terms of their sizes, the second and possibly higher moments of their light distributions. Stars are intrinsically point-like objects, therefore their observed sizes and shapes are the results of the effects of seeing and PSF. A sample of moderately bright stars is most suitable for PSF estimations, because the flux measurement for very bright stars can be biased, and faint stars may be contaminated by small and faint galaxies. The variation of the PSF across the field of view can be significant. The central region of a camera has much less, smooth contaminations, whereas the edge regions often have a stronger, significantly varying PSF. Furthermore, for a wide-field camera with arrays of CCD chips, the PSF varies from CCD to CCD. Those variations can be described approximately by an interpolating function, typically a polynomial model. The accuracy of PSF correction is limited by the number of stars used for the model fitting. It is important to choose a proper polynomial function to model the spatial variations of the PSF across the instrument's field of view.

Correction for contamination of the PSF is achieved by subtracting quantities related to the PSF of stars from the ones of galaxies. This is the most difficult part in the shear measurement pipeline. During the past decade, a number of techniques have been developed to correct PSF contamination. Here we briefly review the three most commonly used ones that are applied in shear measurements. The KSB+ is a deconvolution method that aims to remove the PSF effects from observed galaxy

[8] *http://www.astromatic.net/software/sextractor*

images to obtain PSF-free images for lensing shear analyses. On the other hand, both the Shapelets and the *lens*fit adopt a forward-modeling approach that convolves the model images with the PSF and then directly compares the result with the observed galaxy images.

(1) KSB+

The KSB+ method (Kaiser et al. 1995; Luppino & Kaiser 1997; Hoekstra et al. 1998) is the most widely used method in observations. The ellipticity $\boldsymbol{e}$ of an object is defined in terms of the weighted quadrupole moments Q_{ij} $(i, j = 1, 2)$ given by,

$$\begin{pmatrix} e_1 \\ e_2 \end{pmatrix} = \frac{1}{Q_{11}+Q_{22}} \begin{pmatrix} Q_{11}-Q_{22} \\ 2Q_{12} \end{pmatrix}; \qquad Q_{ij} = \frac{\int d^2\theta\, W(\boldsymbol{\theta})\, I(\boldsymbol{\theta})\, \theta_i \theta_j}{\int d^2\theta\, W(\boldsymbol{\theta})\, I(\boldsymbol{\theta})} \,. \tag{44}$$

Here $I(\boldsymbol{\theta})$ is the measured surface brightness at the angular distance $\boldsymbol{\theta}$ from the center of the object (chosen to be at $\boldsymbol{\theta} = 0$), and $W(\boldsymbol{\theta})$ is a weighting function that can be taken as Gaussian with the scale length matched to the size, such as the half-light radius, of galaxies.

KSB+ estimates galaxy ellipticities under the assumption that the PSF distortion can be described by a small but highly anisotropic distortion convolved with a large circularly symmetric seeing disk. The ellipticity of a galaxy $\boldsymbol{e}^{\rm cor}$ corrected for the anisotropic PSF distortion is given by

$$e_\alpha^{\rm cor} = e_\alpha^{\rm obs} - P_{\alpha\beta}^{\rm sm} q_\beta \,, \tag{45}$$

where q is the PSF anisotropy factor, and $P^{\rm sm}$ is called the smear polarizability tensor that can be calculated from $I(\boldsymbol{\theta})$ of the galaxy and the applied weighting function $W(\boldsymbol{\theta})$ (Hoekstra et al. 1998). The q factor can be derived from the stars in the observed field. Since $\boldsymbol{e}^{*\rm cor} = 0$ for stars, we have

$$q_\mu = (P^{\rm sm*})^{-1}_{\mu\alpha}\; e_\alpha^{*\rm obs} \,, \tag{46}$$

where * denotes the quantities measured from stars. From the PSF-corrected $\boldsymbol{e}^{\rm cor}$, we then aim to extract gravitational lensing shear signals. We can write $\boldsymbol{e}^{\rm cor}$ in terms of the pre-seeing shear polarizability tensor P^γ, the gravitational shear $\boldsymbol{\gamma}$ and the intrinsic source ellipticity $\boldsymbol{e}^{\rm s}$,

$$e_\alpha^{\rm cor} = e_\alpha^{\rm s} + P_{\alpha\beta}^{\gamma} \gamma_\beta \,. \tag{47}$$

However, because only the post-seeing images are observable, we cannot directly obtain the pre-seeing quantity P^γ. Instead, we can calculate the post-seeing shear polarizability tensor $P^{\rm sh}$ from the observed $I(\boldsymbol{\theta})$ and the weighting function $W(\boldsymbol{\theta})$. Then using stars in the field as a calibrator, Luppino & Kaiser (1997) give the expression of P^γ as

$$P_{\alpha\beta}^{\gamma} = P_{\alpha\beta}^{\rm sh} - P_{\alpha\mu}^{\rm sm}\, (P^{\rm sm*})^{-1}_{\mu\delta}\, P_{\delta\beta}^{\rm sh*} \,, \tag{48}$$

where $P^{\rm sm*}$ and $P^{\rm sh*}$ are the stellar smear and shear polarizability tensors respectively. Under the assumption that the intrinsic ellipticities of galaxies are randomly oriented and ignoring intrinsic alignments, we have $\langle e^{\rm s} \rangle = 0$. Then the KSB+ shear estimate $\hat{\boldsymbol{\gamma}}$ can be derived by combining Equations (45-48), which is given by

$$\hat{\gamma}_\alpha = (P^\gamma)^{-1}_{\alpha\beta} \left[e_\beta^{\rm obs} - P_{\beta\mu}^{\rm sm} q_\mu \right] \,. \tag{49}$$

(2) Shapelets

The Shapelet technique is a convenient approach for weak lensing analyses, which has been introduced by different literature, e.g. Refregier & Bacon (2003); Massey & Refregier (2005); Kuijken (2006); Bernstein & Jarvis (2002); Nakajima & Bernstein (2007). In this method, a complete and orthonormal set of 2D basis functions is constructed by the product of Gaussians with Hermite or Laguerre polynomials. In principle, the linear combination of these basis functions with proper weights is able to model any compact image, even irregular spiral arms. Such an approach is particularly efficient at modeling and deconvolving the PSF. The shear rotation and magnification effects can be taken as the matrices acting on the shapelet coefficients. Furthermore, the "shapelet" transform is able to filter out high frequency features such as noise in a similar way as Fourier or wavelet synthesis.

We briefly review the shapelet formalism mainly from Kuijken (2006) as an example. The shapelet decomposition fits an individual galaxy image as a sheared intrinsically circular source contaminated by the PSF. The fitting of the observed image is written as the following formula

$$G_{\rm model} = P \cdot (1 + e_1 S_1 + e_2 S_2) \cdot C\,, \tag{50}$$

where P is the PSF matrix, $e_{1,2}$ are the two components of galaxy ellipticities and $S_{1,2}$ are the first-order shear operators. It is noted that $e_{1,2}$ here include both the intrinsic ellipticities of galaxies and the lensing shear signals. In other words, in this approach, an elliptical source with ellipticity $e_{1,2}$ is regarded as a circular source that is sheared twice, first by the intrinsic ellipticity of the source and then by the gravitational lensing shear. For the assumed circular source of an arbitrary radial brightness profile, it can be expressed by the circular shapelets C in the form of $c_0 C^0 + c_4 C^4 + ...$, where c_i are free coefficient parameters. The PSF matrix P of each galaxy is obtained by interpolating the stellar PSF across the field of view to the galaxy position. The best-fitting $G_{\rm model}$ to the observed image yields the estimated ellipticity distortions. The lensing shear signals can then be further obtained by, e.g., averaging over a number of galaxies with proper weights (Kuijken 2006).

(3) *lens*fit

*Lens*fit is a Bayesian model-fitting approach for galaxy shape measurements developed by Miller et al. (2007) and Kitching et al. (2008). Although its fitting process is slower than KSB+ and shapelets, it is fast enough to be used for large weak-lensing surveys. This method allows an optimal joint measurement of multiple, dithered image exposures, taking into account imaging distortions and the alignment of the multiple measurements.

In this method, a Bayesian posterior probability distribution for the ellipticity of a galaxy given its observed image can be generated as (Miller et al. 2007)

$$p_i(\mathbf{e}|\mathbf{y}_i) = \frac{\mathcal{P}\left(\mathbf{e}\right)\mathcal{L}\left(\mathbf{y}_i|\mathbf{e}\right)}{\int \mathcal{P}\left(\mathbf{e}'\right)\mathcal{L}\left(\mathbf{y}_i|\mathbf{e}'\right)d\mathbf{e}'}\,, \tag{51}$$

where $\mathcal{P}\left(\mathbf{e}\right)$ is the ellipticity prior probability distribution and $\mathcal{L}\left(\mathbf{y}_i|\mathbf{e}\right)$ is the likelihood of obtaining the $i^{\rm th}$ set of data values $\mathbf{y}_i$ given ellipticity $\mathbf{e}$ presumably measured without the effects of PSF or noise. Ideally, the true distribution of $\mathbf{e}$ can be obtained from the data by considering the summation over the data,

$$\left\langle \frac{1}{N}\sum_i p_i(\mathbf{e}|\mathbf{y}_i)\right\rangle = \int d\mathbf{y}\frac{\mathcal{P}\left(\mathbf{e}\right)\mathcal{L}\left(\mathbf{y}|\mathbf{e}\right)}{\int \mathcal{P}\left(\mathbf{e}'\right)\mathcal{L}\left(\mathbf{y}|\mathbf{e}'\right)d\mathbf{e}'}\int f(\mathbf{e}'')\epsilon(\mathbf{y}|\mathbf{e}'')d\mathbf{e}''\,, \tag{52}$$

where $\epsilon(\mathbf{y}|\mathbf{e})$ is the probability distribution for $\mathbf{y}$ of the data sample given an $\mathbf{e}$, and $f(\mathbf{e})$ is the sample distribution of $\mathbf{e}$. Equation (52) demonstrates that the integration of the probability distribution for individual galaxies gives rise to the expectation value of the summed posterior probability distribution for the sample. Under the conditions that $\epsilon(\mathbf{y}|\mathbf{e}) = \mathcal{L}\left(\mathbf{y}|\mathbf{e}\right)$ and $\mathcal{P}\left(\mathbf{e}\right) = f\left(\mathbf{e}\right)$, Equation (52) yields the true distribution of $\mathbf{e}$, i.e.,

$$\left\langle \frac{1}{N}\sum_i p_i(\mathbf{e}|\mathbf{y})\right\rangle = \mathcal{P}\left(\mathbf{e}\right) = f(\mathbf{e})\,. \tag{53}$$

In other words, if the chosen prior is a good representation of the underlying distribution of $\mathbf{e}$, the estimated posterior probability should be unbiased. Kitching et al. (2008) propose an iterative method to create the prior from a subset of the data itself. They show that to recover the prior properly, the number of galaxies contained in the subset should be at least on the order of a few hundred depending on the assumed functional form for the prior. It is noted that the lensing shear signals that we are interested in are contained in the ellipticities $\mathbf{e}$. In principle, they should be included in the prior construction. However, the lensing shear signals vary from one place to another. Given the limited number of galaxies in weak-lensing analyses, it is difficult to perform the prior construction locally. Therefore it is suggested that the correct generation of the prior should be zero-shear based and can be obtained from a large number of galaxies (Miller et al. 2007; Kitching et al. 2008). Such a zero-shear prior can introduce a bias in the shear estimate. To correct for the bias, a *shear sensitivity* factor $|\partial\langle\mathbf{e}\rangle_i/\partial\mathbf{g}|$ should be included. Specifically, the estimated shear can be expressed as

$$\hat{\mathbf{g}} = \frac{\sum_i^N \langle\mathbf{e}\rangle_i}{\sum_i^N |\partial\langle\mathbf{e}\rangle_i/\partial\mathbf{g}|} \,. \tag{54}$$

To calculate the likelihood $\mathcal{L}\left(\mathbf{y}_i|\mathbf{e}\right)$ for a galaxy, *lens*fit fits a model surface brightness convolved with a PSF to the galaxy image. Miller et al. (2013) model the varying PSF in individual image exposures on the pixel-based level by taking into account the properties of real surveys. The optimum (with maximum S/N) shape measurement for each galaxy is estimated by fitting the PSF-convolved two-component model with disk and bulge to the observed image, and with Bayesian marginalization over nuisance model parameters of galaxy position, size, brightness and the bulge fraction. The output for each galaxy is a Bayesian "posterior probability surface" of the two ellipticity parameters, marginalized over the above model parameters. A weight for each galaxy is also available considering the variance of the ellipticity likelihood surface and the variance of the ellipticity distribution of the galaxy population.

3.3 Simulations for Pipeline Calibration

In weak-lensing analyses, a good shear measurement method should be able to accurately extract the shape information from the observed galaxy images that are known to be affected by different effects, such as pixelization, PSF-convolution and noise. During the past decade, a number of collaborations have been built up to improve the accuracy and reliability of different weak-lensing measurement methods using simulations. The Shear TEsting Program[9] (STEP I & II, Heymans et al. 2006; Massey et al. 2007) was set for a blind challenge. It produced a large volume of images containing a mixture of stars and simple galaxies. Participants were asked to run object detection software to identify stars and galaxies from noisy data. The simulated images were smoothed and distorted by a PSF convolution kernel. The simplified shear and PSF from STEP did not vary across an image, but this known fact was not allowed to be used by participants in the process of shear measurements from simulations. Different sets of simulated images were produced by applying different combinations of a constant PSF with different rotations and a constant input shear. STEP2 considered more realistic and more complex galaxy morphologies and built larger simulations to improve the measurement precision. Different shear measurement methods have been tested in STEP resulting in significant progress in the development of shear measurement techniques.

With the successful experience of the STEP program, GRavitational lEnsing Accuracy Testing[10] (GREAT08 & 10, Bridle et al. 2009, 2010; Kitching et al. 2011), also a blind challenge, was further designed to measure varying image distortions in the presence of a variable PSF, pixelization and noise. Different from STEP, the GREAT08 Challenge provided position information for sets of non-overlapping galaxies in order to focus on the issue of inferring shear from a given PSF with different

[9] *http://www.roe.ac.uk/ heymans/step/cosmic_shear_test.html*
[10] *http://www.greatchallenges.info/*

noise levels. Both galaxy and star images are produced. GREAT10 extended the challenge by spatially varying both the shear and the PSF across astronomical images. The lensing shear signals caused by LSSs are not constant across the sky. Their spatial variation reflects the non-uniform matter distribution in the Universe. On the other hand, the variation of PSF arises from effects from the atmosphere and telescope optics. From the GREAT10 Challenge, it was found that the best shear measurement methods can achieve an accuracy with average biases on the level of sub percent. The results also showed that for most of the methods, the accuracy strongly depends on the S/N level. In addition, there is also a weak dependence of the accuracy on the type and size of galaxies.

The above challenges demonstrate that the *lens*fit method performs better than KSB+ and Shapelets, especially for data with low S/N. Its overall accuracy can reach a level of 1% for shear estimates calculated by a weighted average over individual shape measurements from different exposures.

3.4 Systematic Uncertainties

With the increase of survey areas and the improvement of image qualities, statistical uncertainties of shear measurements have been significantly reduced. As a result, it has become more and more crucial that systematic errors be understood and even quantified. Systematic errors can come from any step in the process from data reduction to shear measurement. An inappropriate data reduction process, such as astrometric and photometric calibration; reprojection, resampling and coadding of exposures; masking cosmic rays, tracks left by satellites, etc., can introduce errors. Problems in the process of shear measurement, e.g., inaccurate PSF modeling and correction, can also generate severe systematic effects. As discussed in Sections 3.1 and 3.2, systematics from the data reduction and shear measurement themselves can be reduced by increasing our understandings of the observed images and further improving the reduction pipeline, manually checking the auto masks and properly modeling a PSF (e.g., Rowe 2010). For example, by assuming that a PSF varies in a relatively systematic way from exposure to exposure, it is possible to describe the PSF with a high number density of stars and to decompose the observed PSF patterns into their principal components (Jarvis & Jain 2004).

While observational data processing is critical, physical effects can also contaminate weak-lensing analyses. Arising from environmental tidal effects, the intrinsic alignment of close pairs of galaxies, denoted as II, is one of the important physical systematics. For a deep weak-lensing survey, the contaminations of II to cosmic-shear 2-point correlation signals are on the level of a few percents (Pen et al. 2000; Brown et al. 2002). Such contaminations can be significantly reduced by choosing galaxy pairs from two different redshift bins, using the information of photometric redshifts, in two-point correlation analyses.

Hirata & Seljak (2004) point out another type of alignment. The shape of a galaxy is correlated with its local surrounding density field. On the other hand, this density field can generate lensing shear effects on background galaxies. Therefore there exists a background galaxy-foreground galaxy shear-shape alignment, denoted as GI. If a foreground galaxy has an intrinsic shape that is linearly correlated with its local tidal field, the GI alignment contributes negatively to the cosmic-shear two-point correlations, and has to be properly taken into account. The correlation of galaxy shapes and their local density field can be measured by the cross correlation of galaxy ellipticities and their number densities assuming a bias factor between the galaxy number distribution and the underlying density perturbation field (Hirata et al. 2007; Joachimi et al. 2011). The GI contamination increases significantly if a tomographic cosmic shear analysis is applied. Different methods to minimize the impacts of GI on weak-lensing analyses have been proposed, and a detailed introduction can be found in Heymans et al. (2013).

Uncertainties of photometric redshift (photo-z) estimation are another source of systematic errors. Because lensing signals strongly depend on the distances to lens, to source, and between lens and source, the accuracy of photo-z can considerably affect the uncertainties of cosmological inferences from weak-lensing studies. Modern surveys are designed with multiple-band observations for estimating photo-z for individual galaxies. Different codes, e.g., Hyperz (Bolzonella et al. 2000), BPZ (Benítez 2000), and Le PHARE[11], have been developed. Hildebrandt et al. (2012) use BPZ to estimate photo-z for galaxies in CFHTLenS. They discuss different ways of improving the photo-z estimation. For instance, the photometric zero-points are re-calibrated using spectroscopy redshift information in the fields. They also modify the prior to avoid the systematic overestimation of photo-z at low redshift. The homogenization of the PSF between different bands improves the photo-z accuracy, particularly for faint galaxies that are small and their flux measurements are affected more by PSF effects. The effects of photo-z uncertainties on weak-lensing cosmological studies have been investigated extensively (e.g., Ma et al. 2006). We will come back to this in Section 5.

4 COSMOLOGICAL APPLICATIONS OF WEAK-LENSING EFFECTS

4.1 Cluster Studies

Clusters of galaxies are the largest virialized objects in the Universe. Their total mass is typically $\sim 10^{14} - 10^{15} M_\odot$, and the baryon-to-dark matter mass ratio is $\sim 15\%$, approximately the same as the cosmological ratio. Besides having a large number of galaxies, the baryonic matter in a cluster is dominantly in the form of diffuse hot gas with a typical temperature of $\sim 10^7 - 10^8$ K. Clusters of galaxies play a very important role in the hierarchy of LSSs. From a theoretical point of view, their formation and evolution are sensitive to underlying cosmological models. Observationally, they can be probed by multiple means, optical for member galaxies, X-ray (e.g., Rosati et al. 2002) and Sunyaev-Zeldovich effects (e.g., Carlstrom et al. 2002) for hot gas, and gravitational lensing effects for their dark matter distribution (e.g. Bartelmann & Schneider 2001). Therefore clusters of galaxies are regarded as critical objects in cosmological studies.

Gravitational lensing effects have played important roles in cluster studies, especially in constraining the mass distribution of their dark matter halos. Here we mainly focus on weak-lensing effects, which are particularly useful in understanding the overall dark matter distribution of clusters out to their virial radii. A more complete review, including topics related to strong lensing, can be found in Kneib & Natarajan (2011).

For massive clusters of galaxies, weak-lensing analyses for individual ones are observationally possible by accurately measuring the shapes of a large number of source galaxies behind them. Because both the shear and the convergence depend on the lensing potential, in principle the convergence field κ, directly linked to the 2D projected mass distribution of clusters, is reconstructable from the shear components $\boldsymbol{\gamma}$ estimated from the measured shapes of source galaxies. Specifically, from the definition of κ and $\boldsymbol{\gamma}$ in terms of the lensing potential, it is shown that in the Fourier space, we have (Kaiser & Squires 1993, KS)

$$\tilde{\kappa}(\boldsymbol{k}) = \frac{k_1^2 - k_2^2}{k^2}\tilde{\gamma}_1(\boldsymbol{k}) + \frac{2k_1k_2}{k^2}\tilde{\gamma}_2(\boldsymbol{k})\,, \tag{55}$$

where $k^2 = k_1^2 + k_2^2$. This corresponds to the real space relation, subject to an arbitrary constant (namely the mass-sheet degeneracy),

$$\kappa(\boldsymbol{\theta}) = -\frac{1}{\pi}\int d^2\boldsymbol{\theta}'\Re\Big[D(\boldsymbol{\theta}-\boldsymbol{\theta}')\boldsymbol{\gamma}^*(\boldsymbol{\theta}')\Big]\,, \tag{56}$$

where the kernel $D(\boldsymbol{x}) = (x_1^2 - x_2^2 + 2ix_1x_2)/|x|^4$, and $\Re$ is for the real part (Bartelmann 1995).

[11] *www.lam.oamp.fr/arnouts/LE_PHARE.html*

In reality, however, the shear information can only be estimated discretely from source galaxies. The measured complex ellipticity $\boldsymbol{\epsilon}$ ($|\boldsymbol{\epsilon}| = (1 - b/a)/(1 + b/a)$) of a galaxy is related to the lensing effect by

$$\boldsymbol{\epsilon} = \begin{cases} \frac{\boldsymbol{\epsilon}_{\rm s}+\boldsymbol{g}}{1+\boldsymbol{g}^*\boldsymbol{\epsilon}_{\rm s}} & \text{for } |\boldsymbol{g}| \le 1 \,, \\ \\ \frac{1+\boldsymbol{g}\boldsymbol{\epsilon}_{\rm s}^*}{\boldsymbol{\epsilon}_{\rm s}^*+\boldsymbol{g}^*} & \text{for } |\boldsymbol{g}| > 1 \,, \end{cases} \tag{57}$$

where $\boldsymbol{\epsilon}_{\rm s}$ is the intrinsic ellipticity of the galaxy and $\boldsymbol{g} = \boldsymbol{\gamma}/(1-\kappa)$ is the reduced shear at the position of the galaxy. Different from $\boldsymbol{e}$ in the left part of Equation (44), here the complex $\boldsymbol{\epsilon}$ is defined as (e.g., Seitz & Schneider 1997)

$$\boldsymbol{\epsilon} = \frac{Q_{11} - Q_{22} + 2iQ_{12}}{Q_{11} + Q_{22} + 2\sqrt{Q_{11}Q_{22} - Q_{12}^2}} \,, \tag{58}$$

where Q_{ij} are the weighted quadrupole moments given in the right part of Equation (44). The intrinsic $\boldsymbol{\epsilon}_{\rm s}$ can be much larger than the lensing signals we are interested in, and they can induce a large noise in the reconstructed convergence field. Proper treatments to suppress the noise are thus crucially important in the convergence reconstruction. Furthermore, it is shown that in the case of no intrinsic alignments for source galaxies, the average $\langle\boldsymbol{\epsilon}\rangle$ gives rise to an unbiased estimate of $\langle\boldsymbol{g}\rangle$ (in non-critical regions), rather than $\langle\boldsymbol{\gamma}\rangle$ (Seitz & Schneider 1997). Therefore an additional complication occurs in the convergence reconstruction particularly in cluster regions given the nonlinear relation between $\boldsymbol{g}$ and $\boldsymbol{\gamma}$. Limited observing field and masking out bad data can lead to artificial boundary effects in the reconstruction. Local reconstruction methods have been proposed to reduce the boundary effects, which involve the use of the derivatives of the shears (e.g., Bartelmann 1995; Seitz & Schneider 1996). With developments in instrumentation, the current state-of-the-art wide field imaging facilities can have a field of view close to $1 \times 1\,\deg^2$. Given that the angular radius of a typical cluster at $z \sim 0.2$ is $\sim 10'$, the boundary effects due to the limited field of view have been significantly reduced.

On the other hand, noise is always a concern. To avoid the problem of overfitting in the convergence reconstruction, certain regularization procedures for noise suppression are necessary (e.g., Kaiser & Squires 1993; Bartelmann 1995; Bartelmann et al. 1996). One straightforward approach is to first smooth the observed $\boldsymbol{\epsilon}$ with a suitable smoothing scale to get the average $\langle\boldsymbol{\epsilon}\rangle \approx \boldsymbol{g}$. From that, the smoothed convergence can be reconstructed either using the nonlinear KS method (Kaiser & Squires 1993; Squires & Kaiser 1996; Seitz & Schneider 1997) or the maximum likelihood method by χ^2 fitting to the smoothed reduced shear field to derive the lensing potential (e.g., Bartelmann et al. 1996). In this approach, the residual noise depends on the smoothing function and the scale, and can be approximately described by a Gaussian random field due to the central limit theorem (e.g., van Waerbeke 2000; Fan 2007). Another approach, named entropy-regularized maximum likelihood reconstruction, introduces an entropy term in $\ln(L)$, the logarithm of the likelihood function (e.g., Wallington et al. 1994, 1996; Squires & Kaiser 1996; Bridle et al. 1998; Seitz et al. 1998; Starck et al. 2006; Jee et al. 2007; Jullo et al. 2014). This entropy term plays a role that disfavors strong small-scale structures presumably from noise. With suitable choices of the regularization entropy, the noise can be effectively suppressed. On the other hand, the left-over noise can be highly non-Gaussian resulting in some complications in analyses of statistical error (e.g., Jiao et al. 2011; Jullo et al. 2014).

Non-parametric lensing reconstruction of the mass distribution for clusters of galaxies is important for revealing complicated structures therein. The lensing study of the Bullet Cluster is an excellent example, which shows a clear separation between the total mass density distribution and the gas distribution, providing supporting evidence for the existence of dark matter (e.g., Clowe et al. 2006; Paraficz et al. 2012).

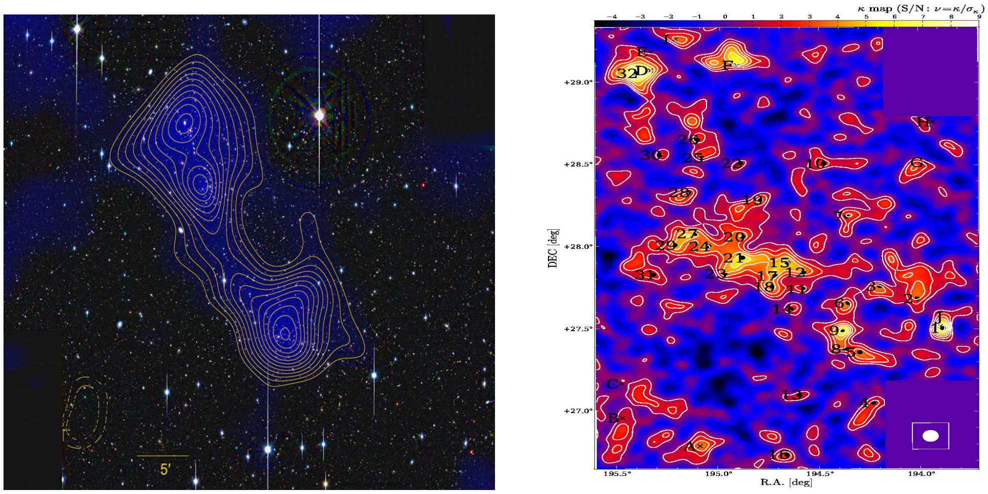

Fig. 8 *Left*: mass distribution of Abell 222/223 system reconstructed from weak-lensing shear measurements, reproduced from figure 1 in Dietrich et al. (2012b) with permission from the authors and by permission of Nature Publishing Group. *Right*: mass distribution of the Coma cluster from weak-lensing shear measurements, reproduced from fig. 3 in Okabe et al. (2014) with permission from N. Okabe and T. Futamase.

Figure 8 presents two other examples. The left panel shows the mass distribution in the Abell 222/223 system from weak-lensing analyses of Dietrich et al. (2012b), where the filamentary structures between the two clusters are clearly seen at the S/N of $\sim 4\sigma$. The right panel shows the recent weak-lensing studies of the nearby Coma cluster with Subaru/Suprime-Cam from Okabe et al. (2014). The high quality observational data reveal abundant substructures in Coma.

On the other hand, for quantitative constraints on the mass distribution of clusters of galaxies, some simplifications are usually applied. For a spherically averaged mass distribution with its center at $\theta = 0$, it is shown that (e.g., Bartelmann & Schneider 2001)

$$\langle \gamma_{\mathrm{t}} \rangle(\theta) = \bar{\kappa}(<\theta) - \bar{\kappa}(\theta)\,, \tag{59}$$

where $\langle \gamma_{\mathrm{t}} \rangle(\theta)$ is the azimuthally averaged tangential shear component at θ, and $\bar{\kappa}(<\theta)$ and $\bar{\kappa}(\theta)$ are the average κ within θ and at θ, respectively. The corresponding parameter-free ζ-statistics has been proposed to measure the 1D mass distribution of dark matter halos, which is given by (Fahlman et al. 1994)

$$\begin{aligned} \zeta(\theta, \theta_{\mathrm{m}}) &= \bar{\kappa}(<\theta) - \bar{\kappa}(\theta < \theta' < \theta_{\mathrm{m}}) \\ &= \frac{2}{1 - \theta^2/\theta_{\mathrm{m}}^2} \int_{\theta}^{\theta_{\mathrm{m}}} d\ln\theta' \langle \gamma_{\mathrm{t}} \rangle(\theta')\,. \end{aligned} \tag{60}$$

It gives the mass distribution within θ subject to a boundary term $\bar{\kappa}(\theta < \theta' < \theta_{\mathrm{m}})$, and can be obtained directly from γ_{t} within the annulus of $\theta < \theta' < \theta_{\mathrm{m}}$. A further improved statistics, namely the ζ_{c}-statistics, is defined by $M_{\zeta_{\mathrm{c}}}(<\theta) = \pi\theta^2 \Sigma_{\mathrm{cr}} \zeta_{\mathrm{c}}(\theta, \theta_{\mathrm{inn}}, \theta_{\mathrm{out}})$, where $\zeta_{\mathrm{c}}(\theta, \theta_{\mathrm{inn}}, \theta_{\mathrm{out}})$ is given by (e.g., Clowe et al. 2000)

$$\begin{aligned} \zeta_{\mathrm{c}}(\theta, \theta_{\mathrm{inn}}, \theta_{\mathrm{out}}) &= \bar{\kappa}(<\theta) - \bar{\kappa}(\theta_{\mathrm{inn}} < \theta' < \theta_{\mathrm{out}}) \\ &= 2\int_{\theta}^{\theta_{\mathrm{inn}}} d\ln\theta' \langle \gamma_{\mathrm{t}} \rangle(\theta') + \frac{2}{1 - \theta_{\mathrm{inn}}^2/\theta_{\mathrm{out}}^2} \int_{\theta_{\mathrm{inn}}}^{\theta_{\mathrm{out}}} d\ln\theta' \langle \gamma_{\mathrm{t}} \rangle(\theta')\,, \end{aligned} \tag{61}$$

where $\theta_{\rm inn}$ and $\theta_{\rm out}$ are the inner and outer radii of the background annulus, respectively. It is seen that $M_{\zeta_c}(<\theta)$ presents the lower bound of the projected mass within θ subject to a boundary term $\pi\theta^2\bar{\kappa}(\theta_{\rm inn}<\theta'<\theta_{\rm out})$, where $\bar{\kappa}(\theta_{\rm inn}<\theta'<\theta_{\rm out})$ is independent of θ. Applying such statistics in real observations, however, it should be noted again that the average of the tangential component of the observed $\boldsymbol{\epsilon}$ gives an estimate of the reduced shear $-\langle g_{\rm t}\rangle$. In cluster regions, the difference between $g_{\rm t}$ and $\gamma_{\rm t}$ is not negligible, and iterative procedures are needed to account for this nonlinearity (e.g., Clowe et al. 2000).

To further quantify the density profile of dark matter halos, parametric models are often adopted to fit either to $M_{\zeta_c}(<\theta)$ or more directly to the reduced shear profile $g_{\rm t}$ (e.g., Okabe et al. 2010; Oguri et al. 2010). The derived parameters are then compared with cosmological predictions aiming to reveal the underlying mechanism for the formation and evolution of dark matter halos, including the properties of dark matter particles as well as the astrophysical processes affecting their formation and evolution (e.g., Umetsu & Broadhurst 2008; Broadhurst et al. 2008; Okabe et al. 2010, 2013; Oguri et al. 2010, 2012; Kneib & Natarajan 2011; Hoekstra et al. 2013; Sereno & Covone 2013).

In the cold dark matter scenario, numerical simulations reveal an approximate universality for the density profile of dark matter halos (e.g., Navarro et al. 1996, 1997; Moore et al. 1999; Jing 2000; Gao et al. 2008; Zhao et al. 2009; Navarro et al. 2010; Gao et al. 2012; Ludlow et al. 2013). Different fitting models have been proposed to describe such profiles (e.g., Navarro et al. 1996, 1997; Hernquist 1990; Einasto 1965; Retana-Montenegro et al. 2012). Among others, the Navarro-Frenk-White density profile (NFW) is a frequently used one given by Navarro et al. (1996, 1997)

$$\rho(r)=\frac{\rho_{\rm s}}{r/r_{\rm s}(1+r/r_{\rm s})^2}\,, \tag{62}$$

where $\rho_{\rm s}$ and $r_{\rm s}$ are the characteristic density and scale of a halo. Given the mass of the halo M_Δ, the halo radius is defined by $M_\Delta=(4\pi/3)\Delta\rho_{\rm crit}r_\Delta^3$ with Δ being the average density of dark matter halos within r_Δ with respect to the critical density of the Universe $\rho_{\rm crit}$. For Δ, the spherical collapse model gives rise to $\Delta_{\rm vir}$ for virialized halos corresponding to the virial radius $r_{\rm vir}$ (e.g., Henry 2000). The value $\Delta=200$ has also been adopted often to define M_{200} and r_{200}. With r_Δ, the concentration parameter is given by $c_\Delta=r_\Delta/r_{\rm s}$ with larger c_Δ for a more centrally concentrated density distribution. Studies show that with certain scatters, there is a relation between c_Δ and M_Δ closely reflecting the mass assembly history of dark matter halos (e.g., Navarro et al. 1997; Bullock et al. 2001; Duffy et al. 2008; Zhao et al. 2009; Prada et al. 2012; Bhattacharya et al. 2013; De Boni et al. 2013).

Figure 9 shows the stacked weak-lensing analyses of 50 clusters from Okabe et al. (2013). The upper left panel shows the profile of $\langle\Sigma_+\rangle=\Sigma_{\rm cr}\langle g_{\rm t}\rangle$, where the symbols with error bars are for the observational results and the lines are for the best fit model results. The lower left panel shows the corresponding result by rotating the source galaxies by 45°, indicting possible systematic effects. The right panel presents the derived (c_{200},M_{200}) by fitting the data to the NFW profile, where different lines indicate different simulation results. It is seen that the NFW profile provides an excellent fit to the stacked weak-lensing signals. Noting the differences of the results from different simulations, the fitted parameters (c_{200},M_{200}) are in line with the simulation predictions. On the other hand, there is a tendency that the derived concentration parameter is somewhat higher than that from simulations.

Besides the 1D profile, current weak-lensing observations begin to be able to probe the shape of the mass distribution, which also carries important cosmological information. Figure 10 presents the results from Oguri et al. (2012), who study 25 clusters selected from the Sloan Giant Arcs Survey (SGAS). The mass distribution of the clusters is analyzed by combining the weak-lensing observations with the strong-lensing giant arcs. The left panel shows the weak-lensing convergence and shear maps by stacking the 25 clusters. The position angle of each cluster derived from strong-lensing modeling is aligned before stacking. The elongation of the mass distribution is clearly seen

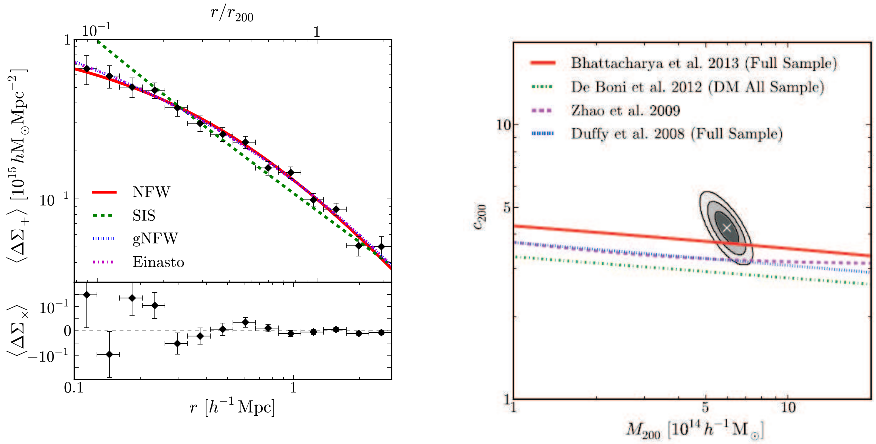

Fig. 9 *Upper left*: the projected density profile from stacked weak-lensing analyses of 50 clusters. Different lines are the best fit results of different models as indicated therein. *Lower left*: the corresponding result with a $45°$ rotation of the source galaxy ellipticities showing the potential systematic effects. *Right*: The derived (c_{200}, M_{200}) from fitting the stacked tangential reduced shear data to the NFW profile. Reproduced from fig. 3 in Okabe et al. (2013) with permission from the authors and by permission of the AAS.

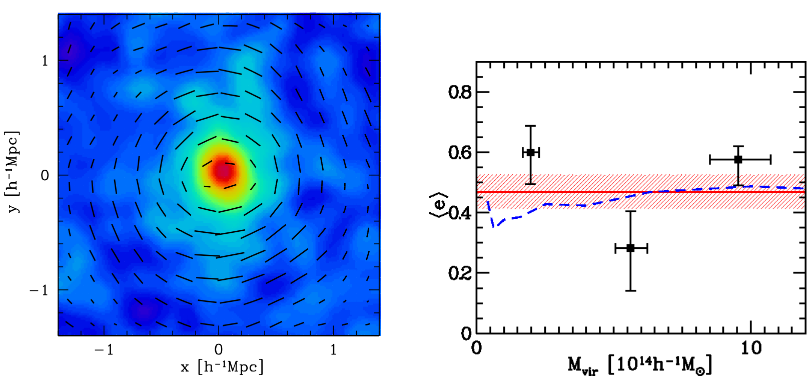

Fig. 10 *Left*: The 2D weak-lensing convergence and shear maps obtained from stacking analyses of 25 clusters, where the position angle of each cluster obtained from strong-lensing modeling is aligned before stacking. Reproduced from the left panel of fig. 11 in Oguri et al. (2012). *Right*: Mean ellipticities of mass distribution obtained from the stacked shear signals in three mass bins, reproduced from the bottom panel of fig. 14 in Oguri et al. (2012). The shaded range indicates the fitting result from the full cluster sample. The blue dashed line is the semi-analytic prediction of Oguri et al. (2012). Printed with permission from the authors and by permission of Oxford University Press on behalf of The Royal Astronomical Society.

in the convergence map. The right panel shows the mean ellipticities of the mass distribution constrained from the stacked shear signals in three different mass bins. The shaded region indicates the results from stacking all the 25 clusters, and the blue dashed line is the semi-analytical prediction of Oguri et al. (2012) taking into account the triaxiality of dark matter halos (Jing & Suto 2002) and the strong-lensing selection bias from the arc cross section. Given the error ranges, the results are in broad agreement with the model prediction based on cold-dark-matter simulations.

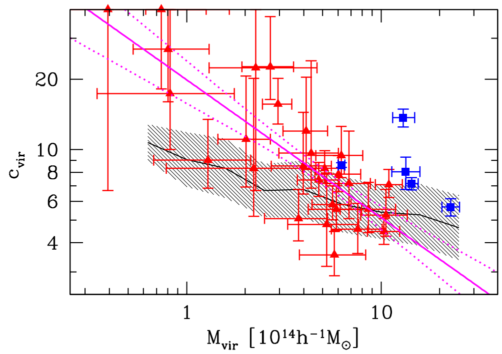

Fig. 11 The $c - M$ relation reproduced from fig. 5 in Oguri et al. (2012). The red symbols are the results from Oguri et al. (2012) obtained by combining the weak-lensing analyses and the strong-lensing giant arcs. The blue squares are for A1689, A370, CL0024 and RXJ1347 from Umetsu et al. (2011) and A383 from Zitrin et al. (2011). The shaded region indicates the theoretical predictions taking into account the strong-lensing selection bias (Oguri et al. 2012). The solid and dotted lines are for the best fit and 1σ range of the fitting results to the red symbols. Printed with permission from the authors and by permission of Oxford University Press on behalf of The Royal Astronomical Society.

Furthermore, with a relatively large cluster sample spanning a sizable mass range, it is becoming possible to observationally constrain the concentration-mass ($c - M$) relation for dark matter halos (e.g., Okabe et al. 2010; Oguri et al. 2012; Sereno & Covone 2013; Auger et al. 2013).

Figure 11 shows the $c - M$ relation from Oguri et al. (2012). The typical redshift for their strong-lensing-selected sample is $z \sim 0.45$. Assuming a power law $c - M$ relation with $c_{\rm vir} = A(M_{\rm vir}/M_{\rm p})^{\alpha}$ and performing a χ^2 fitting with

$$\chi^2 = \Sigma\left\{\left[\log(c_{\rm vir,obs}) - \log(c_{\rm vir,fit})\right]^2/(\sigma_{\rm st}^2 + \sigma_{\rm in}^2)\right\},$$

they obtain $A = 7.7 \pm 0.6$ and $\alpha = -0.59 \pm 0.12$ at $M_{\rm p} = 5 \times 10^{14}\ h^{-1}\ M_{\odot}$. Here $\sigma_{\rm st}$ is the measurement error in $c_{\rm vir,obs}$ for individual clusters, and $\sigma_{\rm in}$ is the intrinsic scatter of $c_{\rm vir}$ taken to be $\sigma_{\rm in} = 0.12$ (Oguri et al. 2012). The value $c_{\rm vir,fit} = A(M_{\rm vir,obs}/M_{\rm p})^{-\alpha}$. The derived slope parameter α is significantly steeper than that of $\alpha \sim -0.1$ predicted by simulations for general halos (e.g., Duffy et al. 2008), and that of $\alpha \sim -0.2$ considering the strong-lensing selection bias (Oguri et al. 2012). The amplitude factor A is also somewhat larger than theoretical predictions. Similar steep $c - M$ relations have also been reported by other weak-lensing studies (e.g., Okabe et al. 2010; Sereno & Covone 2013).

Having shown the fruitful achievements of weak-lensing studies on massive clusters, we note that in order to make detailed comparisons with cosmological predictions and draw physical conclusions, different effects have to be considered carefully. The important aspects related to accurate shape measurements for galaxies have been discussed in Section 3. The distances of the source galaxies, or their redshift information, affect the estimate of $\Sigma_{\rm cr}$, and therefore the physical interpretation of the observed lensing signals. For weak-lensing cluster studies, the separation of the cluster member galaxies from the source galaxy catalog is also important to avoid the dilution effect on lensing signals by the unlensed member galaxies. Color information is crucial in identifying member galaxies for clusters. Analyzing the spatial concentration of galaxies around clusters can also be helpful to suppress the contamination from member galaxies. The availability of photometric redshift for individual galaxies, such as the CFHTLenS data sample (Hildebrandt et al. 2012), can be greatly helpful for determining the distance information and to reduce the contaminations by cluster member galaxies. Detailed discussions on these issues can be found in, e.g., Hoekstra et al. (2013) and Kneib & Natarajan (2011).

Besides, different physical effects, such as the projection effects of correlated and un-correlated LSSs, and the complex mass distribution of clusters themselves, can lead to complications in weak-lensing analyses (Hoekstra 2003; Dodelson 2004; Corless et al. 2009; Hoekstra et al. 2011; Oguri & Hamana 2011). Finding centers of clusters is also an issue (e.g., Oguri et al. 2010; Israel et al. 2010, 2012; Zitrin et al. 2012; Mann & Ebeling 2012; George et al. 2012). Extensive theoretical and simulation studies have been done to explore these effects (e.g., Corless & King 2008; Becker & Kravtsov 2011; Bahé et al. 2012; Giocoli et al. 2012; Dietrich et al. 2012a; Du & Fan 2014).

Aiming to understand the apparently steep $c-M$ relation obtained from a number of weak-lensing observations, Du & Fan (2014) perform systematic studies based on the dark matter halo catalog extracted from the *Millennium Simulation* (Springel et al. 2005). We generate mock weak-lensing data for each individual halo considering different noise levels characterized by $\sigma_{\rm n} = \sigma_{\epsilon_{\rm s}}/\sqrt{n_{\rm g}}$. By assuming a spherical NFW profile and fitting to the reduced tangential shear data $g_{\rm t}$, (c, M) is derived for each halo. Because of the existence of noise, the (c, M) determined from weak-lensing analyses can deviate from the true ones. More importantly, due to the known degeneracy between (c, M) in terms of $g_{\rm t}$ of a halo, a larger determined M generally corresponds to a smaller determined c and vice versa. In other words, the scatters of (c, M) determined by weak lensing for a halo are strongly correlated. Therefore when deriving the $c-M$ relation from a sample of halos studied by weak lensing, an apparently steeper relation than that for the underlying halos is generally expected if the covariance of c and M is not taken into account properly. The larger the noise, the steeper the $c-M$ relation derived by weak lensing. Thus in order to correctly extract the $c-M$ relation from weak-lensing analyses, it is necessary to take the scatters and covariance of (c, M) into consideration rather than to simply fit the observed $c_{\rm obs}$ to $c_{\rm fit} = A(M_{\rm obs}/M_{\rm p})^{\alpha}$ in χ^2 analyses.

Similar to studies for the scaling relation of X-ray clusters taking into account the covariance between the observed luminosity and temperature (e.g., Stanek et al. 2006; Nord et al. 2008), Du & Fan (2014) propose a Bayesian approach to derive the $c-M$ relation from weak-lensing analyses. Assuming $p(c_{\rm obs}, M_{\rm obs}|c_{\rm T}, M_{\rm T})$ to be the probability distribution of the weak-lensing derived $(c_{\rm obs}, M_{\rm obs})$ for a halo with the true concentration and mass $(c_{\rm T}, M_{\rm T})$, and taking into account the intrinsic dispersion of the concentration parameter for halos with a given mass $p(c_{\rm T}|M_{\rm T})$, we have

$$p(c_{\rm obs}, M_{\rm obs}|M_{\rm T}) = \int p(c_{\rm obs}, M_{\rm obs}|c_{\rm T}, M_{\rm T})p(c_{\rm T}|M_{\rm T})\, dc_{\rm T}\,, \tag{63}$$

and

$$p(c_{\rm obs}, M_{\rm obs}) = \frac{\int_{M_{\rm lim}}^{\infty} p(c_{\rm obs}, M_{\rm obs}|M_{\rm T})n(M_{\rm T})\, dM_{\rm T}}{\int_{M_{\rm lim}}^{\infty} n(M_{\rm T})\, dM_{\rm T}}\,, \tag{64}$$

where $n(M_{\rm T})$ is the halo mass function and $M_{\rm lim}$ is the lower limit for mass in the considered sample. Then the probability distribution for $c_{\rm obs}$ given $M_{\rm obs}$ can be written as

$$p(c_{\rm obs}|M_{\rm obs}) = \frac{p(c_{\rm obs}, M_{\rm obs})}{p(M_{\rm obs})}\,, \tag{65}$$

where $p(M_{\rm obs}) = \int p(c_{\rm obs}, M_{\rm obs})\, dc_{\rm obs}$. We can then theoretically predict the expected median value of $c_{\rm obs}$ given $M_{\rm obs}$ by

$$\int_{c_{\rm fit}(M_{\rm obs})} p(c_{\rm obs}|M_{\rm obs})\, dc_{\rm obs} = \frac{1}{2}\,. \tag{66}$$

Note that $c_{\rm fit}(M_{\rm obs})$ depends on the underlying $c-M$ relation for halos through the average $\langle c_{\rm T}\rangle$ in $p(c_{\rm T}|M_{\rm T})$. Therefore for a large sample of observed weak-lensing clusters, the $c-M$ relation can be constrained by minimizing the χ^2 given by

$$\chi^2=\sum_i \frac{[\log c^m_{\rm obs}(M^i_{\rm obs})-\log c_{\rm fit}(M^i_{\rm obs})]^2}{\sigma_i^2}\,, \tag{67}$$

where $c^m_{\rm obs}(M^i_{\rm obs})$ is the median value of $c_{\rm obs}$ for clusters in the mass bin centered at $M^i_{\rm obs}$, and σ_i is the corresponding measurement error for $c^m_{\rm obs}(M^i_{\rm obs})$.

In Du & Fan (2014), we approximate $p(c_{\rm obs}, M_{\rm obs}|c_{\rm T}, M_{\rm T})$ by a 2D Gaussian distribution in $\log$ space given by

$$p(c_{\rm obs}, M_{\rm obs}|c_{\rm T}, M_{\rm T})=\frac{1}{2\pi\sigma_{\rm M}\sigma_{\rm c}\sqrt{1-r^2}}\exp(-T)\,, \tag{68}$$

where

$$\begin{aligned} T \;=\; &\bigg[\sigma^2_{\rm M}\Big(\log c_{\rm obs}-\log c_{\rm T}\Big)^2+\sigma^2_{\rm c}\Big(\log M_{\rm obs}-\log M_{\rm T}\Big)^2 \\ &-2r\sigma_{\rm M}\sigma_{\rm c}\Big(\log c_{\rm obs}-\log c_{\rm T}\Big)\Big(\log M_{\rm obs}-\log M_{\rm T}\Big)\bigg]\Big/2(1-r^2)\sigma^2_{\rm M}\sigma^2_{\rm c}\,. \end{aligned} \tag{69}$$

The parameter $\sigma_{\rm M}$, $\sigma_{\rm c}$ and the correlation coefficient r depend on $M_{\rm T}$ and the noise level. For $p(c_{\rm T}|M_{\rm T})$, it can be written as

$$p(c_{\rm T}|M_{\rm T})=\frac{1}{\sqrt{2\pi}\sigma_{\rm in}}\exp\left[-\frac{(\log c_{\rm T}-\langle\log c_{\rm T}\rangle)^2}{2\sigma^2_{\rm in}}\right], \tag{70}$$

where $\sigma_{\rm in}$ is the intrinsic dispersion of $\log c_{\rm T}$. For $\langle\log c_{\rm T}\rangle$, it is assumed to satisfy the $c-M$ relation $\langle\log c_{\rm T}\rangle=\log A+\alpha\log(M_{\rm T}/M_{\rm p})$ with $M_{\rm p}$ being a chosen pivot mass. It is this (A,α) that we want to constrain from cluster analyses with weak lensing.

In Figure 12, we show the results from simulation studies of Du & Fan (2014). The upper panels are for the results with a simple fitting assuming $c_{\rm fit}=A(M_{\rm obs}/M_{\rm p})^\alpha$ with $M_{\rm p}=10^{14}\ h^{-1}\ M_\odot$. The lower panels show the results with $c_{\rm fit}$ given by Equation (66). It is seen clearly that for the simple fitting that does not account for the correlation between $c_{\rm obs}$ and $M_{\rm obs}$, the derived A and α depend strongly on the noise level σ_n. The higher σ_n is, the steeper the slope parameter α is. In other words, such $c-M$ relation is significantly biased with respect to the underlying $c-M$ relation of dark matter halos. On the other hand, with the Bayesian method taking into account the scatters and the covariance of $c_{\rm obs}$ and $M_{\rm obs}$, the derived A and α agree with the true $c-M$ relation for halos very well (lower panels), demonstrating the great potential to properly constrain the $c-M$ relation with future large weak-lensing surveys.

Since the first detection of weak-lensing signals around massive clusters in the 1990s (Tyson et al. 1990), cluster studies that use weak lensing have advanced tremendously. With future weak-lensing surveys, we can study a large number of clusters. With the thorough understanding of different observational and physical effects, it is highly promising that we can probe the mass distribution of clusters in detail to reveal the underlying cosmological information related to their formation and evolution. Furthermore, the accurate weak-lensing measurement in mass can allow us to calibrate the observable-mass relations for other observations, such as X-ray (e.g., Leauthaud et al. 2010; Mehrtens et al. 2012; Böhringer et al. 2013; Willis et al. 2013) and the Sunyaev-Zeldovich effect (e.g, Reichardt et al. 2013; Hasselfield et al. 2013; Planck Collaboration et al. 2013b). This in turn can significantly improve the cosmological constraints from cluster statistics.

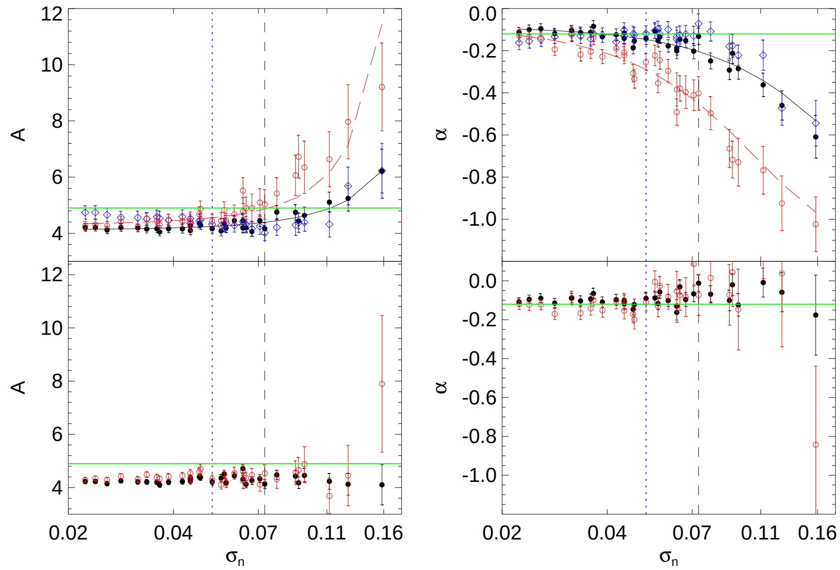

Fig. 12 The $c - M$ relation constrained from simulation studies, reproduced from figs. 7 and 11 in Du & Fan (2014). The left panels show the fitted normalization parameter A vs. the noise level $\sigma_n = \sigma_{\epsilon_s}/\sqrt{n_g}$, and the right panels are for the power index α. The upper panels are for the results with a simple fitting assuming $c_{\rm fit} = A(M_{\rm obs}/M_{\rm p})^{\alpha}$, and the lower panels show the results from the Bayesian analyses with $c_{\rm fit}$ given by Eq. (66). Different colored symbols are for the results from different NFW fittings for individual halos. Printed with permission from the authors and by permission of the AAS.

4.2 Cosmic Shear Correlations

4.2.1 Theoretical considerations

Cosmic shear is the weak-lensing effect caused by LSSs in the Universe. Its signals are very weak, on the order of a percent at angular scales of a few arcminutes. It is impossible to detect cosmic shear from individual galaxies. Instead, cosmic shear signals can be extracted by measuring shear correlations from large samples of galaxies.

As shown previously, weak-lensing shear is a spin-2 field and can be described in a complex form $\boldsymbol{\gamma} = \gamma_1 + i\gamma_2$. The second-order shear correlation function can be defined as

$$\xi_\gamma(\theta) = \Big\langle \boldsymbol{\gamma}(\boldsymbol{\theta}_1) \cdot \boldsymbol{\gamma}^*(\boldsymbol{\theta}_2) \Big\rangle, \tag{71}$$

where $\theta = |\boldsymbol{\theta}_1 - \boldsymbol{\theta}_2|$ is the separation between a pair of galaxies located at $\boldsymbol{\theta}_1$ and $\boldsymbol{\theta}_2$, respectively. The average is taken over all the galaxy pairs with the separation of θ.

To analyze the second-order shear correlations for pairs of galaxies, it is convenient to define the shear of a galaxy in its pair frame with respect to the line connecting the two galaxies. In this frame, the shear of a galaxy is written as $\boldsymbol{\gamma} = \gamma_{\rm t} + i\gamma_\times$ with the tangential component $\gamma_{\rm t} = -{\rm Re}(\boldsymbol{\gamma}{\rm e}^{-2i\phi})$ and cross component $\gamma_\times = -{\rm Im}(\boldsymbol{\gamma}{\rm e}^{-2i\phi})$ (e.g., Bartelmann & Schneider 2001). Here ϕ is the polar angle of the line connecting the two galaxies. We then have the correlation functions $\xi_{\rm tt}$ and $\xi_{\times\times}$ given by, respectively,

$$\xi_{\rm tt}(\theta) = \Big\langle \gamma_{\rm t}(\boldsymbol{\theta}_1)\gamma_{\rm t}(\boldsymbol{\theta}_2) \Big\rangle, \tag{72}$$

and

$$\xi_{\times\times}(\theta) = \left\langle \gamma_\times(\boldsymbol{\theta}_1)\gamma_\times(\boldsymbol{\theta}_2) \right\rangle . \tag{73}$$

From $\xi_{\rm tt}$ and $\xi_{\times\times}$, we can further define

$$\xi_\pm(\theta) = \xi_{\rm tt}(\theta) \pm \xi_{\times\times}(\theta) . \tag{74}$$

In the weak-lensing regime where the lensing potential is determined by the convergence κ under the Born approximation, only the E-mode of the lensing shear is expected, and the B-mode should be identically zero (e.g., Crittenden et al. 2002). Therefore it is desirable to decompose the correlation functions into E-mode and B-mode correlations. All the lensing information should be contained in the E-mode correlation, and the B-mode one should contain only noise. The E/B-mode decomposition provides an important means to test for the existence of systematic errors. The E-mode and B-mode correlation functions are given by (e.g., Crittenden et al. 2002; Schneider et al. 2002b; Pen et al. 2002)

$$\xi_{\rm E}(\theta) = \frac{\xi_+(\theta) + \xi'(\theta)}{2} , \tag{75}$$

and

$$\xi_{\rm B}(\theta) = \frac{\xi_+(\theta) - \xi'(\theta)}{2} , \tag{76}$$

with

$$\xi'(\theta) = \xi_-(\theta) + 4\int_\theta^\infty \frac{d\theta'}{\theta'}\xi_-(\theta') - 12\theta^2 \int_\theta^\infty \frac{d\theta'}{\theta'^3}\xi_-(\theta') . \tag{77}$$

As shown in Section 2.3, theoretically, the shear power spectrum, which is identical to the convergence power spectrum $P_\kappa(l)$, is of great importance. In the ideal case without B-mode contaminations, it is the Fourier transform of the two-point shear (convergence) correlation function (2PCFs) given by

$$\langle \boldsymbol{\gamma}(\mathbf{0})\boldsymbol{\gamma}^*(\boldsymbol{\theta})\rangle = \xi_+(\theta) = \int_0^\infty \frac{dl\, l}{2\pi} J_0(l\theta)P_\kappa(l) . \tag{78}$$

For ξ_-, it is

$$\xi_-(\theta) = \int_0^\infty \frac{dl\, l}{2\pi} J_4(l\theta)P_\kappa(l) . \tag{79}$$

Here J_0 and J_4 are Bessel functions.

From Equation (43), it is seen that $P_\kappa(l)$ can be written as a projection of the 3D power spectrum of dark matter perturbations P_δ along the line of sight. This projection is approximated as an integral over the comoving radial distances χ from the observer out to the limiting distance $\chi_{\rm H}$ of the survey by using Limber's equation. The convergence power spectrum depends on the geometrical factor $f_{\rm K}(\chi)$ and the linear growth factor $G(z)$ which is contained in the power spectrum of dark matter perturbations P_δ, following a simple relation $P_\delta \propto G^2(z)$ on large scales. Both $f_{\rm K}(\chi)$ and $G(z)$ are sensitive to cosmological parameters, including the properties of dark energy. The nonlinear power spectrum P_δ cannot be easily expressed by a simple theoretical formula. As calibrated by simulations, different methods have been developed to calculate P_δ (e.g., Peacock & Dodds 1996; Smith et al. 2003; Lawrence et al. 2010; Heitmann et al. 2014).

The decomposition of the E/B-mode can also be achieved by analyzing the variance of the aperture mass defined by Schneider (1996) and Schneider et al. (1998)

$$M_{\rm ap}(\boldsymbol{\theta}_0, \theta) = \int d^2\boldsymbol{\theta''}\kappa(\boldsymbol{\theta}'')U\Big(|\boldsymbol{\theta}'' - \boldsymbol{\theta}_0|, \theta\Big) , \tag{80}$$

where U is a compensated filter satisfying

$$\int_0^{\theta} d\theta'\, \theta' U(\theta', \theta) = 0 \text{ for } \theta' \leq \theta\,. \tag{81}$$

From the physical relation between κ and $\boldsymbol{\gamma}$, Equation (80) is equivalent to filtering the tangential shear field $\gamma_{\rm t}$ with respect to $\boldsymbol{\theta}_0$ using a filter Q, given by Schneider et al. (1998)

$$M_{\rm ap}(\boldsymbol{\theta}_0, \theta) = \int d^2\boldsymbol{\theta''} \gamma_{\rm t}(\boldsymbol{\theta''}) Q\Big(|\boldsymbol{\theta''} - \boldsymbol{\theta}_0|, \theta\Big)\,, \tag{82}$$

and

$$Q(\theta', \theta) = \frac{2}{\theta'^2} \int_0^{\theta'} d\theta''\, \theta'' U(\theta'', \theta) - U(\theta', \theta) \text{ for } \theta' \leq \theta\,. \tag{83}$$

Therefore in the cosmic shear regime with $\kappa \ll 1$ and $\gamma \ll 1$, $M_{\rm ap}$ can be estimated directly from the tangential component of the observed ellipticities of source galaxies. The variance of $M_{\rm ap}$ can be written in terms of the covergence power spectrum

$$\left\langle M_{\rm ap}^2 \right\rangle (\theta) = \int \frac{{\rm d}\ell\, \ell}{2\pi} P_\kappa(\ell) \hat{U}^2(\theta \ell)\,, \tag{84}$$

where $\hat{U}$ is the Fourier transform of the filter U. Similarly, we can define $M_\times$ by

$$M_\times(\boldsymbol{\theta}_0, \theta) = \int d^2\boldsymbol{\theta''} \gamma_\times(\boldsymbol{\theta''}) Q(|\boldsymbol{\theta''} - \boldsymbol{\theta}_0|, \theta)\,. \tag{85}$$

It is shown that there is no E-mode contribution in $M_\times$ (Crittenden et al. 2002). Therefore $\langle M_\times^2 \rangle(\theta)$ can be used to check possible systematics in lensing measurements.

While the two-point shear correlation/power spectrum analyses carry important cosmological information, they cannot reveal the non-Gaussian nature of LSSs arising from nonlinear gravitational interactions. The third-order cosmic shear correlations and the corresponding bispectrum are the lowest-order measure of the non-Gaussianity of LSSs (e.g., Bernardeau et al. 1997; van Waerbeke et al. 1999; Van Waerbeke et al. 2001).

The bispectrum B_κ of the convergence is defined by (e.g. Schneider et al. 2005)

$$\Big\langle \hat{\kappa}(\boldsymbol{l}_1) \hat{\kappa}(\boldsymbol{l}_2) \hat{\kappa}(\boldsymbol{l}_3) \Big\rangle = (2\pi)^2 \delta_D(\boldsymbol{l}_1 + \boldsymbol{l}_2 + \boldsymbol{l}_3) B_\kappa(\boldsymbol{l}_1, \boldsymbol{l}_2, \boldsymbol{l}_3)\,, \tag{86}$$

and $B_\kappa(\boldsymbol{l}_1, \boldsymbol{l}_2, \boldsymbol{l}_3)$ can be written as

$$B_\kappa(\boldsymbol{l}_1, \boldsymbol{l}_2, \boldsymbol{l}_3) = B_\kappa(\boldsymbol{l}_1, \boldsymbol{l}_2) + B_\kappa(\boldsymbol{l}_2, \boldsymbol{l}_3) + B_\kappa(\boldsymbol{l}_3, \boldsymbol{l}_1)\,, \tag{87}$$

where δ_D is the 2D Dirac delta function. Thus the bispectrum is non-zero only in the case that the three wave vectors $(\boldsymbol{l}_1, \boldsymbol{l}_2, \boldsymbol{l}_3)$ form a closed triangle. Under the Limber approximation, the relation between B_κ and the 3D bispectrum B_δ of matter density perturbations is similar to that of the power spectrum, and is given by (e.g., Sato & Nishimichi 2013)

$$B_\kappa(\boldsymbol{l}_1, \boldsymbol{l}_2, \boldsymbol{l}_3) = \frac{27 H_0^6 \Omega_{\rm m}^3}{8} \int_0^{\chi_{\rm H}} d\chi' \frac{\bar{G}^3(\chi')}{a^3(\chi') f_{\rm K}(\chi')} B_\delta \left[\frac{\boldsymbol{l}_1}{f_{\rm K}(\chi')}, \frac{\boldsymbol{l}_2}{f_{\rm K}(\chi')}, \frac{\boldsymbol{l}_3}{f_{\rm K}(\chi')}; \chi' \right], \tag{88}$$

where $B_\delta\Big[\boldsymbol{l}_1/f_{\rm K}(\chi'), \boldsymbol{l}_2/f_{\rm K}(\chi'), \boldsymbol{l}_3/f_{\rm K}(\chi'); \chi'\Big]$ is the 3D bispectrum with $\boldsymbol{k}_i = \boldsymbol{l}_i/f_{\rm K}$ at the cosmic time corresponding to χ', and $\bar{G}$ is given in Equation (42).

In the quasi-linear perturbation regime, B_δ can be computed in terms of the power spectrum (Fry 1984). On highly nonlinear scales, however, it is a challenging task to predict B_δ accurately. Different models have been proposed (e.g., Scoccimarro & Couchman 2001; Pan et al. 2007; Valageas et al. 2012). The hyper-extended perturbation theory (Scoccimarro & Couchman 2001, HEPT) interpolates B_δ between the strongly nonlinear regime and the quasi-linear regime where the second-order perturbation theory is a good approximation. HEPT on very small scales falls back on the stable clustering hypothesis, where clustering is assumed to have reached virial equilibrium (Peebles 1980). The original HEPT bispectrum is based on the nonlinear power spectrum fitting formula from Peacock & Dodds (1996). Sato & Nishimichi (2013) recently show that HEPT can provide a much better fit to the convergence bispectrum with the revised `halofit` version of Takahashi et al. (2012). These revised fitting functions also match the convergence power spectrum more closely.

To probe the bispectrum, the skewness of the aperture mass has been introduced by, e.g., Jarvis et al. (2004) and Pen et al. (2003). Its generalization involves the correlation of the aperture mass for three different smoothing scales, which optimally probes the bispectrum for general triangles. The definition is given by Schneider et al. (2005),

$$\begin{aligned}\left\langle M_{\rm ap}^3\right\rangle(\theta_1,\theta_2,\theta_3) &\equiv \langle M_{\rm ap}(\theta_1)M_{\rm ap}(\theta_2)M_{\rm ap}(\theta_3)\rangle \\ &= \int\frac{{\rm d}^2\boldsymbol{\ell}_1}{(2\pi)^2}\int\frac{{\rm d}^2\boldsymbol{\ell}_2}{(2\pi)^2}\,B_\kappa(\boldsymbol{\ell}_1,\boldsymbol{\ell}_2) \\ &\quad\times\sum_{(i,j,k)\in S_3}\hat{U}(\theta_i|\boldsymbol{\ell}_1|)\,\hat{U}(\theta_j|\boldsymbol{\ell}_2|)\,\hat{U}(\theta_k|\boldsymbol{\ell}_1+\boldsymbol{\ell}_2|)\,,\end{aligned} \tag{89}$$

where S_3 is the symmetric permutation group of (123), and $\hat{U}$ denotes the Fourier transform of the aperture filter U.

There are several advantages of using aperture moments instead of n-point correlation functions. Most importantly, aperture measures are only sensitive to the E-mode of the shear field. They filter out long-wavelength modes where an E-/B-mode separation is not possible given a finite survey volume (Schneider et al. 2010). They are therefore less susceptible to systematics in the data. Furthermore, a theoretical prediction from the convergence bispectrum B_κ can be obtained much easier and faster for the aperture three-point statistics than for the three-point correlation function (Schneider et al. 2005). It is therefore more efficient to use the aperture moments to constrain cosmological parameters where a Monte-Carlo sampling analysis is necessary.

4.2.2 The statistics of cosmic shear

From an observational point of view, the most direct study of weak lensing effects is in real space, by using the shear signals derived from measurements of galaxy ellipticity. It is possible to reconstruct the convergence field from the measured shear field. Such a convergence reconstruction has been performed recently using CFHTLenS data, and moments of the convergence up to order 5 have been measured (Van Waerbeke et al. 2013).

More generally, the two-point shear correlation functions ξ_+ and ξ_- can be estimated in an unbiased way by averaging over pairs of galaxies (Schneider et al. 2002a). It does not require the treatment of masks and smoothing of the shear field, and is given by

$$\hat{\xi}_\pm(\vartheta) = \frac{\sum_{ij} w_i w_j [\varepsilon_{\rm t}(\boldsymbol{\vartheta}_i)\,\varepsilon_{\rm t}(\boldsymbol{\vartheta}_j) \pm \varepsilon_\times(\boldsymbol{\vartheta}_i)\,\varepsilon_\times(\boldsymbol{\vartheta}_j)]}{\sum_{ij} w_i w_j}\,. \tag{90}$$

Here $\varepsilon_{\rm t}$ and $\varepsilon_\times$ are denoted as the tangential and cross components of observed galaxy ellipticities, respectively, and the sum is performed over all galaxy pairs (ij) with angular distance $|\boldsymbol{\vartheta}_i - \boldsymbol{\vartheta}_j|$

within the chosen bin around ϑ. The weight w represents the shear uncertainty of each galaxy in the measurements. With $\hat{\xi}_\pm$, the second-order aperture E-mode $\langle M_{\rm ap}^2 \rangle$ and B-mode $\langle M_\times^2 \rangle$ can further be calculated by Crittenden et al. (2002) and Schneider et al. (2002b),

$$\langle M^2_{{\rm ap},\times} \rangle(\theta) = \frac{1}{2} \sum_i \vartheta_i \, \Delta\vartheta_i \left[T_+(\vartheta_i) \, \hat{\xi}_+(\vartheta_i) \pm T_-(\vartheta_i) \, \hat{\xi}_-(\vartheta_i) \right] , \tag{91}$$

where the functions $T_\pm(x)$ are

$$T_+ = \int_0^\infty {\rm d}t \, J_0(xt) \, \hat{U}^2(t)$$

and

$$T_- = \int_0^\infty {\rm d}t \, J_4(xt) \, \hat{U}^2(t) \, .$$

The three-point correlation functions (3PCFs) are calculated on triangles. They have eight components and can be expressed by four complex *natural components* (Schneider & Lombardi 2003; Zaldarriaga & Scoccimarro 2003; Takada & Jain 2003). An unbiased estimator for the zero-th component is (Schneider & Lombardi 2003)

$$\hat{\Gamma}^{(0)}(\boldsymbol{s},\boldsymbol{t}) = \frac{\sum_{ijk} w_i \, w_j \, w_k \, \varepsilon_i \, \varepsilon_j \, \varepsilon_k \, e^{-6i\alpha}}{\sum_{ijk} w_i \, w_j \, w_k} \, , \tag{92}$$

where ε is the complex ellipticity of galaxies, and $(\boldsymbol{s}, \boldsymbol{t}, \alpha)$ give the chosen configuration of triangles with $\boldsymbol{s}$ and $\boldsymbol{t}$ being the two sides and α being the angle between them. The other three components are estimated as

$$\hat{\Gamma}^{(1)}(\boldsymbol{s},\boldsymbol{t}) = \frac{\sum_{ijk} w_i \, w_j \, w_k \varepsilon_i^* \, \varepsilon_j \, \varepsilon_k \, e^{-2i\alpha}}{\sum_{ijk} w_i \, w_j \, w_k}; \tag{93}$$

$$\hat{\Gamma}^{(2)}(\boldsymbol{s},\boldsymbol{t}) = \frac{\sum_{ijk} w_i \, w_j \, w_k \varepsilon_i \, \varepsilon_j^* \, \varepsilon_k \, e^{-2i\alpha}}{\sum_{ijk} w_i \, w_j \, w_k}; \tag{94}$$

$$\hat{\Gamma}^{(3)}(\boldsymbol{s},\boldsymbol{t}) = \frac{\sum_{ijk} w_i \, w_j \, w_k \varepsilon_i \, \varepsilon_j \, \varepsilon_k^* \, e^{-2i\alpha}}{\sum_{ijk} w_i \, w_j \, w_k}. \tag{95}$$

The third-order aperture E-mode (EEE), B-mode (BBB), and the mixed modes of EEB and EBB can be expressed as different combinations of $\langle M^3 \rangle$, $\langle M^2 M^* \rangle$, $\langle M M^* M \rangle$ and $\langle M^* M^2 \rangle$ where $M = M_{\rm ap} + i M_\times$, and those, in turn, can be obtained through the integrals over $\hat{\Gamma}^{(i)}$ with chosen filter functions. We refer readers to Jarvis et al. (2004) and Schneider et al. (2005) for details. The expectation values of the mixed components EEB and EBB are non-zero only if the E- and B- modes are correlated. For a parity-symmetric shear field, only the EBB component is non-zero (Schneider 2003). However in practice, noise sample variance causes a violation of parity for a given observed region, and all three B-mode related components can be non-zero.

4.2.3 Cosmological applications

The 2PCFs of cosmic shears have been observationally measured since the year 2000. These first detections encouraged early studies with different surveys (e.g., Refregier 2003), including RCS (53 deg^2, Hoekstra et al. 2002), VIRMOS (8.5 deg^2, Van Waerbeke et al. 2005), CTIO (70 deg^2, Jarvis et al. 2006), GaBoDs (13 deg^2, Hetterscheidt et al. 2007) and CFHTLS Deep (4 deg^2, Semboloni et al. 2006). Recently, Schrabback et al. (2010) performed comprehensive second-order analyses of cosmic shear signals by LSSs with COSMOS data (2 deg^2). They showed that the shear signal scales with redshift as expected from the theory of general relativity in the concordance ΛCDM cosmology, including the full cross-correlation signals between different redshift bins. Under the flatness assumption for the Universe, they obtain $\sigma_8(\Omega_{\rm m}/0.3)^{0.51} = 0.75 \pm 0.08$ (68.3% conf.) from lensing alone. They find a negative deceleration parameter q_0 at the 94.3% confidence level using the tomographic lensing analysis without the assumption of flatness and using priors from the HST Key Project for H_0 and $\Omega_{\rm b}h^2$ from constraints on Big Bang nucleosynthesis. This provides independent evidence for the accelerated expansion of the Universe.

Semboloni et al. (2011) present a first detection of the third-order moments of the aperture mass statistics using the same COSMOS data. Their results are reproduced in the left panel of Figure 13. It is seen that the results are in very good agreement with the predictions of the WMAP7 best-fit cosmological model. The combined likelihood analysis of $\langle M_{\rm ap}^3\rangle(\theta)$ and $\langle M_{\rm ap}^2\rangle(\theta)$ improves the cosmological constraints to $\sigma_8(\Omega_{\rm m}/0.3)^{0.50} = 0.69^{+0.07}_{-0.12}$ (reproduced in the right panel of Fig. 13).

CFHTLenS covers 154 deg^2 sky in five optical bands. It gives rise to accurate photometric redshifts and shape measurements for 4.2 million galaxies between redshifts of 0.2 and 1.3. Kilbinger et al. (2013) present the analyses of cosmic shear signals by LSSs using CFHTLenS. They compute the 2D cosmic-shear correlation function over angular scales ranging between $0.8'$ and $350'$. The results are reproduced in the left panel of Figure 14. For a flat ΛCDM model, they obtain the corresponding constraints $\sigma_8(\Omega_{\rm m}/0.27)^{0.6} = 0.79 \pm 0.03$. With the combinations of CFHTLenS with WMAP7, BOSS and an HST distance-ladder prior on H_0, they find $\Omega_{\rm m} = 0.283 \pm 0.010$ and $\sigma_8 = 0.813 \pm 0.014$. The reproduced results are shown in the right panel of Figure 14. Benjamin et al. (2013) measure the shear correlation functions on angular scales in the range $\sim 1 - 40$ arcmin with the same CFHTLenS data, in two broad redshift bins, $0.5 < z_{\rm p} \le 0.85$ and $0.85 < z_{\rm p} \le 1.3$. The auto and cross correlations of the two bins are reproduced in the left panel of Figure 15. They show good agreements with the theoretical predictions of WMAP7. For a flat ΛCDM model, they find $\sigma_8 = 0.771 \pm 0.041$ with a fixed matter density $\Omega_{\rm m} = 0.27$. In combination with WMAP7, BOSS and a prior on H_0 from HST, they obtain $\Omega_{\rm m} = 0.2762 \pm 0.0074$ and $\sigma_8 = 0.802 \pm 0.013$ (reproduced in the right panel of Fig. 15). Fu et al. (2014) measure second- and third-order weak-lensing aperture mass statistics from CFHTLenS and combine them with cosmic microwave background (CMB) anisotropy for cosmological constraints. The results are shown in Figure 16. The third moment is measured with a significance of 2σ (left panel of Fig. 16). Compared to only using second-order correlations, including the third-order statistics improves the constraint on $\Sigma_8 = \sigma_8(\Omega_{\rm m}/0.27)^{\alpha}$ by 10%. The allowed ranges for $\Omega_{\rm m}$ and σ_8 are substantially reduced. Adding second- and third-order CFHTLenS lensing measurements to Planck CMB temperature anisotropy tightens the Planck-only constraints on $\Omega_{\rm m}$ and σ_8 by 26% for flat ΛCDM (middle panel of Fig. 16). For a model without the flatness prior, the joint CFHTLenS-Planck result is $\Omega_{\rm m} = 0.28 \pm 0.02$ with 68% confidence, which shows an improvement of 43% compared to Planck alone (right panel of Fig. 16).

4.3 Peak Statistics

As discussed in Section 4.1, clusters of galaxies are strong sources for generating weak-lensing signals, and they appear as high peaks in weak-lensing maps. Therefore observations of weak lensing can not only be used to study the mass distribution of known clusters, but also provide a unique way to detect clusters blindly (e.g., Tyson 1992; Kruse & Schneider 1999). The feasibility of cluster detections with weak lensing has been demonstrated by different observational analyses (e.g., Miyazaki et al. 2002; Wittman et al. 2006; Gavazzi & Soucail 2007; Miyazaki et al. 2007; Schirmer et al. 2007; Geller et al. 2010; Shan et al. 2012; Hamana et al. 2012; Van Waerbeke et al. 2013; Shan et al. 2013). Figure 17 shows the mass distribution that is reconstructed with weak-lensing analyses from Shan et al. (2012) with CFHTLS (left) and Van Waerbeke et al. (2013) with CFHTLenS (right). Different symbols are explained in the caption. Certain correspondence between the weak-lensing peaks and the clusters identified optically or in X-ray can be seen clearly.

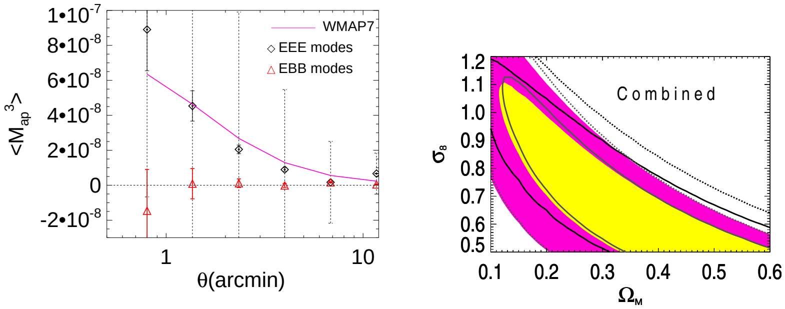

Fig. 13 *Left*: The three-point aperture statistics measured from COSMOS, reproduced from the right panel of fig. 4 in Semboloni et al. (2011). The black diamonds are for $\langle M_{\rm ap}^3 \rangle$ (EEE) and the red triangles are for $\langle M_{\rm ap} M_\times^2 \rangle$ (EBB). Error bars are for statistical errors. The solid line is the WMAP7 model prediction. *Right*: The probability distribution for the parameters $\Omega_{\rm m}$ and σ_8, reproduced from the right panel of fig. 7 in Semboloni et al. (2011). The constraints (*colored regions*) are obtained from the joint measurements of $\langle M_{\rm ap}^2 \rangle(\theta)$ and $\langle M_{\rm ap}^3 \rangle(\theta)$ as compared to that separately from $\langle M_{\rm ap}^2 \rangle(\theta)$ (*inner lines*) and $\langle M_{\rm ap}^3 \rangle(\theta)$ (*outer lines*), respectively. The solid (*dashed*) lines represent the 68.3% (95.5%) level of confidence. Printed with permission from the authors and by permission of Oxford University Press on behalf of The Royal Astronomical Society.

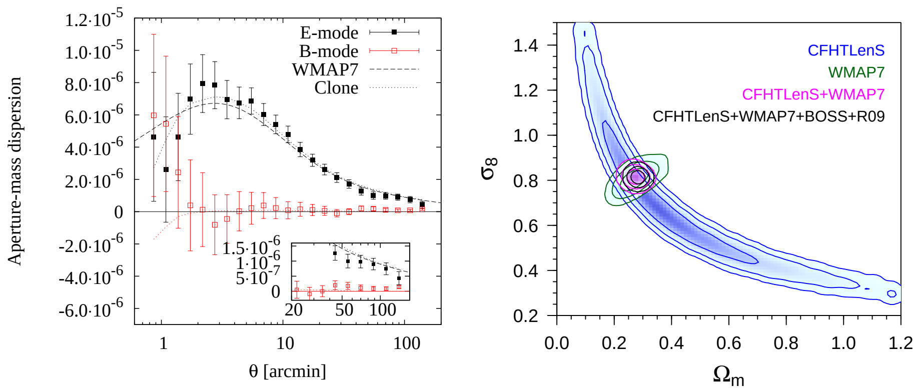

Fig. 14 *Left*: Aperture-mass dispersion of $\langle M_{\rm ap}^2 \rangle$ (E-mode, *black filled squares*) and $\langle M_\times^2 \rangle$ (B-mode, *red open squares*) from CFHTLenS, reproduced from the upper panel of fig. 8 in Kilbinger et al. (2013). The signal is compared to the theoretical prediction for a WMAP7-cosmology (*dashed line*) and the simulation result from Clone lines-of-sight mean signal (*dotted line*). The error bars are the Clone field-to-field rms. *Right*: For the flat ΛCDM model, the marginalized parameter constraints $(\Omega_{\rm m}, \sigma_8)$ (68.3%, 95.5%, 99.7%) from CFHTLenS (*blue contours*), WMAP7 (*green*), CFHTLenS+WMAP7 (*red*) and CFHTLenS+WMAP7+BOSS+R09 (*black*) are shown, reproduced from the upper panel of fig. 10 in Kilbinger et al. (2013), with permission from the authors and by permission of Oxford University Press on behalf of The Royal Astronomical Society.

Being closely associated with mass concentrations, notably clusters of galaxies, weak-lensing peak statistics are anticipated to carry important cosmological information (e.g., Kruse & Schneider 1999; Hamana et al. 2004; Kratochvil et al. 2010; Marian et al. 2013). Particularly, they are more sensitive to massive structures, and thus the non-Gaussian features of the LSSs in the Universe (e.g., Marian et al. 2011). Therefore they are highly complementary to the cosmic shear two-point correlation analyses. To demonstrate the cosmological dependence of weak-lensing peak statistics,

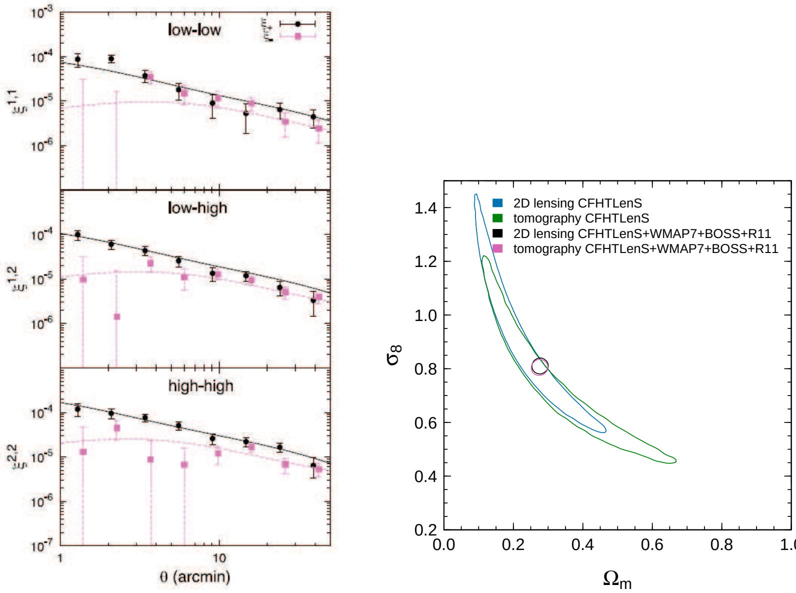

Fig. 15 *Left*: Auto and cross correlations ξ_+ (*filled circles*) and ξ_- (*filled squares*) of two redshift bins measured from CFHTLenS, reproduced from figure 6 in Benjamin et al. (2013). Error bars are the square-root of the diagonal elements of the covariance matrix measured from Clone mock catalogs. Theoretical predictions for the WMAP7 cosmology are presented as lines. *Right*: The marginalized parameter constraints (68.3% conf. level) on $(\Omega_\mathrm{m}, \sigma_8)$ for a flat ΛCDM cosmology: 2D lensing (*blue*), 2-bin tomography (*green*) from CFHTLenS, 2D lensing combined with WMAP7, BOSS and H_0 prior of R11 (*black*), and 2-bin tomography with all combinations (*pink*). Reproduced from figure 8 in Benjamin et al. (2013), with permission from the authors and by permission of Oxford University Press on behalf of The Royal Astronomical Society.

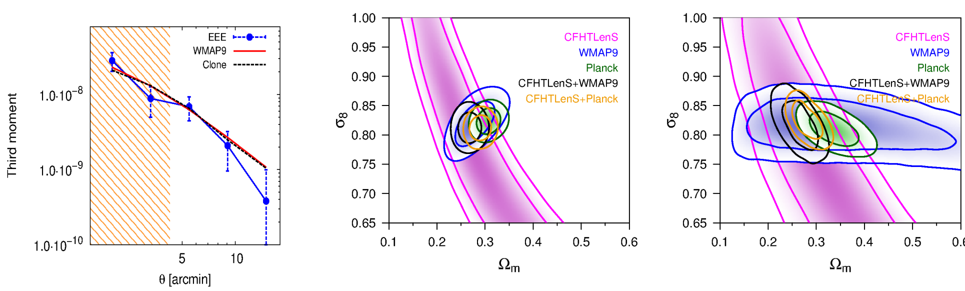

Fig. 16 *Left*: The third-order aperture-mass EEE components as a function of smoothing scale θ, measured from CFHTLenS data. The prediction from WMAP9 is shown as a red solid line and the third moment measured from the Clone is the black dash-dotted curve. *Middle*: Marginalized posterior density contours (68.3%, 95.5%) from CFHTLenS (joint second-order COSEBIs and third-order diagonal aperture-mass; magenta lines), WMAP9 (*blue*), Planck (*green*), CFHTLenS + WMAP9 (*black*) and CFHTLenS + Planck (orange). The flat ΛCDM cosmology is assumed here. *Right*: The corresponding results in the case without the flatness prior. Reproduced from the upper panel of figs. 2 and 11 in Fu et al. (2014), with permission from the authors and by permission of Oxford University Press on behalf of The Royal Astronomical Society.

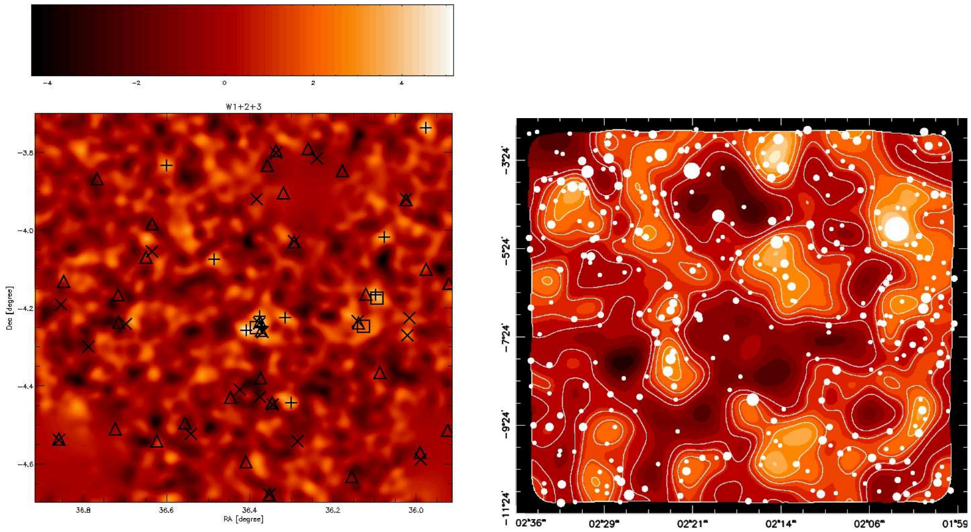

Fig. 17 The weak-lensing reconstructed mass distribution of the CFHTLS W1+2+3 pointing reproduced from fig. 17 in Shan et al. (2012) (*left*), and of the CFHTLenS W1 field reproduced from fig. 8 in Van Waerbeke et al. (2013) (*right*). The color maps (with white contours in the right panel) are the weak-lensing reconstructed convergence maps shown in the S/N. In the left panel, the triangles are for optically detected clusters in the K2 catalog (Thanjavur et al. 2009), the cross symbols are for the X-ray detected clusters (Adami et al. 2011), and the plus and squares symbols are for convergence peaks with S/N>3.5 in maps with Gaussian smoothing scales $\theta_{\mathrm{G}}=1'$ and $\theta_{\mathrm{G}}=2'$, respectively (Shan et al. 2012). In the right panel, the Gaussian smoothing scale is $\theta_{\mathrm{G}}=\sqrt{2}\times 8.9\approx 12.6'$ for the convergence map. The white circles show the predicted peaks from the galaxy distribution with their size indicating the height of the peaks (Van Waerbeke et al. 2013). Note that here the Gaussian smoothing function is taken to have the form $W(\theta)=(1/\pi\theta_{\mathrm{G}}^2)\exp(-\theta^2/\theta_{\mathrm{G}}^2)$. Printed with permission from the authors, and by permission of the AAS (*left*) and of Oxford University Press on behalf of The Royal Astronomical Society (*right*).

we consider the most simple and ideal case assuming a one-to-one correspondence between a weak-lensing convergence peak and a dark matter halo. Then the peak abundance can be theoretically calculated from the mass function of dark matter halos taking into account the lensing efficiency (e.g., Kruse & Schneider 2000; Bartelmann et al. 2001). Specifically, we have (Hamana et al. 2004)

$$N(\nu>\nu_{\mathrm{th}})=\int dz\frac{dV}{d\Omega dz}\int dM\; n_{\mathrm{halo}}(M,z)H_{\mathrm{t}}[\nu(M,z)-\nu_{\mathrm{th}}]\,, \tag{96}$$

where ν stands for the S/N of weak-lensing peaks, $N(\nu>\nu_{\mathrm{th}})$ is the surface number density of peaks with $\nu>\nu_{\mathrm{th}}$, dV and $d\Omega$ are the volume element and the solid angle element of the Universe, respectively, and n_{halo} is the mass function of dark matter halos. The term H_{t} is a Heaviside step function with $H_{\mathrm{t}}(x)=1$ for $x\geq 0$ and $H_{\mathrm{t}}(x)=0$ otherwise, representing the selection function for halos based on their peak weak-lensing signals.

Here the S/N is $\nu=K/\sigma_0$ with K the peak value of the lensing convergence and σ_0 the rms of the noise. As discussed previously, the intrinsic ellipticity plus the uncertainty in shape measurement for a source galaxy is much larger than its weak-lensing signal, thus bringing large noise to the reconstructed convergence map affecting severely the detectability of true peaks. Therefore noise suppression procedures, such as smoothing (e.g., Hamana et al. 2004; Van Waerbeke et al. 2013) and entropy regularization (e.g., Starck et al. 2006), are necessary and σ_0 is the rms of the left-over noise. For the peak signal K of a halo with mass M and at redshift z, it depends on the halo density profile, the redshift information of the lens and the source galaxies through the angular diameter distances, and the noise suppression procedures applied to the convergence. Therefore $K(M,z)$ contains important cosmological information (e.g., Bartelmann et al. 2001; Hamana et al. 2004) and reflects the sensitivity of weak-lensing cluster detection. For the source redshift $z_{\rm s} \sim 1$, the weak-lensing detections are sensitive to clusters at $z \sim 0.2$ (Hamana et al. 2004). For the halo mass function $n_{\rm halo}$, it is directly related to the formation and evolution of dark matter halos and thus sensitive to cosmological models. Given Gaussian linear density perturbations, dynamical models for halo formation, such as the spherical and ellipsoidal collapse models (e.g., Peebles 1980; Bond & Myers 1996), allow us to link the nonlinear formation of dark matter halos to linear density perturbations above a collapse threshold. Then the halo mass function can be theoretically predicted based on properties of linear density perturbations, including the power spectrum and the linear growth factor (e.g., Press & Schechter 1974; Bond et al. 1991; Sheth et al. 2001). While these theoretical models capture the essence of the halo formation, their accuracies are limited by simplified assumptions. Because of its important roles in cosmological studies, accurate modeling of the halo mass function is strongly desired (e.g., Wu & Huterer 2013). With numerical simulations, different fitting models have been proposed to improve the halo mass function (e.g., Sheth & Tormen 1999; Jenkins et al. 2001; Warren et al. 2006; Tinker et al. 2008; Bhattacharya et al. 2011; Watson et al. 2013; Knebe et al. 2013).

From Equation (96), we see that the cosmological dependence of the weak-lensing peak abundance is reflected in the halo mass function, the lensing signal $K(M,z)$ and the volume element dV. In other words, the weak-lensing peak abundance depends both on the structure formation and on the global expansion history of the Universe. This lays the theoretical motivation for probing cosmology with weak-lensing peak statistics. On the other hand, however, the model shown in Equation (96) is a highly idealized one, and many effects can significantly influence weak-lensing peaks. The non-spherical mass distribution of dark matter halos introduces complications in calculating the peak convergence signal K for a halo with given (M,z) (e.g., Tang & Fan 2005; Corless et al. 2009; Hamana et al. 2012). The correlated structures near a halo and non-correlated ones along its line of sight can affect the peak signal K (e.g., Hoekstra 2003; Dodelson 2004; Marian et al. 2010; Hoekstra et al. 2011; Oguri & Hamana 2011; Yang et al. 2011). For relatively low peaks, a large fraction of these do not have dominant halos responsible for their lensing signals. Rather, the projection effects of LSSs along lines of sight contribute coherently to these peaks (e.g., Maturi et al. 2010; Yang et al. 2011). Furthermore, the weak-lensing peak analyses involve, in one way or another, the reconstruction of the convergence field from the measured shapes of source galaxies. The existence of noise in the reconstructed convergence field because of intrinsic ellipticities of source galaxies is therefore inevitable even after the noise suppression treatments. The noise can lead to false peaks from chance alignments of source galaxies, and thus considerably reduce the efficiency of cluster detection (e.g., White et al. 2002; Wittman et al. 2006; Gavazzi & Soucail 2007; Schirmer et al. 2007; Geller et al. 2010). A more subtle effect of noise is that it can also affect the signals of the peaks associated with true dark matter halos, generating not only scatters but also systematic bias (e.g., Fan et al. 2010; Yang et al. 2011). The spatial clustering and the intrinsic alignment of source galaxies can also affect the cosmological interpretations of weak-lensing peak statistics (e.g., Fan 2007; Schmidt & Rozo 2011). Different observational effects should also carefully be taken into account (e.g., VanderPlas et al. 2012; Van Waerbeke et al. 2013; Liu et al. 2014).

Extensive analyses have been performed to explore different effects on weak-lensing peak statistics. In terms of cluster detections, various filtering strategies are developed to optimize weak-lensing signals of clusters (e.g., Schirmer et al. 2004; Hennawi & Spergel 2005; Maturi et al. 2005; Starck et al. 2006; Marian et al. 2012). The aperture mass statistics $M_{\rm ap}$ introduced in Equation (80) can be calculated from the tangential component of the observed ellipticities of source galaxies using a filter Q (Eq. 83). This has been extended to the so called shear-peak statistics where the analyses are done on the basis of the filtered tangential shears defined as

$$\tilde{M}_{\rm ap}(\boldsymbol{\theta}) = \int d^2\boldsymbol{\theta}' \gamma_{\rm t}(\boldsymbol{\theta}') Q(|\boldsymbol{\theta}' - \boldsymbol{\theta}|)$$

with a general filter Q. By choosing an appropriate function Q, e.g., with a similar profile of the halo tangential shear, the S/N of $\tilde{M}_{\rm ap}$ can be maximized for detecting clusters efficiently (e.g., Schneider et al. 1998; Schirmer et al. 2007). An optimal filter can also be found by minimizing the effects both from the noise arising from intrinsic ellipticities and from the projection of LSSs (e.g., Maturi et al. 2005). By incorporating the redshift information of source galaxies, the weak-lensing cluster detection can be further improved by applying a tomographic matched filter (Hennawi & Spergel 2005). For a survey with the source galaxy number density $n_{\rm g} \sim 30$ arcmin^{-2} and the typical source redshift $z_{\rm s} \sim 1$, the S/N $\nu \sim 4$ corresponds to clusters with mass $M \sim 10^{14} M_{\odot}$ at redshift $z \sim 0.2$ with a possible extension to smaller mass and higher redshift depending on the filter optimization (e.g., White et al. 2002; Hamana et al. 2004; Hennawi & Spergel 2005). At this threshold, the efficiency of cluster detection is typically $\sim 60\%$ with certain variations from different filtering methods (e.g., White et al. 2002; Hennawi & Spergel 2005; Jiao et al. 2011). This has been demonstrated observationally by analyzing the correspondences between weak-lensing peaks and clusters identified from optical/X-ray observations (e.g., Gavazzi & Soucail 2007; Miyazaki et al. 2007; Geller et al. 2010; Shan et al. 2012; Kurtz et al. 2012). The efficiency increases with the increase in the detection threshold but at the expense of detection completeness.

On the other hand, for probing cosmology with weak-lensing peak statistics, it is not necessary to individually find explicit correspondences between peaks and the underlying clusters (e.g., Marian et al. 2009). Furthermore, peaks from projection effects of LSSs also carry important cosmological information (e.g., Maturi et al. 2010; Dietrich & Hartlap 2010; Yang et al. 2011). Therefore, for cosmological studies, weak-lensing peaks themselves can be statistically analyzed directly without the need to find one-to-one links between peaks and specific clusters. Extensive investigations have been done to understand the cosmological dependence of weak-lensing peak statistics and its complementary role in cosmological studies (e.g., Marian et al. 2009; Kratochvil et al. 2010; Dietrich & Hartlap 2010; Fan et al. 2010; Yang et al. 2011; Marian et al. 2011, 2013; Liu et al. 2014). In Dietrich & Hartlap (2010), they carry out ray tracing simulations for a total of 158 cosmological models with different $(\Omega_{\rm m}, \sigma_8)$ in the flat ΛCDM framework, and analyze the dependence of the peak abundances on the two parameters.

Figure 18 shows the expected constraints on $(\Omega_{\rm m}, \sigma_8)$ from aperture mass peak abundances from Dietrich & Hartlap (2010), where the survey area is taken to be $180\,\deg^2$, and the number density and the rms of intrinsic ellipticities of source galaxies are set to be $n_{\rm g} = 25$ arcmin^{-2} and $\sigma_{\epsilon_{\rm s}} = 0.38$, respectively. The green region shows the 1σ and 2σ confidence ranges from S statistics that considers the peak S/N (ν) corresponding to different number fraction of peaks with $\nu \geq 3.25$ (see fig. 2 of Dietrich & Hartlap (2010)). The blue regions are for the corresponding constraints from M statistics that counts peaks in different redshift bins determined tomographically assuming the peaks are from individual halos (Dietrich & Hartlap 2010). The joint 1σ, 2σ and 3σ constraints of the two are shown by the regions delimited by the black contour lines. The $+$ symbol indicates the fiducial model. It is seen that the peak statistics can give rise to constraints on cosmological parameters comparable to the two-point cosmic shear correlation analyses. Including the redshift information can further improve the constraints. With the advantage of its sensitivity to non-Gaussian information, the feasibility of using weak-lensing peak statistics to probe the primordial non-Gaussianity has also been analyzed (Marian et al. 2011). It is shown that future Euclid-like surveys can constrain f_{NL} to $\Delta f_{NL} \sim 10$ (Marian et al. 2011). Beyond the abundance, further information from the peak correlation and the peak profile can provide additional values to cosmological studies (Marian et al. 2013).

While it is clear that weak-lensing peak statistics can be an important probe complementary to cosmic shear correlation analyses, their applications in deriving cosmological parameter constraints

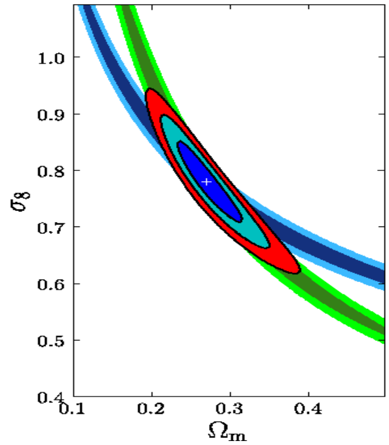

Fig. 18 Expected constraints on $(\Omega_{\rm m}, \sigma_8)$ derived from aperture mass peak abundances for a CFHTLS-like $180\,\deg^2$ survey reproduced from fig. 4 in Dietrich & Hartlap (2010). The green and blue regions show 1σ and 2σ confidence ranges from S and M statistics, respectively. The regions delimited by the black contours are the joint 1σ, 2σ and 3σ constraints from the two peak statistics. Printed with permission from the authors and by permission of Oxford University Press on behalf of The Royal Astronomical Society.

rely on accurate predictions of relevant peak statistics for different cosmological models. From large simulations, it is possible to generate a numerical library for different model predictions with densely sampled cosmological parameters. However, because of the large number of cosmological parameters and the necessity to include different physical and observational effects, e.g., baryonic effects (e.g., Yang et al. 2013a) and mask effects (e.g., Liu et al. 2014), such an approach can be computationally expensive. In addition, while simulations can give rise to results that combine all the effects, theoretical understandings of different effects on peak analyses are crucially important. Therefore, it is highly desirable to develop models for weak-lensing peak statistics, either through fitting to simulation results with important physical quantities or parameters explicitly written out in the fitting formula, or from theoretical considerations of the origin of weak-lensing peaks. The model shown in Equation (96) is an example of the latter. Unfortunately, it is too simplified to be used in real cosmological studies. By analyzing simulation results, Marian et al. (2009, 2010) find that with a proper choice of a hierarchy of matched filters recursively applied to the projected mass density field from the highest mass to the lower ones, the resulting 2D peak mass function follows very well the scaling relation of the 3D mass function with respect to different cosmological models. Therefore the cosmological dependence of the 2D peak mass function can possibly be modeled by

$$n^X = n_{\rm fit}^{\rm fiducial} \times n_{\rm ST}^X / n_{\rm ST}^{\rm fiducial},$$

where n^X is the predicted 2D peak mass function for the cosmological model X, $n_{\rm fit}^{\rm fiducial}$ is the fitted 2D peak mass function for the fiducial model derived from simulations, and $n_{\rm ST}^X$ and $n_{\rm ST}^{\rm fiducial}$ are the corresponding 3D Sheth-Tormen mass functions (Marian et al. 2010). In Hamana et al. (2004, 2012), they derive, from simulation results, a fitting formula for the abundance of weak-lensing convergence peaks that modifies Equation (96) by taking into account the bias and scatter of the peak height induced by the noise from intrinsic ellipticities of source galaxies, the non-spherical mass distribution of halos and the projection effect from LSSs.

In Fan et al. (2010), we develop a model for weak-lensing peak abundances including the noise effects modeled as a Gaussian random field. We consider halo regions and regions away from halos separately. In a particular halo region, the smoothed convergence field can be modeled as

$$K_{\mathrm{N}} = K + N\,,$$

where K is for the smoothed signal from the halo and N is the Gaussian random field from noise. Assuming a known K, e.g., following the NFW halo profile, the peak abundance of the field K_{N}, which is also a Gaussian random field, can be calculated theoretically. Compared to the pure noise case, the peak abundance is modified by the halo's mass distribution. For the highest peak corresponding to the halo, its height is altered by the existence of noise N generating both scatters and a systematic bias toward higher values. The bias depends on the density profile of the halo. This, in a certain sense, provides a theoretical explanation for the fitting result of Hamana et al. (2004, 2012). By employing the halo mass function, we can then calculate the peak abundance in halo regions. For regions outside halos, we simply calculate the peak abundance from N. The total peak abundance is the sum of the two parts (Fan et al. 2010). It is noted that in our modeling, the peaks in a halo region are counted individually. Therefore when finding peaks from weak-lensing maps, we do not combine peaks that are close together to form a single peak as some of the analyses do (Hamana et al. 2012).

In Figure 19, we show the derivatives of the peak abundance with respect to σ_8 (left panel) and Ω_{m} (right panel). Here we consider $n_{\mathrm{g}} = 30$ arcmin^{-2} and $\sigma_{\epsilon_{\mathrm{s}}} = 0.4$, and a Gaussian smoothing with $\theta_{\mathrm{G}} = 1'$. We only include the noise from intrinsic ellipticities of source galaxies in the theoretical calculation. The blue symbols and the error bars are the average values and corresponding 1σ variations computed from 64 sets of simulated maps of $3 \times 3\,\mathrm{deg}^2$ with different σ_8 and Ω_{m}. The shaded regions are the 1σ variations from one set of maps to another. It is seen that within the error ranges, our theoretical predictions (red lines) agree with the simulation results very well. The green lines using the simple model of Equation (96) without accounting for the noise effects overpredict the cosmological information in peak abundances for relatively low peaks with $\nu \leq 5$.

Figure 20 shows the peak number distributions and the expected cosmological constraints for a $3 \times 3\,\mathrm{deg}^2$ survey. From the left panel, we see that without including the effects of noise (black histograms), the number of peaks are systematically underestimated. On the other hand, our model predictions (red histograms) are in good agreement with the simulation results (blue histograms). The right panel shows the derived constraints on $(\Omega_{\mathrm{m}}, \sigma_8)$ from a survey of $3 \times 3\,\mathrm{deg}^2$ with the 'data' constructed from the simulations for the fiducial model and the theoretical predictions calculated from the model of Fan et al. (2010). In the fitting analyses, we take into account the covariance of the number of peaks between different bins. It is seen that the best fit values shown by the red symbol are consistent with the fiducial ones (blue symbol) with little bias noting the degeneracy of the two parameters indicated approximately by the dotted line. This demonstrates the applicability of our model. Details of the analyses can be found in Liu et al. (2014).

We note that the current model of Fan et al. (2010) concerns high peaks and considers the dominant shape noise from intrinsic ellipticities of source galaxies. The projection effects from LSSs contribute extra 'noise' affecting signals from individual halos. They can also generate peaks themselves. These peaks are relatively low and not dominated by single halos (e.g., Yang et al. 2011). Different from the shape noise, the projection effects themselves contain important cosmological information. In Maturi et al. (2010), they propose a theoretical model for weak-lensing peak statistics caused by the projection effects of LSSs and the shape noise of source galaxies by assuming that they can be described by a Gaussian random field. By comparing with simulations, it is shown that the model can predict well the peak counts for peaks with $\nu < 5$, and underestimate the high peaks. This is understandable because high peaks are dominantly from single halos that are highly non-Gaussian. Our model from Fan et al. (2010) combines the contribution from individual halos and the Gaussian random field from shape noise. It should be readily extended to include the projection effects in the Gaussian random field. Then all the calculations are basically the same with the only change being the inclusion of the power spectrum from the projection effects. In this approach, we can in principle

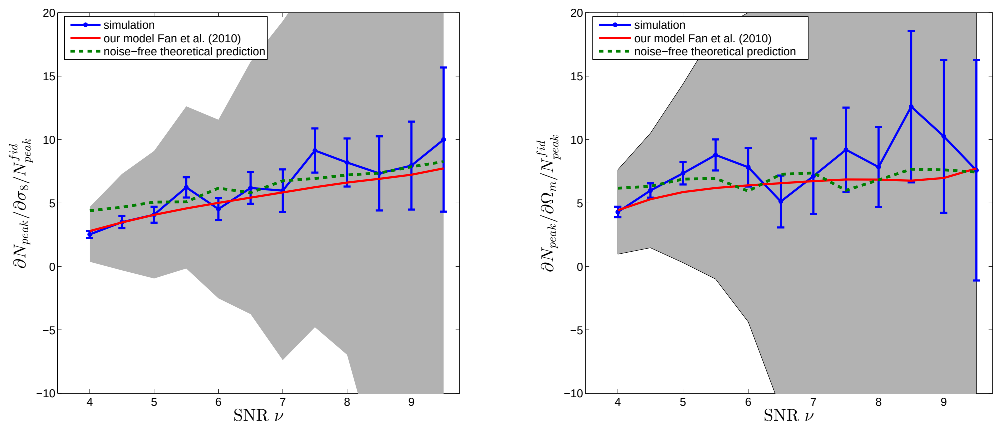

Fig. 19 Derivatives of the peak abundances with respect to σ_8 (*left*) and Ω_m (*right*) reproduced from fig. 6 in Liu et al. (2014). The blue symbols with error bars are the average results and their 1σ errors calculated from 64 sets of simulated maps with different Ω_m and σ_8, and the shaded regions show the 1σ variations from map to map ($3 \times 3\,\mathrm{deg}^2$ each). The red lines are the theoretical predictions from our model of Fan et al. (2010), and the green dashed lines are from the model of Eq. (96). Printed with permission from the authors and by permission of the AAS.

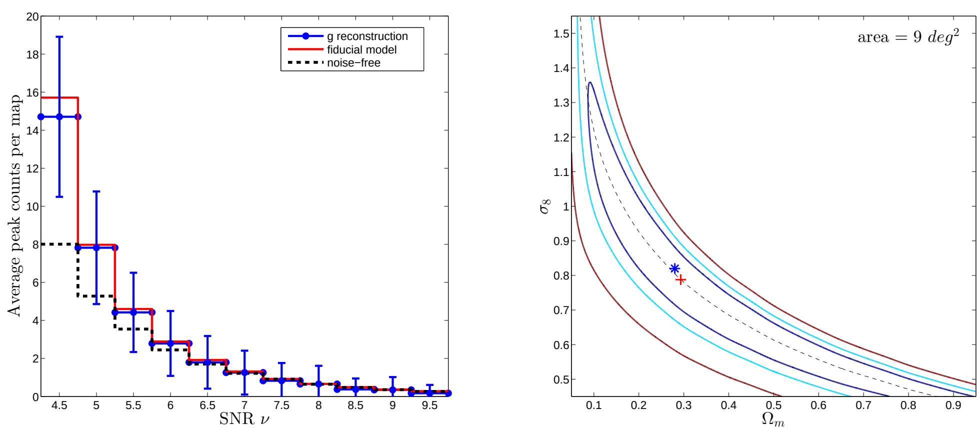

Fig. 20 Number distribution of peaks (*left*) and the expected cosmological constraints on $(\Omega_\mathrm{m}, \sigma_8)$ from a survey of $3 \times 3\,\mathrm{deg}^2$ (*right*), reproduced from fig. 7 in Liu et al. (2014). In the left panel, the results from simulations by averaging over 128 maps for the fiducial model are shown by blue histograms. The error bars indicate the 1σ variations from map to map. The red histograms are for the predictions of Fan et al. (2010), and the black histograms are for the results from Eq. (96). The right panel shows the corresponding constraints derived from the peak number distribution. The theoretical predictions are calculated from the model of Fan et al. (2010), and the data are from the simulations for the fiducial model (blue histograms in the left panel). The $(\Omega_\mathrm{m}, \sigma_8)$ of the fiducial model are shown by the blue "*" symbol. The best fit values are shown by the red "+" symbol. Printed with permission from the authors and by permission of the AAS.

model the peaks over a large range of S/N, from low to high. One important issue to be investigated carefully is the determination of the mass scale above which single halos are responsible dominantly for the corresponding peak signals. The power spectrum describing the large-scale projection effects should then exclude the contributions from those massive halos.

Observationally, current weak-lensing peak analyses are still limited by relatively large statistical errors because of limited survey areas (e.g., Shan et al. 2012; Hamana et al. 2012). However, its feasibility for cosmological studies has begun to emerge. For example, by analyzing the $64\,\mathrm{deg}^2$ of the CFHTLS W1 field, Shan et al. (2012) detect ~ 1000 peaks with S/N $\nu > 3$. Future weak-lensing surveys covering $\sim 5000{-}20\,000\,\mathrm{deg}^2$ survey areas will be able to give rise to, on the order of, $\sim 100\,000$ peaks for cosmological analyses. With much reduced statistical errors, precision cosmological studies ask for thorough understandings of different systematic effects. The accurate modeling of peak statistics either theoretically or from simulation libraries is critical. It is worth noting that with a theoretical model explicitly including the density profile of dark matter halos, such as the model of Fan et al. (2010), future weak-lensing peak analyses from large surveys can in principle allow us to constrain the halo density profile simultaneously with other cosmological parameters. This, on the one hand, can return to us more physical information about the formation and evolution of halos, and on the other hand, can also reduce the potential bias in cosmological parameter constraints arising from the incorrect pre-assumption about the density profile of dark matter halos.

4.4 Galaxy-galaxy Lensing

Galaxy-galaxy (g-g) lensing is named for analyzing weak-lensing signals of background galaxies around a selected sample of foreground lens galaxies (e.g., Miralda-Escude 1996; Squires & Kaiser 1996; Guzik & Seljak 2001). By stacking the signals over the foreground galaxies in the sample, g-g lensing analyses can statistically probe the mass distribution down to galactic scales, though not individually (e.g., Tyson et al. 1984; Brainerd et al. 1996; Kovner & Milgrom 1987; Schneider & Rix 1997; Hudson et al. 1998; Hoekstra et al. 2003; Mandelbaum et al. 2006, 2008; Pastor Mira et al. 2011; Li et al. 2013; Gillis et al. 2013; Hudson et al. 2013; Brimioulle et al. 2013). Furthermore, g-g lensing provides us a unique way to study the correlation between the properties of galaxies and those of their dark matter halos, and therefore to test the theory of galaxy formation (e.g., Hoekstra et al. 2002; Fan 2003; Mandelbaum et al. 2005; Li et al. 2009b; Reyes et al. 2012; Miyatake et al. 2013; Velander et al. 2014). In cosmological studies, g-g lensing measurements can also be helpful in breaking the degeneracy between the bias factor of the galaxy distribution with respect to that of the dark matter and the amplitude of dark matter density perturbations involved in galaxy clustering analyses. Therefore the combination of g-g lensing and galaxy clustering analyses can give rise to better cosmological constraints than that using galaxy clustering alone (e.g., Seljak et al. 2005; Yoo et al. 2006; Baldauf et al. 2010; Mandelbaum et al. 2013; van den Bosch et al. 2013; More et al. 2013; Cacciato et al. 2013).

For g-g lensing, it analyzes shear signals around foreground lens galaxies. The mean tangential shear $\langle\gamma_{\mathrm{t}}\rangle(R)$ along the boundary of a circular aperture of radius R around a lens galaxy is linked to the mean convergence $\bar{\kappa}(<R)$ inside the aperture by (e.g., Miralda-Escude 1996; Squires & Kaiser 1996)

$$\langle\gamma_{\mathrm{t}}\rangle(R) = -\frac{1}{2}\frac{d\bar{\kappa}(<R)}{d\ln R} = \bar{\kappa}(<R) - \bar{\kappa}(R), \tag{97}$$

where $\bar{\kappa}(R)$ is the mean κ at R. For a single lens galaxy, its weak-lensing signals are hardly detectable from background galaxies noting their much larger intrinsic ellipticities. We thus need to stack the signals over a sample of foreground lens galaxies. This effectively increases the number density of source galaxies to $n_{\mathrm{g}}N_{\mathrm{lens}}$ and, consequently, enhances the S/N by $\sqrt{N_{\mathrm{lens}}}$ times compared to that from a single lens galaxy, where N_{lens} is the number of lens galaxies to be stacked and n_{g} is the surface number density of background galaxies. Therefore, statistically, g-g lensing probes the matter-galaxy cross correlation with the contribution from uncorrelated structures along lines of sight being averaged out. Specifically, on average, in comoving coordinates we can write $\bar{\kappa}(R)$ around foreground galaxies at a known redshift $z_{\rm l}$ with background galaxies at $z_{\rm s}$ as (e.g., Guzik & Seljak 2001)

$$\bar{\kappa}(R) = \int \frac{\rho_{\rm m}}{\tilde{\Sigma}_{\rm cr}(\chi, \chi_{\rm s})} \Big[1 + \xi_{\rm g,dm}(r)\Big] d\chi, \tag{98}$$

where $\xi_{\rm g,dm}$ is the 3D matter-galaxy cross correlation, $r = r(R, \chi_{\rm l}, \chi)$ and R are the 3D comoving distance and the 2D projected comoving distance to the lens galaxy, respectively, and $\chi_{\rm l}$, χ and $\chi_{\rm s}$ are the radial comoving distances to the lens galaxy, to the matter that contributes to the lensing signal and to the background source galaxies, respectively. The quantity $\tilde{\Sigma}_{\rm cr}$ is the lensing critical density in comoving coordinates with

$$\tilde{\Sigma}_{\rm cr} = a(\chi) f_{\rm K}(\chi_{\rm s}) / \Big[4\pi G f_{\rm K}(\chi) f_{\rm K}(\chi_{\rm s} - \chi)\Big]$$

and $\rho_{\rm m}$ is the comoving matter density of the Universe. Thus $\tilde{\Sigma}_{\rm cr}^{-1}$ reflects the lensing efficiency for the matter distribution at χ. Given the typical correlation scale of $\xi_{\rm g,dm}$, the dominant contribution to the lensing signals is from the matter distribution closely around lens galaxies. Thus at given $z_{\rm l}$, $\tilde{\Sigma}_{\rm cr}$ can be moved out of the integration in Equation (98). We then have approximately

$$\tilde{\Sigma}_{\rm cr} \langle \gamma_{\rm t} \rangle (R) = \bar{\Sigma}(< R) - \bar{\Sigma}(R) = \Delta\Sigma(R)\,, \tag{99}$$

where

$$\bar{\Sigma}(R) = \int \rho_{\rm m} \Big[1 + \xi_{\rm g,dm}(r)\Big] d\chi\,. \tag{100}$$

Thus g-g lensing leads to an estimate of the excess surface mass density (ESD) $\Delta\Sigma(R)$. Note that the inclusion of the constant term 1 in the square bracket in Equation (98) is for relating $\bar{\kappa}$ to $\bar{\Sigma}(R)/\tilde{\Sigma}_{\rm cr}$, and it is canceled out in $\Delta\Sigma(R)$.

For observations with known redshift information for individual source and lens galaxies, we can calculate $\tilde{\Sigma}_{\rm cr}$ for each source-lens pair, and the average quantity $\langle \tilde{\Sigma}_{\rm cr} \gamma_{\rm t}(R) \rangle$ over all the pairs gives rise to a measure of ESD averaged over the lens sample. In the case of known redshifts for lens galaxies but not for individual source galaxies, we can get the effective $\tilde{\Sigma}_{\rm cr}^{z_{\rm l}}$ and the average $\gamma_{\rm t}(R)^{z_{\rm l}}$ at each $z_{\rm l}$ by averaging over $z_{\rm s}$ with the source redshift distribution of $p_{\rm s}(z_{\rm s})$. Then the mean ESD over the lens sample can be obtained by averaging $\tilde{\Sigma}_{\rm cr}^{z_{\rm l}} \gamma_{\rm t}(R)^{z_{\rm l}}$ over the lens galaxies. If the individual redshifts for lens galaxies are also unknown and their redshift distribution is wide, the direct measure of $\langle \gamma_{\rm t} \rangle(\theta)$ leads to $\bar{\kappa}(< \theta) - \bar{\kappa}(\theta)$ where $\theta = R(\chi_{\rm l})/f_{\rm K}(\chi_{\rm l})$ is the projected angular distance to the lens galaxy, and (e.g., Guzik & Seljak 2001)

$$\begin{aligned} \bar{\kappa}(\theta) \;&=\; 6\pi^2 \left(\frac{H_0}{c}\right)^2 \Omega_{\rm m} \int_0^{\chi_{\rm H}} d\chi \, p_{\rm lens}(\chi) \frac{W(\chi)}{a(\chi)} \\ &\quad \times \int k \, dk \, P_{\rm g,dm}(k, \chi) \frac{2 J_1[k f_{\rm K}(\chi)\theta]}{k f_{\rm K}(\chi)\theta}\,, \end{aligned} \tag{101}$$

and

$$\begin{aligned} \langle \gamma_{\rm t} \rangle(\theta) \;&=\; \bar{\kappa}(< \theta) - \bar{\kappa}(\theta) \\ &=\; 6\pi^2 \left(\frac{H_0}{c}\right)^2 \Omega_{\rm m} \int_0^{\chi_{\rm H}} d\chi \, p_{\rm lens}(\chi) \frac{W(\chi)}{a(\chi)} \\ &\quad \times \int k \, dk \, P_{\rm g,dm}(k, \chi) \frac{2 J_2[k f_{\rm K}(\chi)\theta]}{k f_{\rm K}(\chi)\theta}\,, \end{aligned} \tag{102}$$

where $P_{\rm g,dm}(k,\chi)$ is the matter-galaxy cross-power spectrum, $p_{\rm lens}(\chi)$ is for the lens distribution,

$$W(\chi) = f_{\rm K}(\chi)\int_{\chi}^{\chi_{\rm H}} p_{\rm s}(\chi')\Big[f_{\rm K}(\chi'-\chi)/f_{\rm K}(\chi')\Big]d\chi'\,,$$

and J_1 and J_2 are the Bessel functions.

Figure 21 presents the ESD $\Delta\Sigma$ from g-g lensing analyses of Mandelbaum et al. (2006) with SDSS (left) and Velander et al. (2014) with CFHTLenS (right). The lens galaxies are divided into different luminosity bins. In each bin, the lensing signals around early-type (red in the left panels and dark purple in the right panels) and late-type (blue in the left and green in the right) galaxies are analyzed separately. Both measurements clearly show that the ESD increases with the luminosity, and statistically, late-type galaxies reside in halos less massive than those hosting early-type galaxies. The lines in each panel are the fitting results using the halo model (Mandelbaum et al. 2006; Velander et al. 2014). Note that the considered scale covers the range from ~ 10 kpc to ~ 10 Mpc, i.e., from galactic scales to cluster scales and even beyond. Thus, besides the halos directly hosting the lens galaxies, the ESD shown in Figure 21 also reflects the environment of the lens galaxies. For galaxies in a given luminosity bin, some are central galaxies in clusters, and some are satellite galaxies. The halo mass distributions of the central and the satellite galaxies are different. Therefore in the theoretical modeling of g-g lensing, they should be considered differently (e.g., Seljak et al. 2005; Mandelbaum et al. 2005, 2006; van Uitert et al. 2011; Cacciato et al. 2014; Velander et al. 2014). The halo model fitting shown in Figure 21 takes into account the differences of the two classes of lens galaxies (Mandelbaum et al. 2006; Velander et al. 2014). For the CFHTLenS analyses, because the measurements extend to large scales, the two-halo terms are also included in the modeling. In addition, the baryonic matter contribution from the mean stellar mass of lens galaxies is also put in by modeling it as a point source (Velander et al. 2014). By employing the halo model, g-g lensing observations can then set constraints on the relevant parameters, such as the luminosity-mass relation for central galaxies, the fractional contribution of satellite galaxies for a given luminosity bin, etc.

Figure 22 shows the constraints on the luminosity-mass (left) and stellar mass-halo mass (right) relations derived from different g-g observations (Velander et al. 2014). Given the somewhat different classifications of different types of lens galaxies and theoretical modeling, the results from different observations are in broad agreement with each other. For the satellite fraction, it is found that for early-type/red galaxies, it is about 0.5 for lens galaxies with luminosity $L_{\rm r} \sim 10^{10}L_{\odot}$, and decreases for brighter lens galaxies. On the other hand, for late-type/blue galaxies, the fraction is low for all the luminosity bins, indicating that they are mostly isolated galaxies (Mandelbaum et al. 2006; Velander et al. 2014).

While the g-g lensing alone can provide valuable information, more can be learned by combining with galaxy clustering analyses. In Li et al. (2009b), we use the group catalog constructed from SDSS DR4 by Yang et al. (2007) to model the g-g lensing signals. With the group catalog, the information about central and satellite galaxies is known, and therefore we do not need to involve the free parameter(s) for satellite fractions in different bins. With the ranking method, the mass of parent halos for groups and the mass of subhalos for satellite galaxies at the time of their accretion into parent halos can be assigned (Yang et al. 2007; Giocoli et al. 2008; Li et al. 2009b). Taking into account the tidal disruption of subhalos afterwards in the merging process, we can then model the g-g lensing signals assuming known density profiles for parent and subhalos, respectively. We note that for different cosmological models, the mass assignment can be different, and thus different lensing signals can be expected. In comparison with observational results, g-g lensing analyses in combination with galaxy clustering information can thus set constraints on cosmological parameters.

We show the cosmology dependence of the lensing signals from Li et al. (2009b) in Figure 23. The symbols with error bars are the results of Mandelbaum et al. (2006) using SDSS. The solid and dotted lines are the predictions of WMAP3 (Spergel et al. 2007) and WMAP1 (Spergel et al. 2003) cosmological models, respectively. The differences of the results from the two cosmological

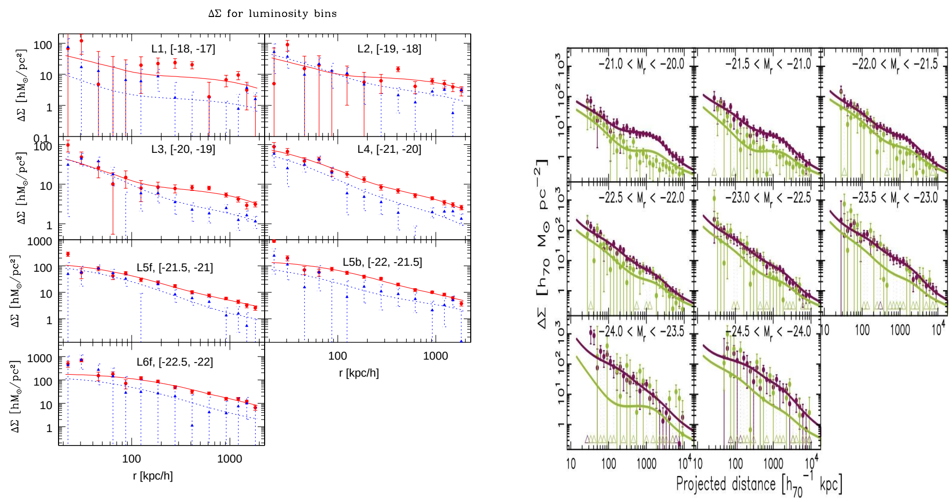

Fig. 21 Galaxy-galaxy lensing measurements from SDSS reproduced from fig. 2 in Mandelbaum et al. (2006) (*left*) and from CFHTLenS reproduced from fig. 5 in Velander et al. (2014) (*right*), respectively. Different panels show the results of ESD for lens galaxies in different luminosity bins as specified therein. In the left (*right*) panels, the red (*dark purple*) and blue (*green*) symbols with error bars are the observational results for early and late-type lens galaxies, respectively. The corresponding lines are for the fitting results of the halo model. Printed with permission from the authors and by permission of Oxford University Press on behalf of The Royal Astronomical Society.

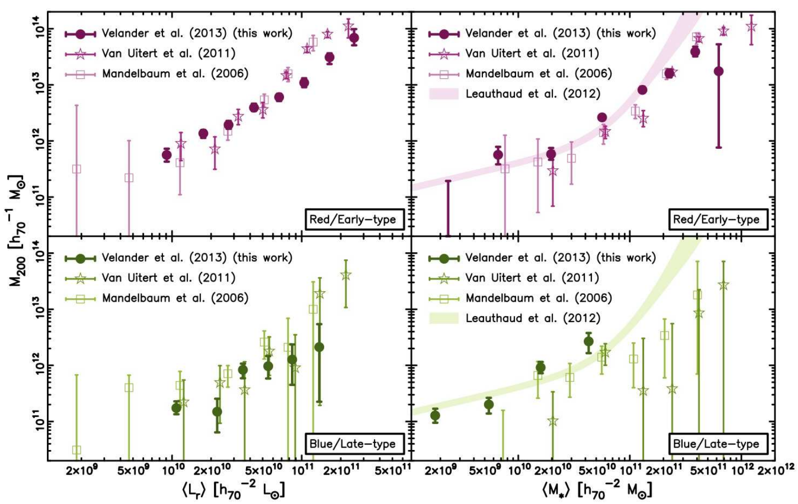

Fig. 22 Constraints on the luminosity-mass (*left*) and stellar mass-halo mass (*right*) relation for central galaxies derived from galaxy-galaxy lensing analyses, reproduced from fig. 12 in Velander et al. (2014). The results from Velander et al. (2014) using CFHTLenS, van Uitert et al. (2011) using RCS2 and Mandelbaum et al. (2006) using SDSS are shown for the luminosity-mass relation in the left panels. In the right panels, an additional result from Leauthaud et al. (2012) using COSMOS is also shown. Note that the COSMOS result is the same in the upper and lower right panels with no distinctions between red and blue lens galaxies. Printed with permission from the authors and by permission of Oxford University Press on behalf of The Royal Astronomical Society.

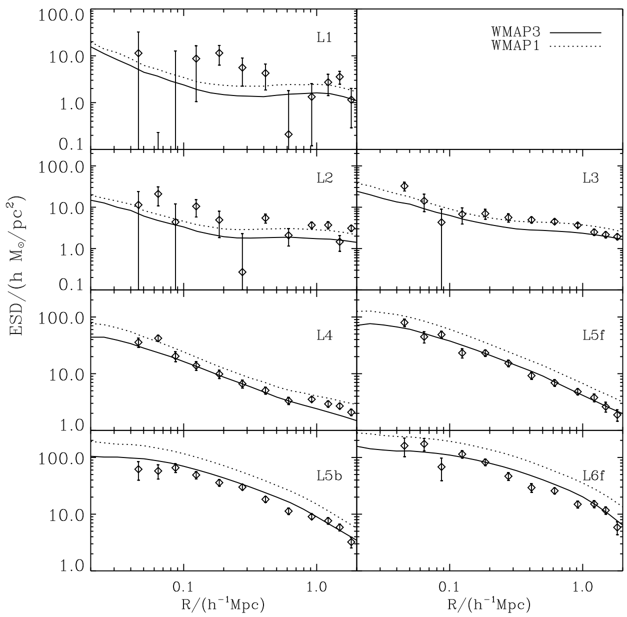

Fig. 23 Galaxy-galaxy lensing results reproduced from fig. 8 in Li et al. (2009b). The symbols with error bars are the observational results of Mandelbaum et al. (2006) for different luminosity bins using SDSS. The solid lines are the theoretical results predicted from Li et al. (2009b) based on the group catalog of Yang et al. (2007) using cosmological parameters consistent with those from WMAP3. The dotted lines are the theoretical results for the WMAP1 cosmological model. Printed with permission from the authors and by permission of Oxford University Press on behalf of The Royal Astronomical Society.

models are clearly seen. The observational results agree better with the WMAP3 cosmology for high luminosity bins. For low luminosity bins, WMAP1 seems to fit the observations better. It is noted that the most up-to-date observations show $\sigma_8 \approx 0.83$ for flat ΛCDM, in between that from WMAP1 with $\sigma_8 \approx 0.9$ and that from WMAP3 with $\sigma_8 \approx 0.75$ (e.g., Planck Collaboration et al. 2013a).

With galaxy group catalogs, we can also measure the g-g lensing effects around selected satellite galaxies and therefore to directly probe the properties of their subhalos (e.g., Li et al. 2013). The application of such analyses to the CFHT/MegaCam Stripe-82 Survey has resulted in the first clear detection of g-g lensing signals around satellite galaxies (Li et al. 2014). The left plot of Figure 24 shows the measured g-g lensing signals around satellite galaxies in parent halos with assigned mass in the range $10^{13}\ h^{-1}\ M_\odot \leq M \leq 5 \times 10^{14}\ h^{-1}\ M_\odot$. The location r_p of the satellites to the center of their parent halos is shown in each panel. In the left panels of this plot, the black solid lines are the fiducial model predictions, and the green and red lines are the predictions taking into account the center offsets using two different models. The solid black lines in the right panels of this plot are the results from the best fit model to the data. The right plot shows the derived constraints on the host halo mass M, the distance r_p and subhalo mass $M_{\rm sub}$ using data shown in the upper panels of the left plot (Li et al. 2014). It is seen that current data can already give rise to reasonable constraints on these quantities. Future LSST-like surveys can detect subhalo lensing signals with much higher S/N and therefore can potentially constrain the properties of subhalos much better (Li et al. 2014).

Recently, by combining the g-g lensing and the two-point autocorrelation function of galaxies from SDSS DR7, Mandelbaum et al. (2013) demonstrate the feasibility and the added value of using

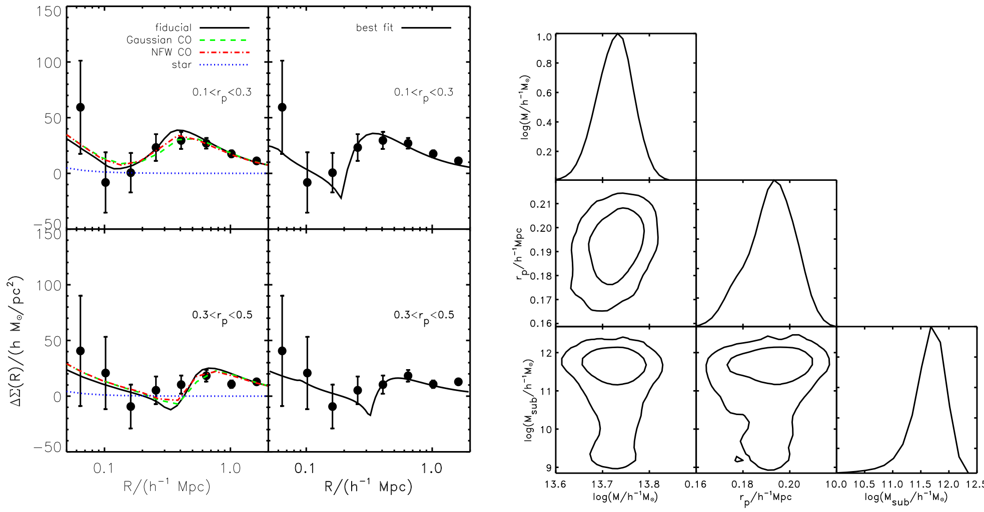

Fig. 24 Galaxy-galaxy lensing signals around satellite galaxies measured from the CFHT/MegaCam Stripe-82 Survey (*left*) and the constraints derived from the data shown in the upper right panel of the left plot (*right*), reproduced from figure 1 and figure 4, respectively, in Li et al. (2014), with permission from the authors and by permission of Oxford University Press on behalf of The Royal Astronomical Society.

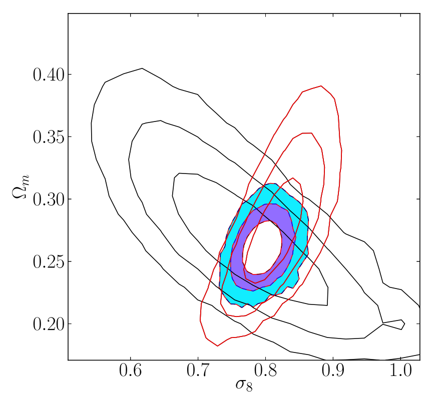

Fig. 25 $(\sigma_8, \Omega_\mathrm{m})$ constraints for flat ΛCDM, reproduced from fig. 14 in Mandelbaum et al. (2013). The black contours are from the joint analyses of galaxy-galaxy lensing and the galaxy autocorrelation using SDSS DR7. The red contours are from WMAP7. The filled contours are the combined results of the two. Printed with permission from the authors and by permission of Oxford University Press on behalf of The Royal Astronomical Society.

g-g lensing analyses in constraining cosmological parameters. By suitably eliminating small scale g-g lensing and galaxy autocorrelation signals, complications from the detailed galaxy distribution within dark matter halos and the effects of baryonic physics can be controlled. Then by assuming that the galaxy distribution is solely determined by the matter distribution, the galaxy number density field can be written as the Taylor expansion of the matter density field. Therefore the g-g lensing signals that are related to $\rho_\mathrm{m}\xi_\mathrm{gm}$ and the autocorrelation function of galaxies ξ_gg can be calculated in terms of the linear bias factor and quadratic bias factor, and the nonlinear matter power spectrum times the matter density of the Universe (Baldauf et al. 2010; Mandelbaum et al. 2013). The joint observational analyses of the g-g lensing and the galaxy autocorrelation can thus constrain the galaxy bias and the matter power spectrum separately to break their degeneracy which exists in the galaxy autocorrelation. This in turn leads to better constraints on the cosmological parameters. Figure 25 shows the constraining result for $(\sigma_8, \Omega_{\rm m})$ in flat ΛCDM from Mandelbaum et al. (2013), where the black contours are from the joint analyses of g-g lensing and the galaxy autocorrelation using SDSS DR7, the red contours are from WMAP7 data, and the filled contours are the combined result of the two. The different directions of the black and red contours demonstrate the great value of including the g-g lensing data in the analyses. Similar studies have been done by Cacciato et al. (2013) who include the small scale information in the analyses by using the conditional luminosity function (CLF) to populate galaxies in dark matter halos (van den Bosch et al. 2013; More et al. 2013). They show that in principle, the cosmological parameters and the halo-galaxy connection through the CLF can be constrained simultaneously.

Beyond the two-point g-g lensing analyses, higher order studies carry additional cosmological information. Using CFHTLenS data, Simon et al. (2013) recently report the first measurements of galaxy-galaxy-galaxy lensing signals of $\langle N_{\rm g}^2 M_{\rm ap}\rangle$ and $\langle N_{\rm g} M_{\rm ap}^2\rangle$ with high significance, where $\langle N_{\rm g}^2 M_{\rm ap}\rangle$ is related to lensing signals around lens galaxy pairs and $\langle N_{\rm g} M_{\rm ap}^2\rangle$ represents excess shear correlations around lens galaxies. Such studies can be used to probe the bispectrum of the matter-galaxy connection for further understanding the formation and evolution of different types of galaxies (Simon et al. 2013).

5 DISCUSSION

For large-scale cosmic shear studies, current Stage II weak-lensing observations have reached ~ 150 deg^2 with $n_{\rm g} \sim 15$ arcmin^{-2} (e.g., Erben et al. 2013). Careful data analyses have demonstrated the cosmological applicability of the weak-lensing effect (e.g., Heymans et al. 2012; Kilbinger et al. 2013). For g-g lensing analyses, shallow but wide surveys, such as SDSS, have also yielded fruitful results (Mandelbaum et al. 2013). For individual cluster studies, analyses have been done for about ~ 100 clusters resulting in constraints on the mass and density profile of associated dark matter halos, and providing mass calibrations for other observables, such as X-ray, SZ and optical richness (Okabe et al. 2013). Stage III projects represented by the Dark Energy Survey (The Dark Energy Survey Collaboration 2005) and the Hyper Suprime Cam survey (HSC Design Review 2009) are beginning to be functional. The scale of such surveys will reach a few thousand square degrees with depth similar to if not deeper than that of CFHTLenS. Therefore the data expected from these surveys will be about 1.5 order of magnitude more than the available data sets to date, which will considerably increase our knowledge about the dark matter distribution in the Universe, from galactic scales to superclusters of galaxies. This in turn will advance our understanding about the physical properties of dark matter, and the formation and evolution of galaxies presumably formed inside dark matter halos (e.g, van den Bosch et al. 2013; Kang et al. 2013). The derived cosmological parameter constraints together with other cosmological probes can be tightened, reaching $\sim 1\%$ level of precision for σ_8 and improving the Figure of Merit of (w_0, w_a) for dark energy by a factor of $2-5$ depending on the control of systematics (e.g., Weinberg et al. 2013b,a; Albrecht et al. 2006). Stage IV weak-lensing observations, expected to be in operation around or after 2020, include notably the ground-based Large Synoptic Survey Telescope (LSST) (LSST Science Collaboration et al. 2009; LSST Dark Energy Science Collaboration 2012), and the space missions of Euclid (Laureijs et al. 2011; Amendola et al. 2013; Amiaux et al. 2012) and WFIRST (Spergel et al. 2013). With six optical filters, LSST will cover a survey area of $\sim 20\,000$ deg^2. The surface number density of source galaxies $n_{\rm g}$ usable for weak-lensing analyses is expected to be close to $30-40$ arcmin^{-2}. Euclid will have a very broad band filter in optical for weak-lensing shape measurements, and three near infrared filters

Y, J, H for photometric redshift estimates. The planned survey area is $\sim 15\,000$ deg^2, and $n_{\rm g} \sim 20$ arcmin^{-2}. Thus we expect that both LSST and Euclid can obtain images for a few billion galaxies for weak-lensing analyses. Mainly operating in infrared bands, WFIRST weak-lensing observations target ~ 2000 deg^2 with $n_{\rm g} \sim 70$ arcmin^{-2}, reaching higher redshift than that of LSST and Euclid. Thus WFIRST will be greatly important in probing the growth of LSSs, and therefore the law of gravity. The Stage IV surveys aim at ambitious goals to study the nature of dark energy, gravity and dark matter. Taking the equation of state of dark energy as an example, we show in Figure 26 the current constraints on (w_0, w_a) from Xia et al. (2013) using the most up-to-date observational data. It is seen that the cosmological constant with $(w_0, w_a) = (-1, 0)$ is consistent with the data at the level of $1\sigma - 2\sigma$. The allowed range for dynamical dark energy is still rather large. In other words, current data cannot clearly reveal if the dark energy is in the form of a cosmological constant or is dynamical in nature. Stage IV observations are designed to reach the level of constraints for $\Delta w_0 \sim 0.01$ and $\Delta w_a \sim 0.1$. Then the best fit dynamical model obtained by the current data can be distinguished well from the cosmological constant at a high significance level, and thus the fundamental question regarding the nature of dark energy can be expected to be answered decisively.

However, the full realization of their statistical power for future large surveys crucially depends on our understandings about different systematic effects. For weak-lensing studies, the principal systematics from the observational side are the errors in galaxy shape measurements and those in the estimations of photometric redshifts, critical for tomographic analyses (e.g., Weinberg et al. 2013b). The weak-lensing induced shape distortion is typically on the order of 1% in cosmic shear regimes and can be larger in cluster regions. But even for cluster induced signals, they are still much smaller than the intrinsic ellipticities of galaxies with $\sigma_{\epsilon_{\rm s}} \sim 0.2-0.4$. Furthermore, as discussed in Section 3, the observed images experience the influences of telescope optics and atmospheric disturbances for ground based observations. Such PSF effects must be carefully modeled in order to obtain accurate weak-lensing signals for high precision cosmological studies.

Extensive studies have been done to discuss the tolerance level of the systematic errors in shape measurements, focusing on cosmic shear two-point correlation (power spectrum) analyses (e.g., Amara & Réfrégier 2008; Chang et al. 2013; Massey et al. 2013).

Figure 27 shows the bias on the dark energy equation-of-state parameter w induced by the additive (left) and multiplicative (right) errors in shape measurements (Massey et al. 2013). Here the baseline Stage IV survey is $15\,000\,\deg^2$ with $n_{\rm g} = 30\,$arcmin^{-2} and a median redshift of 1. The source galaxies are split into 10 redshift bins in the tomographic weak-lensing power spectrum analyses. The effects of the errors on shear measurements are written in the form of $\hat{\gamma} = (1 + m)\gamma + c$ where $\hat{\gamma}$ and γ are the measured and the true shear signals, respectively, and m and c represent the multiplicative and additive errors, respectively. Correspondingly, the measured cross-power spectrum between redshift bins at $z_{\rm A}$ and $z_{\rm B}$ is written as

$$\hat{C}(l, z_{\rm A}, z_{\rm B}) = \Big[1 + M(l, z_{\rm A}, z_{\rm B})\Big] C(l, z_{\rm A}, z_{\rm B}) + A(l, z_{\rm A}, z_{\rm B})\,.$$

The quantities $\bar{A}$ and $\bar{M}$ in the plots are defined, respectively, by

$$\bar{A} = \Big[\sum_{z_{\rm bins}} (1/2\pi) \int_{l_{\rm min}}^{l_{\rm max}} |A(l, z_{\rm A}, z_{\rm B})| l^2 d\ln l\Big] / N_{\rm A}\,,$$

$$\bar{M} = \Big[\sum_{z_{\rm bins}} (1/2\pi) \int_{l_{\rm min}}^{l_{\rm max}} |M(l, z_{\rm A}, z_{\rm B})| l^2 d\ln l\Big] / N_{\rm M}\,,$$

with

$$N_{\rm A} = N_{\rm M} = \Big[\sum_{z_{\rm bins}} (1/2\pi) \int_{l_{\rm min}}^{l_{\rm max}} l^2 d\ln l\Big]$$

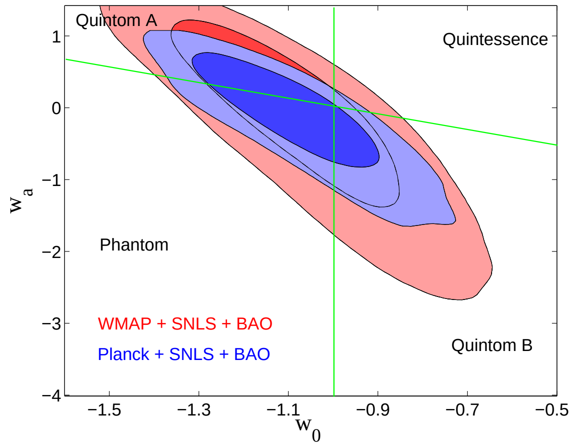

Fig. 26 The current constraints on (w_0, w_a), reprinted with permission from fig. 4 in Xia et al. (2013). Copyright(2013) by the American Physical Society.

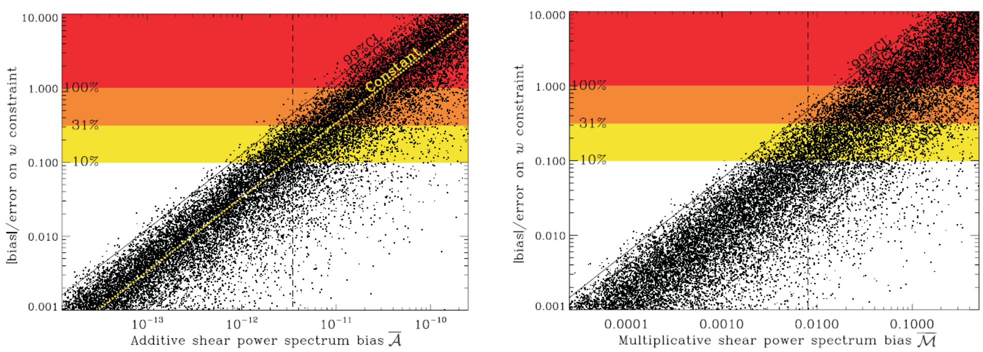

Fig. 27 Bias on w, the equation-of-state parameter of dark energy, induced by the additive (*left*) and multiplicative (*right*) errors for shape measurements, reproduced from fig. 3 in Massey et al. (2013). Each black point shows the result for a random realization of systematics with a unique dependence on angular scale and redshift. The dotted lines show the results with constant shear measurement systematics. The solid lines show limiting values including 95% and 99% of random realizations. Printed with permission from the authors and by permission of Oxford University Press on behalf of The Royal Astronomical Society.

(Massey et al. 2013). It is seen that in order to control the bias to be less than 0.31σ with σ being the statistical error, we require $\bar{A} \leq 3.5 \times 10^{-12}$ if $M = 0$ and $\bar{M} \leq 8.0 \times 10^{-3}$ if $A = 0$. Considering the coexistence of A and M, the requirements for $\bar{A}$ and $\bar{M}$ should be tighter by a factor of two or so (Massey et al. 2013).

The accuracy of the galaxy shape measurements depends on the PSF modeling, corrections for other non-convolutive errors, and image processing algorithms. Tremendous efforts have been made to evaluate the performances of different shape measurement methods. A number of challenging programs have been conducted based on simulated data with increasing complications that resemble real observations, including the STEP (Heymans et al. 2006; Massey et al. 2007), GREAT08 Challenge (Bridle et al. 2009, 2010), GREAT10 Challenge (Kitching et al. 2011, 2012, 2013) and the current ongoing GREAT3 Challenge (Mandelbaum et al. 2014). Studies specific to different surveys have also been carried out (e.g., Chang et al. 2013). The general conclusion from these investigations is that the accuracies achieved by the best shape measurement algorithms currently available are not fully sufficient for the realization of the statistical power for Stage IV surveys, although they are not pessimistically far from the requirements (e.g., Kitching et al. 2012; Chang et al. 2013; Massey et al. 2013). Further careful studies are intensively ongoing, and it is believed that by the time or even before the Stage IV projects are in place, systematic errors in shape measurements can be controlled well and they should not be major obstacles for high precision weak-lensing cosmological studies (e.g., Massey et al. 2013; Mandelbaum et al. 2014, and references therein).

Because lensing effects are sensitive to positions of background galaxies, another important source of errors for precision weak-lensing studies comes from uncertainties in the redshift information for faint source galaxies. In particular, tomographic weak-lensing analyses by dividing source galaxies into multiple redshift bins can significantly boost the amount of cosmological information compared to 2D analyses, and have become one of the key parts of weak-lensing studies for future surveys (e.g., Hu 1999; Schrabback et al. 2010; Benjamin et al. 2013). For that, we need to measure the redshift for every single source galaxy. Obtaining accurate spectroscopic redshifts for individual galaxies is infeasible even for the current generation of weak-lensing surveys involving a few million source galaxies, needless to say for future Stage III and Stage IV surveys targeting hundreds of millions to a few billion galaxies with mean redshift close to $z \sim 1$ or higher. Therefore photometric redshift (photo-z) determinations from multi-filter photometry become a necessary part of weak-lensing surveys. Photo-z measurements rely on the characteristic SED features of galaxies. Their precisions depend on the observed wavelength coverage, filter sets, photometric accuracy, our understanding about the physical properties of galaxies in the sample and so on (e.g., Abdalla et al. 2008; Ilbert et al. 2009; Hildebrandt et al. 2012). Different algorithms have been developed for photo-z determination, either based on template fitting or on sets of training data with known spectroscopic redshifts (e.g., Hildebrandt et al. 2010; Abdalla et al. 2011; Dahlen et al. 2013). The specific choice of the templates and training data can also introduce errors to the determination of photo-z if they are not representative for the considered galaxy samples (e.g., Abrahamse et al. 2011).

Because the errors in photo-z determinations are inevitable, their impacts on weak-lensing cosmological studies are then among the issues in the field that are of most concern. The systematic bias of photo-z $z_{\rm p}$ with respect to the true redshift $z_{\rm spec}$, the scatter of $(z_{\rm p} - z_{\rm spec})$, and the fraction of outliers with large $|z_{\rm p} - z_{\rm spec}|$, or more completely, the distribution of $(z_{\rm p} - z_{\rm spec})$, depend on measurements of photo-z. If we precisely know the bias and the outlier fraction, they can in principle be included in the modeling and thus be potentially correctable. The scatters contribute to statistical errors in cosmological parameter constraints, and such errors increase relatively mildly with the increase of scatters in photo-z (e.g., Ma et al. 2006; Zhan 2006; Newman et al. 2013). More seriously, the uncertainties in the bias, the scatter and the outlier fraction, namely errors on errors, can significantly degrade constraints on the cosmological parameters. Studies show that in order to limit the degradation of constraints on the dark energy parameters to be less than 1.5, these uncertainties need to be known to a precision better than $\sim 10^{-3}$ (e.g., Ma et al. 2006; Ma & Bernstein 2008; Sun et al. 2009; Bernstein & Huterer 2010; Hearin et al. 2010). This requires high-quality calibrations of photo-z. Direct calibrations using spectroscopically determined redshifts demand an order of 10^5 for spectroscopic redshifts spanning the redshift range of the considered photometric sample (e.g., Ma & Bernstein 2008; Hearin et al. 2010). The sample variance of the spectroscopic data can introduce additional effects on calibration of photo-z and needs to be carefully taken into account when designing spectroscopic follow-up surveys (e.g., Cunha et al. 2012). Involving cross-correlation techniques through galaxy clustering can provide self-calibrations for photo-z and thus mitigate the stringent requirements for spectroscopic redshift measurements (e.g., Zhan 2006; Newman 2008; Zhang et al. 2010; Newman et al. 2013; Rhodes et al. 2013, and references therein).

Apart from observational uncertainties, different astrophysical effects can also impact weak-lensing cosmological studies. Accurate understanding and modeling of the nonlinear evolution of LSSs and baryonic effects are highly desired for extending the analyses to small scales where weak-lensing effects are significant (e.g., Zhan & Knox 2004; Huterer & Takada 2005; Jing et al. 2006; Kitching & Taylor 2011; Takahashi et al. 2012; Hearin et al. 2012; Yang et al. 2013a; Zentner et al. 2013; Semboloni et al. 2013). The intrinsic alignments of galaxies, arising from either the physical connection of close pairs of galaxies or the lensing effects of foreground halos on background galaxies, can considerably contaminate the cosmic shear correlation analyses (e.g., Hirata et al. 2007; Joachimi et al. 2013; Heymans et al. 2013). On the other hand, these effects themselves carry important information about the astrophysical processes related to galaxy formation. With a proper understanding and modeling for their characteristic behaviors, the intrinsic alignments of galaxies can potentially be separated from weak-lensing effects, and thus their systematic effects on cosmological parameter determinations can be significantly reduced. Moreover, such an approach can also provide constraints on the intrinsic alignments, and therefore probe the galaxy formation simultaneously from weak-lensing observations, though at a cost of somewhat losing statistical accuracy (e.g., King & Schneider 2003; Fan 2007; van den Bosch et al. 2013; More et al. 2013; Heymans et al. 2013).

It should be emphasized that the impacts of observational or astrophysical effects can be different for different weak-lensing analyses. Most of the above mentioned requirements, e.g., the accuracy of shape measurement and of photo-z, are derived from two-point correlation/power spectrum studies. Other statistical quantities, such as higher-order correlations, g-g lensing and peak abundance, may require different systematic controls. To fully realize the power of future large weak-lensing surveys, careful investigations of systematic effects for different weak-lensing studies are needed. Joint analyses of multiple statistical quantities related to weak lensing should be helpful to diagnose the possible existence of systematic effects, and further to reduce their impacts on cosmological studies (e.g., Weinberg et al. 2013b).

In this paper, we focus our discussions on weak-lensing shear signals obtained by accurately measuring shapes of faint galaxies. However, they are not the only observables related to weak lensing. Weak-lensing magnification can affect the observed size, flux and therefore the number density of background objects (e.g., Bartelmann & Schneider 2001; Zhang & Pen 2005; van Waerbeke 2010; Bauer et al. 2011; Mao et al. 2012; Morrison et al. 2012; Ford et al. 2014; Yang et al. 2013b). Higher order weak-lensing effects, such as flexion, can reveal more detailed structures about the distribution of dark matter (e.g., Goldberg & Bacon 2005; Bartelmann et al. 2013; Er & Bartelmann 2013; Rowe et al. 2013). Compared with other cosmological probes, the full potential of weak-lensing cosmological studies is far from being achieved by current observations. Future large surveys will bring weak-lensing analyses to the central stage of cosmological studies. The complete matrix involving different weak-lensing observables and statistical analyses will be in place, which is expected to greatly improve our understanding about the dark side of the Universe.

Acknowledgements We thank Xiangkun Liu for providing us Figs. 1–4 and Fig. 6. We are very grateful to N. Okabe, T. Futamase, M. Oguri, J.P. Dietrich, R. Mandelbaum, R. Li, R. Massey, E. Semboloni, M. Kilbinger, J. Benjamin, M. Velander, L. van Waerbeke and J.Q. Xia for kindly allowing us to reproduce figures from their original papers. We are also thankful for AAS, APS and Oxford University Press on behalf of the Royal Astronomical Society for granting us permission for figure reproduction. L. P. Fu is supported in part by the National Natural Science Foundation of China (Grant Nos. 11333001 and 11103012), Innovation Program 12ZZ134 of SMEC, STCSM Pujiang Program (12PJ1406700) and Shanghai Research (Grant 13JC1404400). Z. H. Fan is supported in part by the National Natural Science Foundation of China (Grant Nos. 11333001, 11173001 and 11033005).

References

LSST Science Collaboration, Abell, P. A., Allison, J., et al. 2009, arXiv: 0912.0201
LSST Science Collaboration, Abell, P. A., Allison, J., et al. 2012, arXiv: 1211.0310
The Dark Energy Survey Collaboration, Abbott, T. et al. 2005, arXiv: astro-ph/0510346
Abdalla, F. B., Amara, A., Capak, P., et al. 2008, MNRAS, 387, 969
Abdalla, F. B., Banerji, M., Lahav, O., & Rashkov, V. 2011, MNRAS, 417, 1891
Abrahamse, A., Knox, L., Schmidt, S., et al. 2011, ApJ, 734, 36
Adami, C., Mazure, A., Pierre, M., et al. 2011, A&A, 526, A18
Planck Collaboration, Ade, P. A. R., Aghanim, N., et al. 2013a, A&A in press, arXiv:1303.5076
Planck Collaboration, Ade, P. A. R., Aghanim, N., et al. 2013b, A&A in press, arXiv:1303.5080
Albrecht, A., Bernstein, G., Cahn, R., et al. 2006, arXiv: astro-ph/0609591
Amara, A., & Réfrégier, A. 2008, MNRAS, 391, 228
Amendola, L., Appleby, S., Bacon, D., et al. 2013, Living Reviews in Relativity, 16, 6 (Review of Euclid Theory Working Group, arXiv:1206.1225)
Amiaux, J., Scaramella, R., Mellier, Y., et al. 2012, in Society of Photo-Optical Instrumentation Engineers (SPIE) Conference Series, 8442, arXiv: 1209.2228
Anderson, L., Aubourg, E., Bailey, S., et al. 2012, MNRAS, 427, 3435
Auger, M. W., Budzynski, J. M., Belokurov, V., Koposov, S. E., & McCarthy, I. G. 2013, MNRAS, 436, 503
Bacon, D. J., Refregier, A. R., & Ellis, R. S. 2000, MNRAS, 318, 625
Bahé, Y. M., McCarthy, I. G., & King, L. J. 2012, MNRAS, 421, 1073
Baldauf, T., Smith, R. E., Seljak, U., & Mandelbaum, R. 2010, Phys. Rev. D, 81, 063531
Bardeen, J. M., Bond, J. R., Kaiser, N., & Szalay, A. S. 1986, ApJ, 304, 15
Bartelmann, M. 1995, A&A, 303, 643
Bartelmann, M., King, L. J., & Schneider, P. 2001, A&A, 378, 361
Bartelmann, M., Limousin, M., Meneghetti, M., & Schmidt, R. 2013, Space Sci. Rev., 177, 3
Bartelmann, M., Narayan, R., Seitz, S., & Schneider, P. 1996, ApJ, 464, L115
Bartelmann, M., & Schneider, P. 2001, Phys. Rep., 340, 291
Bauer, A. H., Seitz, S., Jerke, J., et al. 2011, ApJ, 732, 64
Bauer, D., Buckley, J., Cahill-Rowley, M., et al. 2013, arXiv:1305.1605
Becker, M. R., & Kravtsov, A. V. 2011, ApJ, 740, 25
Benítez, N. 2000, ApJ, 536, 571
Benjamin, J., Van Waerbeke, L., Heymans, C., et al. 2013, MNRAS, 431, 1547
Bernardeau, F., van Waerbeke, L., & Mellier, Y. 1997, A&A, 322, 1
Bernstein, G., & Huterer, D. 2010, MNRAS, 401, 1399
Bernstein, G. M., & Jarvis, M. 2002, AJ, 123, 583
Bhattacharya, S., Habib, S., Heitmann, K., & Vikhlinin, A. 2013, ApJ, 766, 32
Bhattacharya, S., Heitmann, K., White, M., et al. 2011, ApJ, 732, 122
Birkinshaw, M. 1999, Phys. Rep., 310, 97
Blandford, R., & Narayan, R. 1986, ApJ, 310, 568
Blas, D., Lesgourgues, J., & Tram, T. 2011, J. Cosmol. Astropart. Phys., 7, 034
Böhringer, H., Chon, G., Collins, C. A., et al. 2013, A&A, 555, A30
Bolzonella, M., Miralles, J.-M., & Pelló, R. 2000, A&A, 363, 476
Bond, J. R., Cole, S., Efstathiou, G., & Kaiser, N. 1991, ApJ, 379, 440
Bond, J. R., & Myers, S. T. 1996, ApJS, 103, 1
Brainerd, T. G., Blandford, R. D., & Smail, I. 1996, ApJ, 466, 623
Bridle, S. L., Hobson, M. P., Lasenby, A. N., & Saunders, R. 1998, MNRAS, 299, 895
Bridle, S., Shawe-Taylor, J., Amara, A., et al. 2009, Annals of Applied Statistics, 3, 6
Bridle, S., Balan, S. T., Bethge, M., et al. 2010, MNRAS, 405, 2044
Brimioulle, F., Seitz, S., Lerchster, M., Bender, R., & Snigula, J. 2013, MNRAS, 432, 1046

Broadhurst, T., Umetsu, K., Medezinski, E., Oguri, M., & Rephaeli, Y. 2008, ApJ, 685, L9
Brown, M. L., Taylor, A. N., Hambly, N. C., & Dye, S. 2002, MNRAS, 333, 501
Bullock, J. S., Kolatt, T. S., Sigad, Y., et al. 2001, MNRAS, 321, 559
Cacciato, M., van den Bosch, F. C., More, S., Mo, H., & Yang, X. 2013, MNRAS, 430, 767
Cacciato, M., van Uitert, E., & Hoekstra, H. 2014, MNRAS, 437, 377
Carlstrom, J. E., Holder, G. P., & Reese, E. D. 2002, ARA&A, 40, 643
Chang, C., Kahn, S. M., Jernigan, J. G., et al. 2013, MNRAS, 428, 2695
Clowe, D., Luppino, G. A., Kaiser, N., & Gioia, I. M. 2000, ApJ, 539, 540
Clowe, D., Bradač, M., Gonzalez, A. H., et al. 2006, ApJ, 648, L109
Corless, V. L., & King, L. J. 2008, MNRAS, 390, 997
Corless, V. L., King, L. J., & Clowe, D. 2009, MNRAS, 393, 1235
Courteau, S., Cappellari, M., de Jong, R. S., et al. 2014, Reviews of Modern Physics, 86, 47
Crittenden, R. G., Natarajan, P., Pen, U.-L., & Theuns, T. 2002, ApJ, 568, 20
Cunha, C. E., Huterer, D., Busha, M. T., & Wechsler, R. H. 2012, MNRAS, 423, 909
Dahlen, T., Mobasher, B., Faber, S. M., et al. 2013, ApJ, 775, 93
De Boni, C., Ettori, S., Dolag, K., & Moscardini, L. 2013, MNRAS, 428, 2921
Dietrich, J. P., Böhnert, A., Lombardi, M., Hilbert, S., & Hartlap, J. 2012a, MNRAS, 419, 3547
Dietrich, J. P., & Hartlap, J. 2010, MNRAS, 402, 1049
Dietrich, J. P., Werner, N., Clowe, D., et al. 2012b, Nature, 487, 202
Dodelson, S. 2004, Phys. Rev. D, 70, 023008
Dodelson, S. 2003, Modern Cosmology (Academic Press)
Du, W., & Fan, Z. 2014, ApJ, 785, 57
Duffy, A. R., Schaye, J., Kay, S. T., & Dalla Vecchia, C. 2008, MNRAS, 390, L64
Einasto, J. 1965, Trudy Inst. Astrofiz. Alma-Ata, 51, 8
Eisenstein, D. J., & Hu, W. 1999, ApJ, 511, 5
Er, X., & Bartelmann, M. 2013, MNRAS, 428, 103
Erben, T., Hildebrandt, H., Miller, L., et al. 2013, MNRAS, 433, 2545
Fahlman, G., Kaiser, N., Squires, G., & Woods, D. 1994, ApJ, 437, 56
Fan, Z. 2003, ApJ, 594, 33
Fan, Z.-H. 2007, ApJ, 669, 10
Fan, Z., Shan, H., & Liu, J. 2010, ApJ, 719, 1408
Ford, J., Hildebrandt, H., Van Waerbeke, L., et al. 2014, MNRAS, 439, 3755
Fry, J. N. 1984, ApJ, 279, 499
Fu, L., Semboloni, E., Hoekstra, H., et al. 2008, A&A, 479, 9
Fu, L., Kilbinger, M., Erben, T., et al. 2014, MNRAS, 441, 2725
Gao, L., Navarro, J. F., Cole, S., et al. 2008, MNRAS, 387, 536
Gao, L., Navarro, J. F., Frenk, C. S., et al. 2012, MNRAS, 425, 2169
Gavazzi, R., & Soucail, G. 2007, A&A, 462, 459
Geller, M. J., Kurtz, M. J., Dell'Antonio, I. P., Ramella, M., & Fabricant, D. G. 2010, ApJ, 709, 832
George, M. R., Leauthaud, A., Bundy, K., et al. 2012, ApJ, 757, 2
Gillis, B. R., Hudson, M. J., Erben, T., et al. 2013, MNRAS, 431, 1439
Giocoli, C., Meneghetti, M., Ettori, S., & Moscardini, L. 2012, MNRAS, 426, 1558
Giocoli, C., Tormen, G., & van den Bosch, F. C. 2008, MNRAS, 386, 2135
Goldberg, D. M., & Bacon, D. J. 2005, ApJ, 619, 741
Guzik, J., & Seljak, U. 2001, MNRAS, 321, 439
Hamana, T., Oguri, M., Shirasaki, M., & Sato, M. 2012, MNRAS, 425, 2287
Hamana, T., Takada, M., & Yoshida, N. 2004, MNRAS, 350, 893
Harnois-Déraps, J., Vafaei, S., & Van Waerbeke, L. 2012, MNRAS, 426, 1262
Hasselfield, M., Hilton, M., Marriage, T. A., et al. 2013, J. Cosmol. Astropart. Phys., 7, 008
Hearin, A. P., Zentner, A. R., & Ma, Z. 2012, J. Cosmol. Astropart. Phys., 4, 034

Hearin, A. P., Zentner, A. R., Ma, Z., & Huterer, D. 2010, ApJ, 720, 1351
Heitmann, K., Lawrence, E., Kwan, J., Habib, S., & Higdon, D. 2014, ApJ, 780, 111
Hennawi, J. F., & Spergel, D. N. 2005, ApJ, 624, 59
Henry, J. P. 2000, ApJ, 534, 565
Hernquist, L. 1990, ApJ, 356, 359
Hetterscheidt, M., Simon, P., Schirmer, M., et al. 2007, A&A, 468, 859
Heymans, C., Grocutt, E., Heavens, A., et al. 2013, MNRAS, 432, 2433
Heymans, C., Van Waerbeke, L., Bacon, D., et al. 2006, MNRAS, 368, 1323
Heymans, C., Van Waerbeke, L., Miller, L., et al. 2012, MNRAS, 427, 146
Hilbert, S., Hartlap, J., White, S. D. M., & Schneider, P. 2009, A&A, 499, 31
Hildebrandt, H., Arnouts, S., Capak, P., et al. 2010, A&A, 523, A31
Hildebrandt, H., Erben, T., Kuijken, K., et al. 2012, MNRAS, 421, 2355
Hirata, C. M., & Seljak, U. 2004, Phys. Rev. D, 70, 063526
Hirata, C. M., Mandelbaum, R., Ishak, M., et al. 2007, MNRAS, 381, 1197
Hoekstra, H., Franx, M., Kuijken, K., & Squires, G. 1998, ApJ, 504, 636
Hoekstra, H., van Waerbeke, L., Gladders, M. D., Mellier, Y., & Yee, H. K. C. 2002, ApJ, 577, 604
Hoekstra, H. 2003, MNRAS, 339, 1155
Hoekstra, H., Franx, M., Kuijken, K., Carlberg, R. G., & Yee, H. K. C. 2003, MNRAS, 340, 609
Hoekstra, H., Hartlap, J., Hilbert, S., & van Uitert, E. 2011, MNRAS, 412, 2095
Hoekstra, H., Bartelmann, M., Dahle, H., et al. 2013, Space Sci. Rev., 177, 75
Hyper Suprime-Cam Design Review, 2009, *http://www.naoj.org/Projects/HSC/report.html*
Hu, W. 1999, ApJ, 522, L21
Hudson, M. J., Gillis, B. R., Coupon, J., et al. 2013, arXiv:1310.6784
Hudson, M. J., Gwyn, S. D. J., Dahle, H., & Kaiser, N. 1998, ApJ, 503, 531
Huterer, D., & Takada, M. 2005, Astroparticle Physics, 23, 369
Ilbert, O., Capak, P., Salvato, M., et al. 2009, ApJ, 690, 1236
Inada, N., Oguri, M., Shin, M.-S., et al. 2012, AJ, 143, 119
Ishibashi, A., & Wald, R. M. 2006, Classical and Quantum Gravity, 23, 235
Israel, H., Erben, T., Reiprich, T. H., et al. 2010, A&A, 520, A58
Israel, H., Erben, T., Reiprich, T. H., et al. 2012, A&A, 546, A79
Jain, B., Seljak, U., & White, S. 2000, ApJ, 530, 547
Jarvis, M., Bernstein, G., & Jain, B. 2004, MNRAS, 352, 338
Jarvis, M., & Jain, B. 2004, astro-ph/0412234
Jarvis, M., Jain, B., Bernstein, G., & Dolney, D. 2006, ApJ, 644, 71
Jee, M. J., Ford, H. C., Illingworth, G. D., et al. 2007, ApJ, 661, 728
Jenkins, A., Frenk, C. S., White, S. D. M., et al. 2001, MNRAS, 321, 372
Jiao, Y.-X., Shan, H.-Y., & Fan, Z.-H. 2011, RAA (Research in Astronomy and Astrophysics), 11, 507
Jing, Y. P. 2000, ApJ, 535, 30
Jing, Y. P., & Suto, Y. 2002, ApJ, 574, 538
Jing, Y. P., Zhang, P., Lin, W. P., Gao, L., & Springel, V. 2006, ApJ, 640, L119
Joachimi, B., Mandelbaum, R., Abdalla, F. B., & Bridle, S. L. 2011, A&A, 527, A26
Joachimi, B., Semboloni, E., Bett, P. E., et al. 2013, MNRAS, 431, 477
Jullo, E., Pires, S., Jauzac, M., & Kneib, J.-P. 2014, MNRAS, 437, 3969
Kaiser, N., & Squires, G. 1993, ApJ, 404, 441
Kaiser, N., Squires, G., & Broadhurst, T. 1995, ApJ, 449, 460
Kaiser, N., Wilson, G., & Luppino, G. A. 2000, astro-ph/0003338
Kang, X., Macciò, A. V., & Dutton, A. A. 2013, ApJ, 767, 22
Kilbinger, M., Fu, L., Heymans, C., et al. 2013, MNRAS, 430, 2200
King, L. J., & Schneider, P. 2003, A&A, 398, 23
Kitching, T., Balan, S., Bernstein, G., et al. 2011, The Annals of Applied Statistics, 5, 2231 (arXiv: 1009.0779)

Kitching, T. D., Balan, S. T., Bridle, S., et al. 2012, MNRAS, 423, 3163
Kitching, T. D., Miller, L., Heymans, C. E., van Waerbeke, L., & Heavens, A. F. 2008, MNRAS, 390, 149
Kitching, T. D., Rowe, B., Gill, M., et al. 2013, ApJS, 205, 12
Kitching, T. D. & Taylor, A. N. 2011, MNRAS, 416, 1717
Knebe, A., Pearce, F. R., Lux, H., et al. 2013, MNRAS, 435, 1618
Kneib, J.-P., & Natarajan, P. 2011, A&A Rev., 19, 47
Komatsu, E., Smith, K. M., Dunkley, J., et al. 2011, ApJS, 192, 18
Kovner, I., & Milgrom, M. 1987, ApJ, 321, L113
Kratochvil, J. M., Haiman, Z., & May, M. 2010, Phys. Rev. D, 81, 043519
Kruse, G., & Schneider, P. 1999, MNRAS, 302, 821
Kruse, G., & Schneider, P. 2000, MNRAS, 318, 321
Kuijken, K. 2006, A&A, 456, 827
Kurtz, M. J., Geller, M. J., Utsumi, Y., et al. 2012, ApJ, 750, 168
Laureijs, R., Amiaux, J., Arduini, S., et al. 2011, EUCLID Collaboration: Euclid Definition Study Report, arXiv: 1110.3193
Lawrence, E., Heitmann, K., White, M., et al. 2010, ApJ, 713, 1322
Leauthaud, A., Finoguenov, A., Kneib, J.-P., et al. 2010, ApJ, 709, 97
Leauthaud, A., Tinker, J., Bundy, K., et al. 2012, ApJ, 744, 159
Lewis, A., Challinor, A., & Lasenby, A. 2000, ApJ, 538, 473
Li, H., Liu, J., Xia, J.-Q., et al. 2009a, Physics Letters B, 675, 164
Li, R., Mo, H. J., Fan, Z., et al. 2009b, MNRAS, 394, 1016
Li, R., Mo, H. J., Fan, Z., Yang, X., & Bosch, F. C. v. d. 2013, MNRAS, 430, 3359
Li, R., Shan, H., Mo, H., et al. 2014, MNRAS, 438, 2864
Limber, D. N. 1954, ApJ, 119, 655
Liu, X., Wang, Q., Pan, C., & Fan, Z. 2014, ApJ, 784, 31
Ludlow, A. D., Navarro, J. F., Boylan-Kolchin, M., et al. 2013, MNRAS, 432, 1103
Luppino, G. A., & Kaiser, N. 1997, ApJ, 475, 20
Lynds, R., & Petrosian, V. 1989, ApJ, 336, 1
Ma, Z., & Bernstein, G. 2008, ApJ, 682, 39
Ma, Z., Hu, W., & Huterer, D. 2006, ApJ, 636, 21
Mandelbaum, R., Tasitsiomi, A., Seljak, U., Kravtsov, A. V., & Wechsler, R. H. 2005, MNRAS, 362, 1451
Mandelbaum, R., Seljak, U., Kauffmann, G., Hirata, C. M., & Brinkmann, J. 2006, MNRAS, 368, 715
Mandelbaum, R., Seljak, U., & Hirata, C. M. 2008, J. Cosmol. Astropart. Phys., 8, 006
Mandelbaum, R., Slosar, A., Baldauf, T., et al. 2013, MNRAS, 432, 1544
Mandelbaum, R., Rowe, B., Bosch, J., et al. 2014, ApJS, 212, 5
Mann, A. W., & Ebeling, H. 2012, MNRAS, 420, 2120
Mao, S., Wang, J., & Smith, M. C. 2012, MNRAS, 422, 2808
Marian, L., Hilbert, S., Smith, R. E., Schneider, P., & Desjacques, V. 2011, ApJ, 728, L13
Marian, L., Smith, R. E., & Bernstein, G. M. 2009, ApJ, 698, L33
Marian, L., Smith, R. E., & Bernstein, G. M. 2010, ApJ, 709, 286
Marian, L., Smith, R. E., Hilbert, S., & Schneider, P. 2012, MNRAS, 423, 1711
Marian, L., Smith, R. E., Hilbert, S., & Schneider, P. 2013, MNRAS, 432, 1338
Massey, R., & Refregier, A. 2005, MNRAS, 363, 197
Massey, R., Heymans, C., Bergé, J., et al. 2007, MNRAS, 376, 13
Massey, R., Hoekstra, H., Kitching, T., et al. 2013, MNRAS, 429, 661
Maturi, M., Angrick, C., Pace, F., & Bartelmann, M. 2010, A&A, 519, A23
Maturi, M., Meneghetti, M., Bartelmann, M., Dolag, K., & Moscardini, L. 2005, A&A, 442, 851
Mehrtens, N., Romer, A. K., Hilton, M., et al. 2012, MNRAS, 423, 1024
Miller, L., Heymans, C., Kitching, T. D., et al. 2013, MNRAS, 429, 2858
Miller, L., Kitching, T. D., Heymans, C., Heavens, A. F., & van Waerbeke, L. 2007, MNRAS, 382, 315

Miralda-Escude, J. 1996, in Astrophysical Applications of Gravitational Lensing, IAU Symposium, 173, eds. C. S. Kochanek & J. N. Hewitt, 131
Miyazaki, S., Hamana, T., Shimasaku, K., et al. 2002, ApJ, 580, L97
Miyazaki, S., Hamana, T., Ellis, R. S., et al. 2007, ApJ, 669, 714
Miyatake, H., More, S., Mandelbaum, R., et al. 2013, arXiv:1311.1480
Mo, H., van den Bosch, F. C., & White, S. 2010, Galaxy Formation and Evolution (Cambridge: Cambridge Univ. Press, 2010)
Moore, B., Quinn, T., Governato, F., Stadel, J., & Lake, G. 1999, MNRAS, 310, 1147
More, A., Cabanac, R., More, S., et al. 2012, ApJ, 749, 38
More, S., van den Bosch, F. C., Cacciato, M., et al. 2013, MNRAS, 430, 747
Morrison, C. B., Scranton, R., Ménard, B., et al. 2012, MNRAS, 426, 2489
Nakajima, R., & Bernstein, G. 2007, AJ, 133, 1763
Navarro, J. F., Frenk, C. S., & White, S. D. M. 1996, ApJ, 462, 563
Navarro, J. F., Frenk, C. S., & White, S. D. M. 1997, ApJ, 490, 493
Navarro, J. F., Ludlow, A., Springel, V., et al. 2010, MNRAS, 402, 21
Newman, J., Abate, A., Abdalla, F., et al. 2013, arXiv:1309.5384
Newman, J. A. 2008, ApJ, 684, 88
Nord, B., Stanek, R., Rasia, E., & Evrard, A. E. 2008, MNRAS, 383, L10
Oguri, M., Bayliss, M. B., Dahle, H., et al. 2012, MNRAS, 420, 3213
Oguri, M., & Hamana, T. 2011, MNRAS, 414, 1851
Oguri, M., Takada, M., Okabe, N., & Smith, G. P. 2010, MNRAS, 405, 2215
Okabe, N., Futamase, T., Kajisawa, M., & Kuroshima, R. 2014, ApJ, 784, 90
Okabe, N., Smith, G. P., Umetsu, K., Takada, M., & Futamase, T. 2013, ApJ, 769, L35
Okabe, N., Takada, M., Umetsu, K., Futamase, T., & Smith, G. P. 2010, PASJ, 62, 811
Pan, J., Coles, P., & Szapudi, I. 2007, MNRAS, 382, 1460
Paraficz, D., Kneib, J.-P., Richard, J., et al. 2012, arXiv:1209.0384
Pastor Mira, E., Hilbert, S., Hartlap, J., & Schneider, P. 2011, A&A, 531, A169
Peacock, J. A., & Dodds, S. J. 1996, MNRAS, 280, L19
Peebles, P. J. E. 1980, The Large-scale Structure of the Universe (Princeton: Princeton Univ. Press)
Pen, U.-L., Lee, J., & Seljak, U. 2000, ApJ, 543, L107
Pen, U.-L., Van Waerbeke, L., & Mellier, Y. 2002, ApJ, 567, 31
Pen, U.-L., Zhang, T., van Waerbeke, L., et al. 2003, ApJ, 592, 664
Peterson, J. R., & Fabian, A. C. 2006, Phys. Rep., 427, 1
Prada, F., Klypin, A. A., Cuesta, A. J., Betancort-Rijo, J. E., & Primack, J. 2012, MNRAS, 423, 3018
Press, W. H., & Schechter, P. 1974, ApJ, 187, 425
Refregier, A. 2003, ARA&A, 41, 645
Refregier, A., & Bacon, D. 2003, MNRAS, 338, 48
Reichardt, C. L., Stalder, B., Bleem, L. E., et al. 2013, ApJ, 763, 127
Retana-Montenegro, E., van Hese, E., Gentile, G., Baes, M., & Frutos-Alfaro, F. 2012, A&A, 540, A70
Reyes, R., Mandelbaum, R., Gunn, J. E., et al. 2012, MNRAS, 425, 2610
Rhodes, J., Allen, S., Benson, B. A., et al. 2013, arXiv:1309.5388
Rosati, P., Borgani, S., & Norman, C. 2002, ARA&A, 40, 539
Rowe, B. 2010, MNRAS, 404, 350
Rowe, B., Bacon, D., Massey, R., et al. 2013, MNRAS, 435, 822
Sato, M., Hamana, T., Takahashi, R., et al. 2009, ApJ, 701, 945
Sato, M., & Nishimichi, T. 2013, Phys. Rev. D, 87, 123538
Schirmer, M., Erben, T., Schneider, P., Wolf, C., & Meisenheimer, K. 2004, A&A, 420, 75
Schirmer, M., Erben, T., Hetterscheidt, M., & Schneider, P. 2007, A&A, 462, 875
Schmidt, F., & Rozo, E. 2011, ApJ, 735, 119

Schneider, P. 1996, MNRAS, 283, 837
Schneider, P. 2003, A&A, 408, 829
Schneider, P., Ehlers, J., & Falco, E. E. 1992, Gravitational Lenses (Berlin: Springer-Verlag)
Schneider, P., & Rix, H.-W. 1997, ApJ, 474, 25
Schneider, P., van Waerbeke, L., Jain, B., & Kruse, G. 1998, MNRAS, 296, 873
Schneider, P., van Waerbeke, L., Kilbinger, M., & Mellier, Y. 2002a, A&A, 396, 1
Schneider, P., van Waerbeke, L., & Mellier, Y. 2002b, A&A, 389, 729
Schneider, P., & Lombardi, M. 2003, A&A, 397, 809
Schneider, P., Kilbinger, M., & Lombardi, M. 2005, A&A, 431, 9
Schneider, P., Eifler, T., & Krause, E. 2010, A&A, 520, A116
Schrabback, T., Hartlap, J., Joachimi, B., et al. 2010, A&A, 516, A63
Scoccimarro, R., & Couchman, H. M. P. 2001, MNRAS, 325, 1312
Seitz, S., & Schneider, P. 1996, A&A, 305, 383
Seitz, C., & Schneider, P. 1997, A&A, 318, 687
Seitz, S., Schneider, P., & Bartelmann, M. 1998, A&A, 337, 325
Seljak, U., Makarov, A., Mandelbaum, R., et al. 2005, Phys. Rev. D, 71, 043511
Semboloni, E., Mellier, Y., van Waerbeke, L., et al. 2006, A&A, 452, 51
Semboloni, E., Schrabback, T., van Waerbeke, L., et al. 2011, MNRAS, 410, 143
Semboloni, E., Hoekstra, H., & Schaye, J. 2013, MNRAS, 434, 148
Sereno, M., & Covone, G. 2013, MNRAS, 434, 878
Shan, H., Kneib, J.-P., Tao, C., et al. 2012, ApJ, 748, 56
Shan, H., Kneib, J.-P., Comparat, J., et al. 2013, arXiv:1311.131
Sheth, R. K., & Tormen, G. 1999, MNRAS, 308, 119
Sheth, R. K., Mo, H. J., & Tormen, G. 2001, MNRAS, 323, 1
Simon, P., Erben, T., Schneider, P., et al. 2013, MNRAS, 430, 2476
Simpson, F., Heymans, C., Parkinson, D., et al. 2013, MNRAS, 429, 2249
Smith, R. E., Peacock, J. A., Jenkins, A., et al. 2003, MNRAS, 341, 1311
Soucail, G., Fort, B., Mellier, Y., & Picat, J. P. 1987, A&A, 172, L14
Spergel, D. N., Verde, L., Peiris, H. V., et al. 2003, ApJS, 148, 175
Spergel, D. N., Bean, R., Doré, O., et al. 2007, ApJS, 170, 377
Spergel, D., Gehrels, N., Breckinridge, J., et al. 2013, arXiv: 1305.5425 (WFIRST)
Springel, V., White, S. D. M., Jenkins, A., et al. 2005, Nature, 435, 629
Squires, G., & Kaiser, N. 1996, ApJ, 473, 65
Stanek, R., Evrard, A. E., Böhringer, H., Schuecker, P., & Nord, B. 2006, ApJ, 648, 956
Starck, J.-L., Pires, S., & Réfrégier, A. 2006, A&A, 451, 1139
Sun, L., Fan, Z.-H., Tao, C., et al. 2009, ApJ, 699, 958
Sunyaev, R. A., & Zeldovich, Y. B. 1970, Ap&SS, 7, 20
Takada, M., & Jain, B. 2003, ApJ, 583, L49
Takahashi, R., Sato, M., Nishimichi, T., Taruya, A., & Oguri, M. 2012, ApJ, 761, 152
Tang, J. Y., & Fan, Z. H. 2005, ApJ, 635, 60
Thanjavur, K., Willis, J., & Crampton, D. 2009, ApJ, 706, 571
Tinker, J., Kravtsov, A. V., Klypin, A., et al. 2008, ApJ, 688, 709
Tyson, A. 1992, Physics Today, 45, 24
Tyson, J. A., Valdes, F., Jarvis, J. F., & Mills, A. P., Jr. 1984, ApJ, 281, L59
Tyson, J. A., Wenk, R. A., & Valdes, F. 1990, ApJ, 349, L1
Umetsu, K., & Broadhurst, T. 2008, ApJ, 684, 177
Umetsu, K., Broadhurst, T., Zitrin, A., Medezinski, E., & Hsu, L.-Y. 2011, ApJ, 729, 127
Valageas, P., Sato, M., & Nishimichi, T. 2012, A&A, 541, A161
van den Bosch, F. C., More, S., Cacciato, M., Mo, H., & Yang, X. 2013, MNRAS, 430, 725
van Uitert, E., Hoekstra, H., Velander, M., et al. 2011, A&A, 534, A14

van Waerbeke, L. 2000, MNRAS, 313, 524
van Waerbeke, L. 2010, MNRAS, 401, 2093
van Waerbeke, L., Bernardeau, F., & Mellier, Y. 1999, A&A, 342, 15
Van Waerbeke, L., Mellier, Y., Erben, T., et al. 2000, A&A, 358, 30
Van Waerbeke, L., Hamana, T., Scoccimarro, R., Colombi, S., & Bernardeau, F. 2001, MNRAS, 322, 918
Van Waerbeke, L., Mellier, Y., & Hoekstra, H. 2005, A&A, 429, 75
Van Waerbeke, L., Benjamin, J., Erben, T., et al. 2013, MNRAS, 433, 3373
VanderPlas, J. T., Connolly, A. J., Jain, B., & Jarvis, M. 2012, ApJ, 744, 180
Velander, M., van Uitert, E., Hoekstra, H., et al. 2014, MNRAS, 437, 2111
Wallington, S., Narayan, R., & Kochanek, C. S. 1994, ApJ, 426, 60
Wallington, S., Kochanek, C. S., & Narayan, R. 1996, ApJ, 465, 64
Walsh, D., Carswell, R. F., & Weymann, R. J. 1979, Nature, 279, 381
Warren, M. S., Abazajian, K., Holz, D. E., & Teodoro, L. 2006, ApJ, 646, 881
Watson, W. A., Iliev, I. T., D'Aloisio, A., et al. 2013, MNRAS, 433, 1230
Weinberg, D., Bard, D., Dawson, K., et al. 2013a, arXiv: 1309.5380
Weinberg, D. H., Mortonson, M. J., Eisenstein, D. J., et al. 2013b, Phys. Rep., 530, 87
White, M., van Waerbeke, L., & Mackey, J. 2002, ApJ, 575, 640
Willis, J. P., Clerc, N., Bremer, M. N., et al. 2013, MNRAS, 430, 134
Wittman, D., Dell'Antonio, I. P., Hughes, J. P., et al. 2006, ApJ, 643, 128
Wittman, D. M., Tyson, J. A., Kirkman, D., Dell'Antonio, I., & Bernstein, G. 2000, Nature, 405, 143
Wu, H.-Y., & Huterer, D. 2013, MNRAS, 434, 2556
Xia, J.-Q., Li, H., & Zhang, X. 2013, Phys. Rev. D, 88, 063501
Yang, X., Mo, H. J., van den Bosch, F. C., et al. 2007, ApJ, 671, 153
Yang, X., Kratochvil, J. M., Wang, S., et al. 2011, Phys. Rev. D, 84, 043529
Yang, X., Kratochvil, J. M., Huffenberger, K., Haiman, Z., & May, M. 2013a, Phys. Rev. D, 87, 023511
Yang, X., Zhang, P., Zhang, J., & Yu, Y. 2013b, arXiv:1309.2474
Yoo, J., Tinker, J. L., Weinberg, D. H., et al. 2006, ApJ, 652, 26
Zaldarriaga, M., & Scoccimarro, R. 2003, ApJ, 584, 559
Zentner, A. R., Semboloni, E., Dodelson, S., et al. 2013, Phys. Rev. D, 87, 043509
Zhan, H. 2006, J. Cosmol. Astropart. Phys., 8, 008
Zhan, H., & Knox, L. 2004, ApJ, 616, L75
Zhang, P., & Pen, U.-L. 2005, Physical Review Letters, 95, 241302
Zhang, P., Pen, U.-L., & Bernstein, G. 2010, MNRAS, 405, 359
Zhao, D. H., Jing, Y. P., Mo, H. J., & Börner, G. 2009, ApJ, 707, 354
Zhao, G.-B., & Zhang, X. 2010, Phys. Rev. D, 81, 043518
Zitrin, A., Broadhurst, T., Coe, D., et al. 2011, ApJ, 742, 117
Zitrin, A., Bartelmann, M., Umetsu, K., Oguri, M., & Broadhurst, T. 2012, MNRAS, 426, 2944